Investigating the Microstructural and Mechanical Properties of the Novel Metallic Materials Used in Interdisciplinary Fields and Constructing a Relationship with the Biocompatibility in Biomedical Applications

by

Benay Uzer

A Dissertation Submitted to the
Graduate School of Sciences and Engineering
in Partial Fulfillment of the Requirements for
the Degree of

Doctor of Philosophy
in
Mechanical Engineering

Koç University

July, 201

Investigating the Microstructural and Mechanical Properties of the Novel Metallic Materials Used in Interdisciplinary Fields and Constructing a Relationship with the Biocompatibility in Biomedical Applications

Koç University

Graduate School of Sciences and Engineering

This is to certify that I have examined this copy of a doctoral dissertation by

Benay Uzer

and have found that it is complete and satisfactory in all respects,
and that any and all revisions required by the final
examining committee have been made.

Committee Members:

_____

Assoc. Prof. Demircan Canadinç

_____

Assoc. Prof. B. Erdem Alaca

_____

Asst. Prof. Alper Uzun

_____

Assoc. Prof. Hakan Usta

_____

Asst. Prof. İlknur Eruçar Fındıkçı

Date: 19/07/2017

ABSTRACT

In this dissertation novel metallic materials utilized in interdisciplinary applications have been analyzed by constructing a relationship between their microstructural and mechanical properties. For this aim the materials used for structural and biomedical applications were subjected to mechanical tests and the microstructural evolutions were investigated via various characterization techniques. These properties were also incorporated in the biocompatibility evaluations of the implant materials.

The initial tests were carried out to understand the effect of microstructural evolution on the cell response on the potential implant materials which were deformed up to different strain levels. Microscopy analyses showed that the brain tumor cells exhibited the best attachment and viability on the sample with the greatest plastic deformation where a significant slip activity was prevalent, accompanied by considerable slip-twin interactions. Specifically the deposition of proteins necessary for the focal contact formation on the implant surface was promoted on this sample owing to the greater energy provided by the interactions of the slip and twinning. This study showed that by manipulating the microstructure of the implant material improved cell response and consequently a more successful treatment can be obtained. This study was continued with another cell type in order to understand whether different cells would all react in the same way or not. Conversely, fibroblast cells did not exhibit enhanced cell response with the increased plastic deformation, which might stem from the failure of the adhesion of ECM proteins, or incompatibility with cell size or surface roughness. This study pointed out the importance of selecting a unique implant material specific for the body location and the tissue that the metal will be in contact with.

Biocompatibility of the metallic materials was further analyzed in order to thoroughly understand the parameters affecting it. Specifically the immersion experiments of Nickel Titanium (NiTi) orthodontic archwires through the incorporation of the realistic mechanical

conditions into *ex situ* experiments showed that toxic Ni ion release increased due to stress corrosion cracking (SCC). The stress accumulated in the archwire-bracket contact sites leads to surface cracks in concomitant with the corrosive environment of the artificial saliva. This study was followed by investigating the dissolution-reformation cycle of the protective oxide layer on the archwires. The results showed that Ni ion release enhanced owing to the dissolution of the oxide layer and with the reformation the net ion contribution has decreased significantly. These findings showed the need for incorporating the actual chemical and mechanical condition into the *ex situ* experiments and thorough analysis of the protective oxide layer in order to correctly evaluate the biocompatibility of the materials.

After thoroughly evaluating the biocompatibility of the metallic implants further experiments were carried out to better understand the microstructure and mechanical properties of the materials which exhibit complex slip and twinning activity upon loading. With this aim both polycrystalline and single crystal metals were tested in order to better understand the activation of the plastic deformation mechanisms with and without the influence of the grain boundary interactions. These studies showed the enhanced mechanical properties owing to the impediment of slip by the twins and formation of nanotwins within the primary twins. The mutual interaction of these mechanisms has strengthened the material, thus materials were able to accommodate the great amount of deformation.

Overall the findings of this dissertation show that a thorough analysis of microstructural analysis is needed to better understand the mechanical properties of the metallic materials. Moreover, for the biocompatibility evaluation of the metallic implants the incorporation of microstructural and mechanical properties was pointed out to be utmost importance.

ÖZET

Bu tezde disiplinler arası uygulamalarda kullanılan üstün özellikli metal malzemeler mikroyapı ve mekanik özellikleri ilişkilendirilerek derinlemesine incelenmiştir. Bu amaçla yapısal ve biyomedikal alanlarda kullanılan malzemeler mekanik testler ile deforme edilmiş ve mikro yapı evrimleri farklı mikroskopi teknikleri ile incelenmiştir. Ayrıca incelenen bu özellikler implant malzemelerin biyouyumluluklarının değerlendirilmesine de dahil edilmiştir.

Öncelikle, farklı gerinimlere deforme edilmiş potansiyel implant malzemelerde mikro yapı evriminin hücre davranışına olan etkisi incelenmiştir. Yapılan mikroskopi analizleri beyin tümörü hücrelerinin en iyi yapışma ve canlılığı en yüksek gerinime deforme edilmiş, kayma ve ikiz mekanizmalarının etkileşiminin fazlaca görüldüğü örnek üzerinde sergilediğini göstermiştir. Özellikle bu etkileşimin sağladığı yüksek enerji sayesinde hücre yapışmasında görev alan proteinlerin implant yüzeyine yapışması kolaylaşmıştır. Bu çalışma implant malzemelerin mikro yapılarının değiştirilmesiyle daha iyileşmiş hücre davranışı ve buna bağlı olarak daha başarılı bir tedavi elde edilebileceğini göstermiştir. Bu çalışma farklı hücre tiplerinin de aynı sonucu verip veremeyeceğini incelemek amacıyla başka bir hücre tipiyle devam ettirilmiştir. Beyin tümörünün aksine fibroblast hücreleri plastik deformasyonla paralel olarak gelişmiş bir hücre davranışı göstermemiştir. Bunun nedenleri arasında ECM proteinlerinin yapışmasındaki başarısızlık veya hücre boyu veya yüzey pürüzlülüğünün uyumsuzluğu gösterilebilir. Bu çalışma implant malzeme seçiminin metal malzemenin temas edeceği dokuya özel olarak seçilmesi gerekliliğini göstermiştir.

Metal malzemelerin biyouyumluluklarını etkileyen tüm parametrelerin anlaşılması amacıyla daha detaylıca incelemeler yapılmıştır. Özellikle Nikel-Titanyum (NiTi) diş tellerindeki gerçek yükleme koşullarının *ex situ* deneylere dahil edilmesiyle oluşan gerilimli korozyon çatlakları nedeniyle Ni iyon salınımındaki artış gösterilmiştir. Diş teli ve braket temas noktalarında biriken gerilim asidik ortamın aşındırıcı etkisiyle birlikte tel yüzeyinde çatlaklara neden olmuştur. Bu çalışmanın devamında diş tellerinin yüzeyindeki koruyucu oksit tabakasının çözünme-yeniden

oluşma döngüsü incelenmiştir. Sonuçlar Ni iyon salımının oksit tabakasının çözünmesiyle arttığını ve yeniden oluşmasıyla azaldığını göstermiştir. Bu çalışmalar malzemelerin biyouyumluluklarının değerlendirilmesinde gerçek kimyasal ve yükleme koşullarının *ex situ* deneylere katılmasının ve koruyucu oksit tabakasının detaylıca incelenmesinin gerekliliğini göstermiştir.

Metalik implant malzemelerin biyouyumluluklarının detaylıca değerlendirilesinin ardından yük altında karmaşık kayma ve ikiz mekanizması aktivitesi gösteren malzemelerin mikro yapı ve mekanik özelliklerini anlamak için ilave deneyler yapılmıştır. Bu amaçla çok taneli ve tek taneli metal örnekler tane sınırı etkileşimleri etkisi altında ve tane sınırı olmayacak şekilde test edilmiştir. Bu çalışmalar kayma mekanizmasının ikiz mekanizması ile engellendiğini, birincil ikizlerin içinde oluşan nano ikizler sayesinde malzemelerin güçlendiğini ve bunların sayesinde malzemelerin daha yüksek miktardaki deformasyona dayanabildiğini göstermiştir

Bu tezde yapılan çalışmaların sonuçları malzemelerin mekanik özelliklerinin iyi bir şekilde anlaşılabilmesi için mikro yapılarının detaylıca incelenmesi gerektiğini göstermiştir. Ayrıca metalik implantların biyouyumluluk değerlendirilmelerinde mikro yapı ve mekanik özelliklerin dahil edilmesinin büyük önem taşıdığı belirtilmiştir.

CONTENTS

Dedicated to my beloved family, for their endless love, support and presence…

ACKNOWLEDGEMENT

Firstly, I would like to express my sincere gratitude to my advisor Assoc. Prof. Demircan Canadinç for the continuous support of my PhD study and related research, for his patience, motivation, and immense knowledge. His guidance helped me in all the time of research and writing of this thesis. He has always supported me to fulfill my potential and provided all the resources to carry out my research in Turkey and abroad. The joyful and productive research environment he has built made my 4 years unforgettable. I could not have imagined having a better advisor and mentor for my PhD study.

I would like to thank to my thesis progress supervision committee members Assoc. Prof. Erdem Alaca and Asst. Prof. Alper Uzun for their valuable comments and supervision throughout my PhD study. I also would like to thank Assoc. Prof. Hakan Usta and Asst. Prof İlknur Eruçar Fındıkçı for their participation in my thesis committee and the valuable contribution. I must also express my profound gratitude to our collaborators Prof. Ibrahim Karaman, Prof. Hans J. Maier, Prof. Yuri Chumlyakov, Asst. Prof. Tuğba Bağcı Önder and Ahmet Cingöz.

I want to acknowledge the financial support by the Scientific and Technological Research Council of Turkey (TÜBİTAK) within the National Graduate Student Fellowship Program 2211.

I must express my gratitude to Türkan, Ayşe Abla, Hacer Abla ve Songül Abla who are the part of the big family I had at Koç University. Without their presence my experience at Koç University wouldn't have been as unforgettable as it is now. I wish to express my sincere thanks to Derya Ernur, Emine Büyükdurmuş, Elif Tüysüz, Özge Armağan Çelik and Pelin Manzak for their endless support, assistance and friendship throughout my study at Koç University.

I am so grateful to be a member of Advanced Materials Group and thank its members for making my PhD full of joy. Without them my PhD wouldn't have been that much fun. Minomm,

the funniest person I have ever met. Her enthusiasm for doing PhD (the golden bracelet) can be the main motivation for many of AMG members and the other colleagues. I learned a lot from her knowledge and working with her was one of the best part of PhD. Berçom, such an amazing person who can solve everyone's problem in less than a minute. He is one of the people that everyone takes as a role model. Atkuş the energetic person and the joy of our group who could dance, talk, eat and write a journal at the same time. Cemre, she was the most creative person of AMG and coming up with the most fun ideas for gifts. Morad, the person with a wonderful heart who was our transfer from Tabriz. I am so grateful to have my PhD in a great atmosphere with these wonderful people. I want to also thank for their friendship and support all along my PhD to Elmira, Deniz, Ayşen and Işınsu who are the honorary members of AMG.

Before going to Texas A&M University to spend the last year of my PhD I would never imagine I could meet such wonderful people who made that place home for me. Every day we spent together with my dearest roommates Michelle and Simone turned into so much fun. Although they were younger than me I learned a lot from both of them as they were the most mature, kindest and thoughtful people I have ever seen. Ollie, our son with Michelle was the best fish ever. Working with my friends and colleagues Michael, Hande, Tejas, Daniel, Abhinav, Wahaz, William, Ceylan, Ömer, Taymaz, Nazanin, Xavier and all other MESAM research group members made every day in that lab full of fun with our geek conversation. Danny is the best post-doc who at the same time makes the best coffee and Tejo is the best cook while he always made me almost cry with his emotional Indian songs. Going for shopping right after quenching our samples was a routine with Hande. We always cheered each other. Kübra and Utku, my dearest friends and the funniest couple that I got to know in College Station although we lived almost 5 minutes apart in the skirts of Sarıyer. I can never forget their support and friendship in the most difficult times of my life. They are a wonderful family and will grow with their new member of whom I will proudly be an aunt. Seda Tüzün Canadinç, I am so grateful to spend more time with her and learn more about her wonderful personality. I will always model her kind

and thoughtful character. Although the places we traveled together were not the best destinations in the US, I hope that we will be meeting in better places somewhere around the world. I also feel grateful to know Aylin and Ozan Hoca who have always shown support, warmth, sincerity and I enjoyed our conversations on life a lot. I will remember all the good memories in College Station always with a smile.

I am thankful to my colleagues Mahmut, Ümmü, Sedat, Mohammed, Ahmet, Ömer, Ozan, Murat, Oktay, Elif, İrem, Banu, Onur, Mert, and NEMO members Burak, Pelin, Zeynep, Vahid, Ayda and Özge for their friendship. I feel so lucky to know them and with their presence my PhD was more fun.

Özlem, I am so grateful to get to know such a great personality who cares and thinks about her loved ones and always tries to be there for them. I will always remember the late night talks I had with her from diverse field of interest including cinema, science, music…Özge, the funniest of the gang with her great laugh. I loved our chats when I was almost crying from laughing. She is one of the most intellectual people I have known. lrina, such a nice person that I shared so much in common. Although we couldn't spend much time together I enjoyed our walks and talks a lot. I am so grateful to live the best years of my life with these wonderful girls at 24/7.

Çiğdem and Didar, looking back to the first day I met them I could have never imagined that these two girls would be more than sisters to me. As well as we were together in happy moments we were there for each other in hard times of our lives. Didar's talent for empathy and humor, Çiğdem's thoughtfulness for her loved ones and love for everyone shaped my personality to be a better person. We became a one big family with them and their wonderful family members: Nihan, Yüksel Teyze, Embiya Amca, Hülya Teyze and Adnan Amca are the most wonderful people I got to know through them. We may not be together as we used to but the bond between us will last forever.

Finally, I want thank my family for their endless love and support. I cannot thank my parents enough for their endless love and presence. With their unlimited support, encouragement and faith in my decisions I always felt strong on my way to achieve my goals. I feel so lucky to be the aunt of Efe and Emir. They are the prime source of joy and fun in my life. I will always be there for them, see them growing up and become young men. Their love has motivated me to be a better person and aunt for them. I want to thank their parents, my dear sister in law and brother, Senem and Benan for letting me experience this wonderful feeling and for their support all along my life. I also want to acknowledge the support of Aynur and Nail Baydar. I am grateful to my brother who has been my role model all throughout my life.

I dedicate this dissertation to my dear family, for their continuous and endless love, support and presence…

LIST OF TABLES

LIST OF FIGURES

Figure 2.2. Topographic representations of the surface heights (height images) of the samples deformed up to **(a)** 5%, **(b)** 15%, **(c)** 35% and **(d)** 60%.

Figure 2.3. Traces of mechanical twins on the surface of the 35% deformed sample. This gradual transition was obtained by superposing the topography and surface images, and adjusting the transparency of the images. The color bar shows the surface roughness defined in terms of peak distance values along the z axis (in μm).

Figure 2.4. CLSM line profile traversing a twinned region on the sample deformed to 35% strain. The encircled areas exhibit a stair-like line profile, where the surface topography changes abruptly, which is characteristic of twinning.

Figure 2.5. (a) Laser **(b)** and height images of grains showing overall surface topography of the sample deformed to 35%. The color bar represents the surface roughness defined in terms of peak distance values along the z axis (in μm).

Figure 2.6. (a) Laser **(b)** and height images of the boundary of two neighboring grains on the sample deformed to 35% of strain. **(c)** Line profile obtained from the areas marked in the images (a) and (b) showing the sudden drop in surface height. The color bar shows the surface roughness defined in terms of peak distance values along the normal to the surface (in μm).

Figure 2.7. FESEM image showing a grain on the sample deformed to 25% strain: twin-slip interactions are prominent within this grain.

Figure 2.8. (a) Laser **(b)** and height images of the slip lines within a grain in the sample deformed to 35% strain. **(c)** The line profile shows the step-like increase of the surface height by the slip lines within the region marked in **(a)** and **(b)**. The color bar shows the surface roughness defined in terms of peak distance values along the normal to the surface (in μm).

Figure 7.1. Stress-strain curve of the NiCoCr samples in [110], [111] and [123] orientations deformed up to fracture under tensile loading. The optical microscopy (OM) images within the graph were obtained from the samples deformed up to 4% ([110]) and 10% ([111] and [123]) of strain. The crystallographic orientation of the images from top to bottom is: [111], [110] and [123]. The scale bar in OM images is 50μm. (To better understand the graph and its corresponding OM image the reader is referred to the web version of this paper.)

Figure 7.2. TEM micrographs and diffraction patterns of the samples in [110] orientation deformed up to **((a)** and **(b))** 60% and **(c)** fracture**.**

Figure 7.3. TEM micrographs and diffraction patterns of the samples in [111] orientation deformed up to **(a)** 10% and **((b), (c)** and **(d))** fracture.

Figure 7.4. TEM micrographs and diffraction patterns of the samples in [123] orientation deformed up to **(a)** 10% and **(b)** fracture**.**

Figure 7.5. TEM bright field images of NiCoCr samples in [123] orientation deformed up to fracture.

1. INTRODUCTION

1.1 Objective

In this dissertation the novel metallic materials used in interdisciplinary applications have been analyzed by constructing a relationship between their microstructural and mechanical properties. For this purpose materials utilized for structural and biomedical applications were subjected to mechanical tests and the activation of plastic deformations were analyzed in detail. In addition, biocompatibility of the implant materials was also investigated and related with the microstructural and mechanical properties of the sample.

Initial study was carried out on stainless steel samples which have been widely used as implant materials in numerous applications. These samples were subjected to tensile test and deformed up to different strain values in order to activate plastic deformation mechanisms in different volume fractions. Surface topography and the microstructural evolution due to the activated slip and twinning mechanisms were analyzed with different material characterization techniques. Brain tumor and fibroblast cells were seeded on these samples which possessed different microstructural and surface properties and the effect of plastic deformation on the biocompatibility of the material was evaluated.

In continuation of this study in order to thoroughly understand the parameters affecting the biocompatibility of the metallic implants further experiments were carried out. Specifically NiTi archwires utilized in orthodontic treatment were subjected to immersion tests by incorporating the realistic mechanical conditions into *ex situ* experiments. In addition to that the formation and dissolution of the protective oxide layer which directly influences the Ni ion release from the implant was analyzed with the static immersion of the archwires.

After completely analyzing the biocompatibility of different implant materials, metals with complex microstructures were subjected to tensile test. Specifically polycrystal Hadfield steel and

single crystal high entropy alloy with low stacking fault energies (SFE) were used which showed activation of twinning mechanism in the early stages of the plastic deformation. The interaction of slip and twinning mechanisms were also analyzed in detail since it contributes significantly to the work hardening rate and improved mechanical strength in these materials. In addition that the work carried out with single crystal materials has helped to better understand the orientation dependence of the slip and twinning mechanisms by circumventing the complications associated with grain boundaries. The knowledge gained by investigating these materials will elucidate the microstructural evolution of the materials that will shape the future applications in structural and biomedical fields.

Overall the aforementioned studies show that the microstructural and mechanical properties of a material are strongly correlated. Particularly the incorporation of these properties into the biocompatibility evaluation of the metallic implants play significant role. Therefore for selecting a material that will be utilized either as a structural material or an implant all these parameters need to be analyzed thoroughly and taken into consideration. The findings of this thesis aim to shed light onto the relation of microstructural evolution and mechanical properties of the metallic materials that would be utilized in interdisciplinary studies, and set higher standards in the material selection for these applications.

1.2 Background

Metallic materials have been utilized in numerous applications including automotive, aerospace, civil engineering and biomedical. New technologies and introduction of materials with superior properties further improve their use in more applications every day. Specifically materials with unprecedented combination of mechanical strength and ductility attract the attention of researchers [1–3]. For instance twinning induced plasticity (TWIP) or high manganese steels have been regarded as a potential candidate to be used in automotive, defense, railroad and mining industries since they have excellent combination of high strength, ductility,

toughness and large strain hardening capacity [1,4,5]. The use of these steels for the manufacturing of car body parts provides a decrease in fuel consumption owing to the manufacturing of lighter cars and improvement in safety due to high energy absorption performance of these steels [1]. Within the last decade new classes of alloys named as high entropy alloys (HEAs) have been popular. These alloys consist of multiple elements which are present in almost equal atomic concentrations on the contrary to the conventional alloys which are composed of one principal element with minor additive ones such as iron based alloys or Ni based superalloys [6,7]. These alloys differ from the previously developed multi principal element alloys (MPEAs) because they form a solid solution without any intermetallic phases which cause brittleness or difficulty in processing [7]. The studies carried out on HEAs in the last few years showed that these alloys present superior mechanical properties, such as high tensile strength, elongation to fracture and fracture toughness [3,8–10]. Particularly at the cryogenic temperatures Cantor alloy (FeMnCrCoNi), and its quaternary (FeNiCoCr) and ternary (NiCoCr) alloys possessed greater yield strength, ultimate tensile strength and fracture toughness without sacrificing the ductility [3,9,11]. These extraordinary properties make these alloys a great choice for the space applications. The further studies that will be carried out on these alloys will elucidate the reasons for these unprecedented properties. In the chapter 7 of this dissertation research carried out on these materials and their microstructural investigations will be explained in detail.

Other than the aforementioned applications metallic materials are also widely used in biomedical applications. Biomaterials are used to replace a part of a living system or to function in an intimate contact with the living tissue [12]. Some of the widely used biomaterials and their applications are listed in Table 1.1. For a biomaterial to function properly in a living organism its biocompatibility constitutes the utmost importance which shows the acceptance of an artificial implant by the surrounding tissue and by the body as a whole. Beside this mechanical,

microstructural and surface properties of the material also play critical role depending on the body part that the implant will be utilized [13,14].

Materials	Advantages	Disadvantages	Examples
Polymers (nylon, silicone rubber, polyester, polytetrafuoroethylene, etc)	Resilient Easy to fabricate	Not strong Deforms with time May degrade	Sutures, blood vessels other soft tissues, sutures, hip socket, ear, nose
Metals (Ti and its alloys, Co–Cr alloys, Au, Ag stainless steels, etc.)	Strong, tough ductile	May corrode Dense Difficult to make	Joint replacements, dental root implants, pacer and suture wires, bone plates and screws
Ceramics (alumina zirconia, calcium phosphates including hydroxyapatite, carbon)	Very bio-compatible	Brittle Not resilient Weak in tension	Dental and orthopedic implants
Composites (carbon–carbon, wire- or fiber- reinforced bone cement)	Strong, tailor-made	Difficult to make	Bone cement, Dental resin

Table 1.1. Biomaterials and examples on their applications in the body [12].

Among the aforementioned materials metallic materials have been the choice for numerous applications throughout the centuries due to their mechanical strength, ductility, fracture toughness, corrosion and wear resistance, and biocompatibility [13,15]. The first attempt to implant a metallic material dates back to 1860s with the use of wires and pins made of iron, gold, silver or platinum which ended up being unsuccessful due to infection after implantation. Aseptic surgical technique developed by Dr. J. Lister has significantly reduced the possibility of the infection and improved their use [15]. The first steel implant was designed for the repair of bone fractures in the early 1900s. Later on this implant was modified in order to decrease the stress concentration through the elimination of the sharp corners in the design (Figure 1.1).

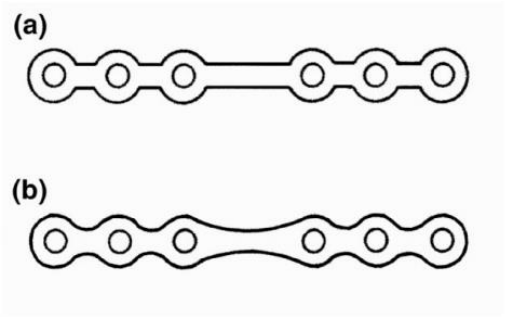

Figure 1.1. Early design of bone fracture plate **(a)** before and **(b)** after the modification of its design [12].

Starting with the use of stainless steel, metallic materials with improved mechanical properties and biocompatibility have been developed which met the requirements of the critical biomedical applications listed in Table 1.2. Nickel Titanium (NiTi) shape memory alloy (SMA) is one of these metallic materials which have been utilized in numerous applications ranging from cardiovascular, orthodontics, orthopedics and physical therapy. The protective titanium oxide layer covering the material improves the biocompatibility although it contains approximately 50% at. of Ni. In addition to that shape memory property of NiTi which enables the alloy to undergo solid to solid phase transformation upon the change of temperature plays critical role in numerous biomedical applications. Numerous studies have been carried out to evaluate the corrosion resistance and biocompatibility of the NiTi alloys and they showed the Ni ion release from the alloy was below the toxic level throughout the testing periods [14,16,17].

Type	Primary utilizations[a]	Status of applications
Stainless steels	1. Temporary devices (fracture plates, screws, hip nails, *etc.*) (Class II) 2. Total hip replacements (Class II)	Routinely applied
Co-based alloys	3. Total joint replacements (wrought alloys) (Class II) 4. Dentistry castings (Class II)	Routinely applied
Ti-based alloys	5. Stem and cup of total hip replacements with CoCrMo or ceramic femoral heads (Class II) 6. Other permanent devices (nails, pacemakers) (Class III)	Routinely applied
Miscellaneous others		
NiTi	1. Orthodontic dental archwires (Class I)	FDA approved
	2. Vascular stents (Class III)	FDA approved
	3. Vena cava filter (Class II)	FDA approved
	4. Intracranial aneurysm clips (Class II)	FDA approved
	5. Contractile artificial muscles for an artificial heart (Class III)	Research
	6. Catheter guide wires (Class II)	FDA approved
	7. Orthopedic staples (Class I)	FDA approved
Mg	Biodegradable orthopedic implants (Class III)	Animal trial
Ta	8. Wire sutures for plastic surgery and neurosurgery (Class III)	FDA approved
	9. A radiographic marker (Class II)	FDA approved

Table 1.2. Metallic biomaterials and their primary applications as implants [15].

As mentioned above for the structural materials the mechanical properties of the biomaterials also play important role in order to achieve a successful treatment. For instance Young's modulus is an important property which can affect the recovery after surgery significantly. Specifically if the modulus of elasticity of an implant placed in the body to repair or replace a bone fracture exceeds the one of the bone then the implant would bear much more load than the bone which consequently can result with the resorption of the bone. In order to eliminate this problem (stress shielding effect) metallic materials with the Young's modulus similar to that of the bone needs to be implanted [15]. Mechanical properties of some of the widely used metallic biomaterials are listed in Table 1.3.

Table 1.3. Mechanical properties of metallic implant materials and cortical bone [15].

Materials	Young's modulus/GPa	Ultimate tensile strength/MPa	Fracture toughness (MPa $\sqrt{m}$)
CoCrMo alloys	240	900–1540	~100
316L stainless steel	200	540–1000	~100
Ti alloys	105–125	900	~80
Mg alloys	40–45	100–250	15–40
NiTi alloy	30–50	1355	30–60
Cortical bone	10–30	130–150	2–12

1.2.1 Plastic Deformation of Metals & Mechanisms

When a material is loaded over its elastic limit, it can not recover its original shape and deforms plastically. There are mainly two types of plastic deformation mechanisms in metals: slip and twinning.

Slip

Slip takes place by the dissociation of the bonds between the parallel planes under shear stress.

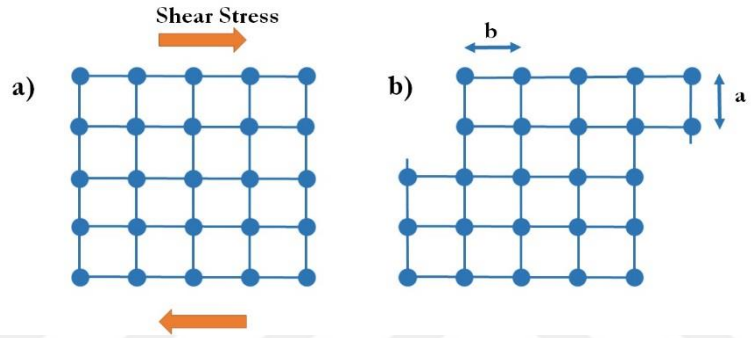

Figure 1.2. Slip mechanism in a perfect crystal.

The critical shear stress for the initiation of this co-operative movement of the atoms in a perfect crystal (Figure 1.2) was first calculated by Frenkel:

$$\tau = \frac{b}{a}\frac{G}{2\pi}$$

where τ is the applied shear stress, G is the shear modulus, b is the spacing between the atoms in the direction of shear stress and a is the spacing between the rows of atom respectively. When the theoretical value of shear stress was compared with the experimental result, a discrepancy between these values was noted. This 10-100 times greater theoretical stress value was explained by the existence of defects in the material which can be listed as point, line, surface and volume. Research independently carried out by Orowan, Polanyi and Taylor in 1934 to reconcile the predicted and experimented stress values showed the presence of dislocations (line defects) in the

material. There are two types of dislocations: edge and screw. In edge dislocation the dislocation line and the Burger's vector which represents the magnitude and direction of the lattice distortion are perpendicular to one another. On the other hand these two vectors are parallel to each other in screw dislocation. Figure 1.3 presents the steps of edge dislocation mechanism where the dislocation is denoted with ⊥ sign. The half plane observed in Figure 1.3 makes the glide of dislocation easier and the material can be plastically deformed with lower energy on the contrary to the mechanism in perfect crystal.

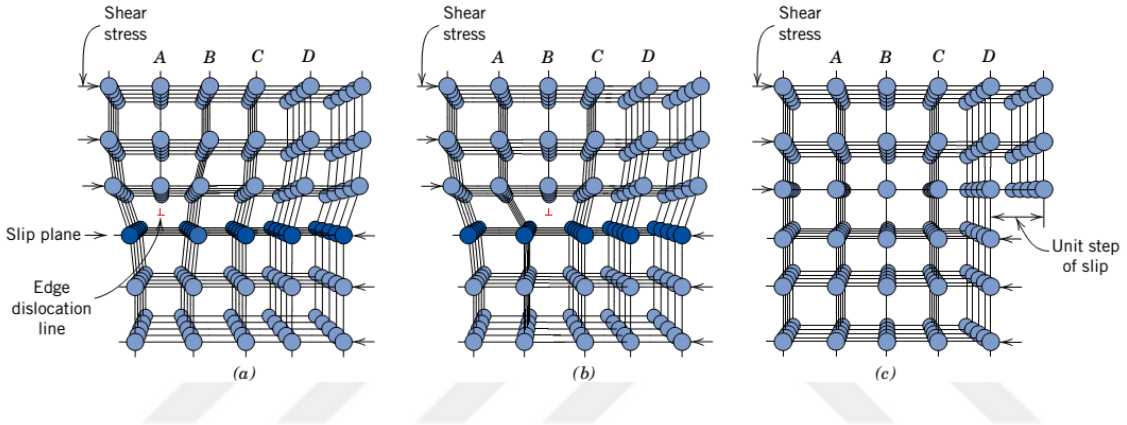

Figure 1.3. Mechanism of an edge dislocation under an applied shear stress. **(a)** The extra half plane is labeled A. **(b)** The dislocation moves one atomic distance to the right and B becomes the extra half-plane. **(c)** A step is formed on the surface of the crystal with the exit of the extra half-plane. [18]

Dislocation movement depends on the crystal structure of the material. In each different crystal there is a preferred plane and direction for this mechanism which is determined by the packing of the atoms. Specifically the slip plane and the direction correspond to the plane and direction which is most closely packed with atoms. The metallic materials investigated in this thesis have face centered cubic (FCC) structure (excluding NiTi SMAs) and the preferential direction and plane family of slip is <110> and {111} respectively. The Burger's vector of a full dislocation in the FCC material is b = a/2<110> as shown with b_1 in Figure 1.4.

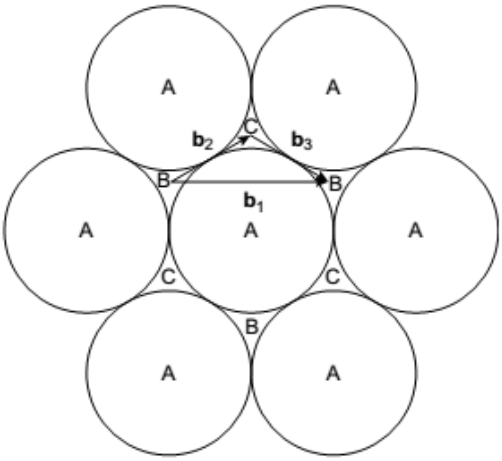

Figure 1.4. Slip of {111} planes in FCC metals [19].

However as presented in Figure 1.4, B atoms choose to move to another B position through position C because of less resistance against this movement. Thus perfect dislocation would dissociate into two partials dislocations (Shockley Partial) with the Burgers vectors of b_2 and b_3. Miller index notation of this dissociation is shown below:

$$\mathbf{1/2\ \langle 110\rangle \rightarrow 1/6\ \langle 211\rangle + 1/6\ \langle 12\text{-}1\rangle}$$

It should be noted that the right-hand side of the notation is equal to the left-hand side: 1/6 [2+1, 1+2, 1+(-1)] which proves that the total Burgers vector doesn't change in the end of this dissociation. Another important point to mention is that the energy of the dislocation is related with the square of its magnitude. This proves the formation of Shockley partials ($b_2^2 + b_3^2 = a^2/3$) which is energetically favorable than the perfect dislocation ($b_1^2 = a^2/2$). Possible Shockley partials in FCC crystal are presented in Figure 1.5.

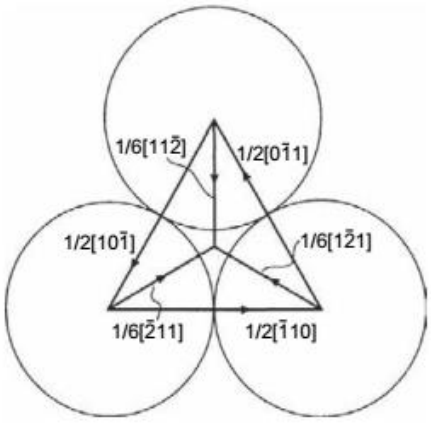

Figure 1.5. Burgers vector of perfect and Shockley partial dislocations in the (111) plane [19].

The dissociation of perfect dislocation into partial dislocations leaves an imperfect crystal where the stacking of the atoms is disrupted. This planar defect between the two partials is named as stacking fault (Figure 1.6). The energy needed to bring these two partial dislocation back together is called as stacking fault energy and is measured in $J.m^{-2}$.

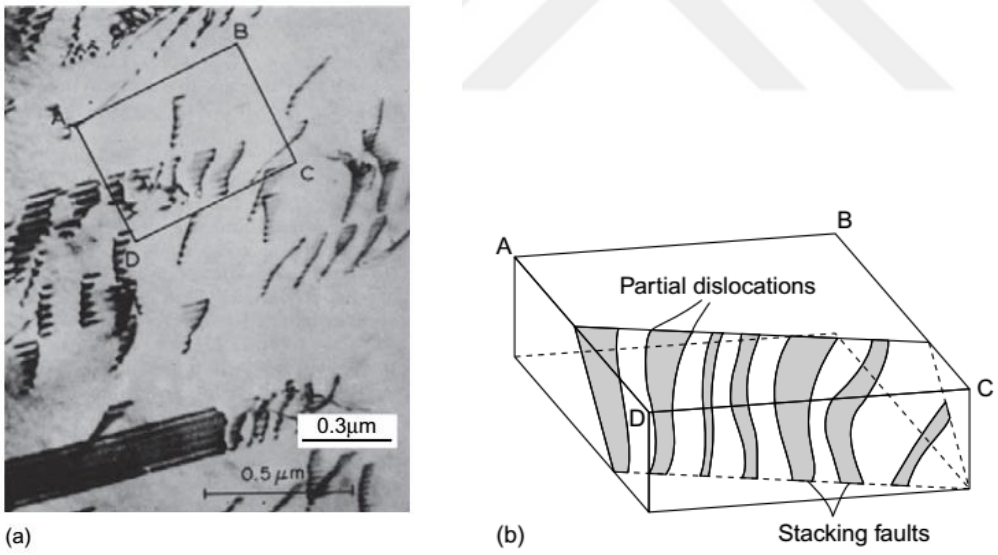

Figure 1.6. (a) Transmission Electron Microscopy (TEM) image of extended dislocations in Cu-7% Al alloy. **(b)** Arrangement of dislocations in the inset in **(a)** [19]**.**

Deformation Twinning

Upon the applied load the formation of partial dislocations lead to the generation of large stacking faults which consequently take role in the formation of twinnings [20]. Atomic movement during twinning causes a mirror like image configuration in the crystal (Figure 1.7). Twins are commonly observed in FCC metals which have low stacking fault energy owing to the lower stress needed to nucleate the twins.

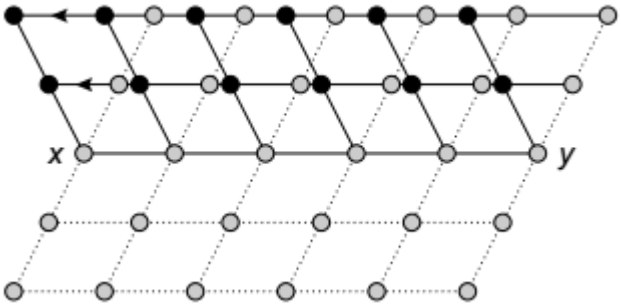

Figure 1.7. Arrangement of atoms during formation twinning [19].

Twinning constitutes an important mechanism for the work hardening behavior of the material. Specifically twin boundaries non-coplanar to mobile dislocations act as barriers to dislocation motion particularly by decreasing the grain size and consequently increasing the work hardening rate. Likewise the Hall-Petch relation which states that the yield strength of the material increases as the grains get smaller the phenomena where the twin boundaries surrogate grain boundaries is called dynamic Hall-Petch effect [21]. In addition to that the formation of nanotwinnings inside the major twinnings would further increase the work hardening rate, delay the onset of necking and increase the ductility [9,22].

During plastic deformation the competition between the slip and twinning mechanisms is strongly dependent on the crystal orientation, temperature or strain rate [21,23,24]. Specifically the research on single crystals have analyzed the activation of these two mechanisms in the early and later stages of the deformation. They have also presented the critical resolved shear stresses

for the nucleation of slip and twinning mechanisms in different materials [24–28]. In the chapter 7 of this dissertation the competition between these mechanisms will be explained in detail by constructing a relationship in crystal orientation.

1.2.2 Characterization of Materials

In this dissertation characterization of mechanical and microstructural properties of metallic materials was carried out via different techniques. The ones utilized by the author will be explained briefly in this chapter.

Characterization of Mechanical Properties

The mechanical properties of the metallic materials were investigated via universal tensile test in this dissertation. Tension test is one of the most common tests to evaluate the mechanical response of the materials and obtain the stress-strain curve (Figure 1.8). The specimen is deformed, usually up to the fracture strain, with a gradually increasing load which is applied uniaxially along the longitudinal axis. Dogbone shaped specimens (Figure 1.9) are used in this test in order to confine the deformation in the narrow center section (gauge section) and eliminate the possibility of fracture at the ends of the sample.

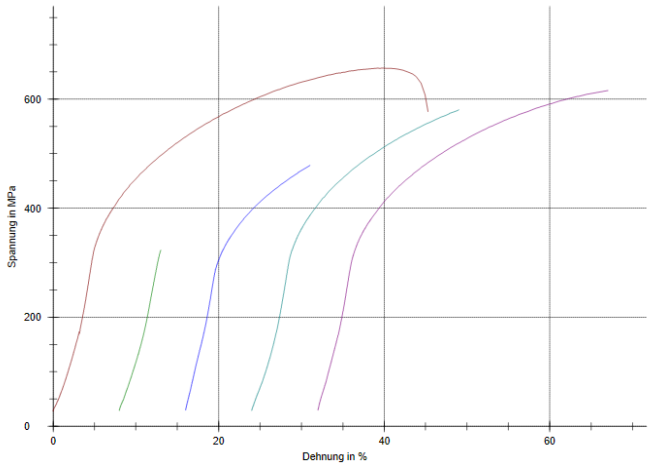

Figure 1.8. Stress-strain curve of the 316L Stainless Steel samples used for the investigation of the attachment and viability behavior of the cells.

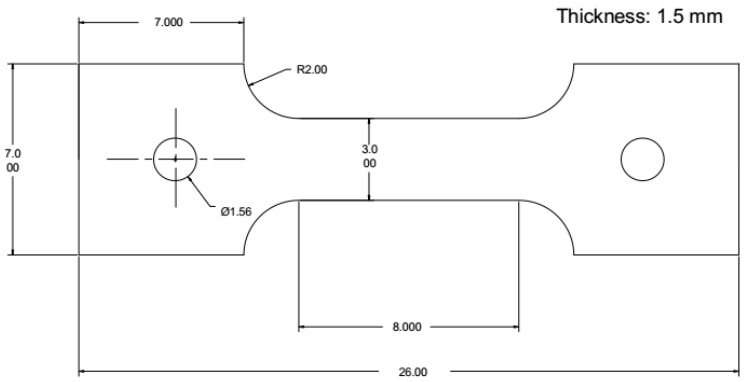

Figure 1.9. The dimensions of the NiCoCr tension samples tested in this thesis.

Characterization of Microstructure

The microstructure of the samples was analyzed via two main techniques: Scanning Electron Microscope (SEM) and Transmission Electron Microscope (TEM). The SEM image is obtained by the scanning of the surface with a focused beam of electrons. These electrons interact with the atoms at different depths within the sample. The types of the signals produced in SEM include secondary electron (SE), back-scattered electrons (BSE) and X-rays. BSE detector was mainly used for the detection of the different phases by the visualization of the contrast on the material while SE detector was utilized to understand the surface topography of the material. In addition energy dispersive X-ray (EDX) detector is used to understand the chemical composition of the material or create the element composition maps. The tested samples can be analyzed via SEM right after they are kindly cleaned with ethanol without destructing the facture surface (Figure 1.10). In order to eliminate the charging problem the metallic samples can be coated with conductive materials or mount with a carbon tape.

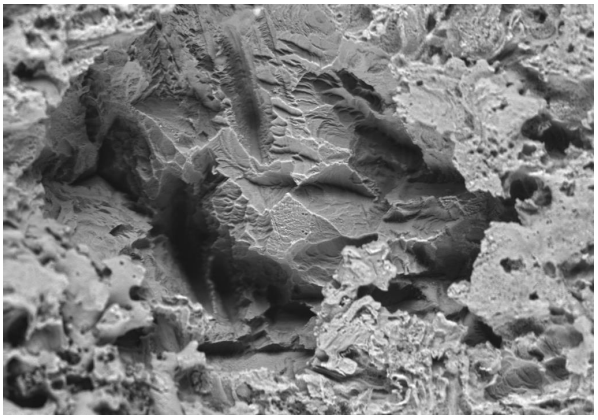

Figure 1.10. The SEM image of the fracture surface of Hadfield steel sample.

On the other hand TEM is imaged is obtained by the transmission of electron beam through the sample which is typically thinner than 100nm (Figure 1.11). While the samples are easily prepared for the SEM analysis, TEM analysis necessitates a toilsome and time consuming sample preparation. The tested samples are firstly ground down to 60 μm thickness with 400 and 600 grit SiC sandpapers and then polished with 1000 and 1200 grit ones respectively. TEM coils in the thickness of nanometers is obtained with twin jet electro polishing equipment. Typically an alcohol is mixed with a strong acid, and the working temperature and the accelerating voltage is determined based on the material.

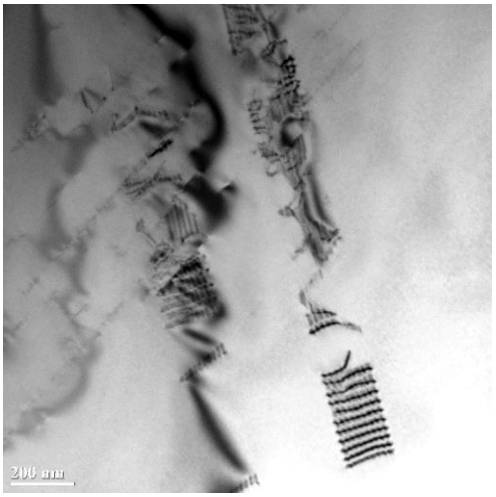

Figure 1.11. TEM image of the NiCoCr sample deformed up to fracture

1.3 References

[1] P. Lan, J. Zhang, Twinning and dynamic strain aging behavior during tensile deformation of Fe-Mn-C TWIP steel, Materials Science and Engineering: A. 700 (2017) 250–258. doi:10.1016/j.msea.2017.06.012.

[2] Z. Zhang, M.M. Mao, J. Wang, B. Gludovatz, Z. Zhang, S.X. Mao, E.P. George, Q. Yu, R.O. Ritchie, Nanoscale origins of the damage tolerance of the high-entropy alloy CrMnFeCoNi., Nature Communications. 6 (2015) 10143. doi:10.1038/ncomms10143.

[3] G. Laplanche, A. Kostka, C. Reinhart, J. Hunfeld, G. Eggeler, E.P. George, Acta Materialia Reasons for the superior mechanical properties of medium-entropy CrCoNi compared to high-entropy CrMnFeCoNi, Acta Materialia. 128 (2017) 292–303. doi:10.1016/j.actamat.2017.02.036.

[4] B. Gumus, B. Bal, G. Gerstein, D. Canadinc, H.J. Maier, F. Guner, M. Elmadagli, Twinning activities in high-Mn austenitic steels under high-velocity compressive loading, Materials Science and Engineering A. 648 (2015) 104–112. doi:10.1016/j.msea.2015.09.045.

[5] B. Bal, B. Gumus, G. Gerstein, D. Canadinc, H.J. Maier, On the micro-deformation mechanisms active in high-manganese austenitic steels under impact loading, Materials Science and Engineering A. 632 (2015) 29–34. doi:10.1016/j.msea.2015.02.054.

[6] D.B. Miracle, O.N. Senkov, Acta Materialia A critical review of high entropy alloys and related concepts, Acta Materialia. 122 (2017) 448–511. doi:10.1016/j.actamat.2016.08.081.

[7] B.J. Yeh, S. Chen, S. Lin, J. Gan, T. Chin, T. Shun, C. Tsau, Nanostructured High-Entropy Alloys with Multiple Principal Elements : Novel Alloy Design Concepts and Outcomes **, (2004) 299–303. doi:10.1002/adem.200300567.

[8] Z. Zhang, H. Sheng, Z. Wang, B. Gludovatz, Z. Zhang, E.P. George, Q. Yu, S.X. Mao, R.O. Ritchie, Dislocation mechanisms and 3D twin architectures generate exceptional strength-ductility-toughness combination in CrCoNi medium-entropy alloy, Nature Communications. 8 (2017) 14390. doi:10.1038/ncomms14390.

[9] B. Gludovatz, A. Hohenwarter, D. Catoor, E.H. Chang, E.P. George, R.O. Ritchie, A fracture-resistant high-entropy alloy for cryogenic applications, 345 (2014).

[10] F. Otto, Y. Yang, H. Bei, E.P. George, Relative effects of enthalpy and entropy on the phase stability of equiatomic high-entropy alloys, Acta Materialia. 61 (2013) 2628–2638. doi:10.1016/j.actamat.2013.01.042.

[11] F. Otto, A. Dlouhý, C. Somsen, H. Bei, G. Eggeler, E.P. George, The influences of temperature and microstructure on the tensile properties of a CoCrFeMnNi high-entropy alloy, Acta Materialia. 61 (2013) 5743–5755. doi:10.1016/j.actamat.2013.06.018.

[12] J. Park, R.S. Lakes, Biomaterials, 3rd Ed.

[13] B. Uzer, S.M. Toker, A. Cingoz, T. Bagci-Onder, G. Gerstein, H.. Maier, D. Canadinc, An exploration of plastic deformation dependence of cell viability and adhesion in metallic implant materials, Journal of the Mechanical Behavior of Biomedical Materials. 60 (2016) 177–186. doi:10.1016/j.jmbbm.2016.01.001.

[14] S.M. Toker, D. Canadinc, H.J. Maier, O. Birer, Evaluation of passive oxide layer formation-biocompatibility relationship in NiTi shape memory alloys: Geometry and body location dependency., Materials Science & Engineering C, Materials for Biological Applications. 36 (2014) 118–29. doi:10.1016/j.msec.2013.11.040.

[15] Q. Chen, G. Thouas, Metallic implant biomaterials, Materials Science and Engineering: R: Reports. 87 (2015) 1–57. doi:10.1016/j.mser.2014.10.001.

[16] B. Uzer, B. Gumus, S.M. Toker, D. Sahbazoglu, D. Saher, C. Yildirim, S. Polat-Altintas,

D. Canadinc, A Critical Approach to the Biocompatibility Testing of Niti Orthodontic Archwires, International Journal of Metallurgy and Metal Physics. 1 (2016) 1–7.

[17] J. Ryhänen, E. Niemi, W. Serlo, E. Niemelä, P. Sandvik, H. Pernu, T. Salo, Biocompatibility of nickel-titanium shape memory metal and its corrosion behavior in human cell cultures., Journal of Biomedical Materials Research. 35 (1997) 451–7. http://www.ncbi.nlm.nih.gov/pubmed/9189823.

[18] J. William D. Callister, D.G. Rethwisch, Materials Science and Engineering SI Version, eighth, 2011.

[19] D. Hull, D.J. Bacon, Introduction to Dislocations, 5th ed., n.d.

[20] J.W. Christian, S. Mahajan, Deformation twinning, Progress in Materials Science. 39 (1995) 1–157. doi:10.1016/0079-6425(94)00007-7.

[21] G.G. Steinmetz, David, Dierk Raabe, A constitutive model of twin nucleation and deformation twinning in high-Mn austenitic TWIP steels, RWTH Aachen, 2013.

[22] B. Gludovatz, A. Hohenwarter, K.V.S. Thurston, H. Bei, Z. Wu, E.P. George, R.O. Ritchie, entropy alloy CrCoNi at cryogenic temperatures, Nature Communications. 7 (2016) 1–8. doi:10.1038/ncomms10602.

[23] S.M. Toker, D. Canadinc, a. Taube, G. Gerstein, H.J. Maier, On the role of slip–twin interactions on the impact behavior of high-manganese austenitic steels, Materials Science and Engineering: A. 593 (2014) 120–126. doi:10.1016/j.msea.2013.11.033.

[24] I. V Kireeva, Y.I. Chumlyakov, Z. V Pobedennaya, Y.N. Platonova, I. V Kuksgauzen, D.A. Kuksgauzen, Slip and twinning in the [149] oriented single crystals of a high-entropy alloy, 59 (2016) 106–113. doi:10.1007/s11182-016-0898-1.

[25] I. Karaman, H. Sehitoglu, K. Gall, Y.I. Chumlyakov, H.J. Maier, Deformation of single

crystal hadfield steel by twinning and slip, Acta Materialia. 48 (2000) 1345–1359. doi:10.1016/S1359-6454(99)00383-3.

[26] D. Canadinc, H. Sehitoglu, H.J. Maier, D. Niklasch, Y.I. Chumlyakov, Orientation evolution in Hadfield steel single crystals under combined slip and twinning, International Journal of Solids and Structures. 44 (2007) 34–50. doi:10.1016/j.ijsolstr.2006.04.011.

[27] I. Karaman, H. Sehitoglu, a. . Beaudoin, Y.. Chumlyakov, H.. Maier, C.. Tomé, Modeling the deformation behavior of Hadfield steel single and polycrystals due to twinning and slip, Acta Materialia. 48 (2000) 2031–2047. doi:10.1016/S1359-6454(00)00051-3.

[28] I. Kireeva, Y. Chumlyakov, Z. Pobedennaya, Mechanisms of Plastic Deformation in [111] Oriented Single Crystals of FeNiMnCrCo High Entropy Alloy, 20090 (2016) 1–5. doi:10.1063/1.4966383.

2. AN EXPLORATION OF PLASTIC DEFORMATION DEPENDENCE OF CELL VIABILITY AND ADHESION IN METALLIC IMPLANT MATERIALS

2.1 Introduction

Cell viability and adhesion on an implant material play an important role for the biocompatibility of the material and dictate the success of long-term tissue-implant integration [1–15]. Especially when the physical and chemical properties of the implant surface can mimic those of the biological structure, a successful tissue-implant integration is achieved as the cells attach to, and spread and grow on the implant surface [11,16]. This, in turn, proves very effective in minimizing the risk of inflammatory reactions [17].

The materials of choice for the metallic implants have most commonly been stainless steels, cobalt-chrome alloys, and titanium and its alloys [2,18–22] They usually exhibit good formability, high strength, and wear and corrosion resistance, as well as acceptable long-term biocompatibility [4,20,22–25]. When the implant material is placed in the body, cells recognize special ligands on the implant surface through their focal contacts [26,27]. The ligands can either be on the membrane of an adjacent cell, or can be a part of the extracellular matrix (ECM) [1,27,28]. If cells can successfully attach on these ligands through their focal contacts, they can then adhere and spread on the implant material [1]. Especially the first hours of the cell-implant interactions are very critical for the adhesion behavior of the cells: if good cell-implant attachment and viability is achieved right after the placement of the implant into the host body, the surface will be resistant to bacterial attacks. This will increase the life span of the implant and improve the quality of the treatment. If, on the other hand, cells cannot attach on the substrate and instead bacteria colonize on the implant surface, tissue-implant integration will fail [9].

Physical and chemical properties of an implant's surface play a significant role in achieving a successful cell-implant attachment [1,13,16,22]. Specifically, roughness, polarity, hydrophilicity and free energy of the surface are the most critical factors affecting the cell-implant

interaction [11,16,29]. Surface free energy (SFE) and wettability of the material surface enhance the cell attachment because cellular proteins responsible for attachment are attracted more to the surface [16,29,30]. Surface roughness also constitutes an important parameter for the cell viability and attachment because it changes the chemical and physical properties of the material surface directly, which, in turn, affect the cell response to the implant. For example, cell attachment is reported to increase concomitant with surface roughness owing to a higher surface energy and serums moving into grooves [6,10,13,29,31].

In order to characterize the surface roughness effect on cell viability and attachment, numerous machining and patterning methods were utilized [3,18,32]. Focal adhesion formation and spread area of the cells were investigated on different potential implant materials and the importance of the cell-implant interactions was reported [14]. In addition, numerous surface modification techniques were utilized to obtain implants with different physical and chemical properties, including lithography or etching [5,15,33]. As a result, micron and submicron scale features mimicking the real biological components were obtained, which resulted in enhanced cell viability and a better adhesion [8,11,12,31,33]. These studies also showed that physical modifications on implant surfaces can lead to chemical changes, which, in turn, significantly influence the cell response.

The findings of the aforementioned studies evidenced a better cell viability and adhesion behavior on implant surfaces modified with various techniques. However, all these methods were confined to the macroscopic investigations that involved modifications on the implant surface either with generating different surface features or changing the groove sizes. To the best of the authors' knowledge, a study presenting a clear relationship between the cell response and the true reason for the surface roughness, i.e. micro-deformation mechanisms, has not been forwarded yet. In particular, understanding the role of micro-deformation mechanisms on the cell response to the corresponding implant surface might be of utmost importance since parameters dictating

the cell adhesion and viability, such as surface roughness or surface energy, are directly dictated by the deformation of the surface at the micro-scale. The current study was undertaken with the motivation of addressing this issue, and to investigate the cell response to different micro-deformation mechanisms, such as slip and twinning.

In the current study, viability and adhesion behavior of the cells, and the corresponding dependence on the micro-deformation mechanisms were investigated on austenitic 316L stainless steel samples because among all the other metallic materials, the utility of stainless steels as biomaterials dates back to earlier years, and thus, this class of materials has been investigated in detail in terms of their mechanical properties, microstructure, and interactions with living cells [7,20,24,34,35]. The 316L stainless steel samples were subjected to tensile loading and deformed up to plastic strains of 5%, 15%, 25% and 35%. As widely as the stainless steels are utilized as implant materials in orthopedics or cardiovascular diseases [4], they are also used in the treatment of neurological diseases such as full or partial paralysis, and Parkinson's disease, where implanted stainless steel electrodes are employed to stimulate the targeted brain regions with the aid of electric signals [36–38]. Another example is cranioplasty, which involves the utility of stainless steel mesh to repair large cranial defects, which might come into contact with the outer brain tissue [39]. Thus, for the sake of observing the most possible cell viability and adhesion behavior, highly adhesive and replicative malignant brain tumor cells (U373) were seeded on the samples. In particular, the quick and adhesive response of these cells was very useful in investigating their viability and adhesion behavior within short observation periods. The current findings revealed that the U373 cells showed higher cell viability and adhesion on the sample deformed to the largest strain, featuring the highest density of micro-deformation activities, and filopodia formation was observed as the strain increased.

Overall, the current set of results demonstrates that cell response on a metallic implant can be controlled by controlling plastic deformation during the making of the implant, and thus,

by activating the desired micro-deformation mechanisms. Furthermore, the cell reaction data to different microstructures and surface properties can be useful to tailor the properties of implant material in order to obtain the surface and microstructure that would stimulate the highest cell viability and adhesion. As a result, a better cell-implant interaction can be achieved, inflammatory and adverse reactions can be reduced or even eliminated, and the quality of the treatment can be improved. More importantly, the current results open the venue for utilizing microscopic level live tissue - metallic material relationship to facilitate new medical treatments.

2.2 Materials and Methods

For mechanical tests, dog bone shaped tensile test specimens were cut from 316L stainless steel sheets, which were then ground with 400, 800, 1200 and 2500 grit SiC papers, and polished with diamond abrasives having particle sizes of 0.6μm, 0.3μm and 0.1μm respectively. The polished samples were etched to observe the microstructure more clearly. The etching reagent was prepared by mixing 200 ml distilled water, 200 ml HCl (32%), 20 ml HNO_3 (65%) and 0.6 ml Vogel's inhibitor at a working temperature of 70 °C. To obtain the samples with different microstructures, the polished and etched steel samples were subjected to tensile loading with a servo hydraulic test machine and deformed up to four different strains: 5%, 15%, 25% and 35%. A different sample geometry was utilized in order to strain the samples to 60%, such that the cell viability could be observed for an extreme deformation case. This wide range of strains stimulated topographical variations and activation of micro-deformation mechanisms in different volume fractions on each sample. It should be noted that the steel sheet deformed up to the failure strain (40%) was not included in the viability and adhesion tests because the localization of the stresses and strains in the vicinity of the fracture surfaces would result in a significant deviation from the overall test results. Prior to seeding the cells, the deformed samples were polished with 0.1μm particle-sized diamond abrasive to remove traces of the etchant. However,

the etchant traces on the samples deformed up to 25% and 35% were not fully removed by this procedure. Therefore, they were also polished utilizing a vibratory polisher for 12 hours.

For the cell culture experiments samples with the dimensions of 10 mm × 10 mm × 1 mm were obtained from the gauge section of each 316L steel sheet by electrical discharge machining (EDM), and three companion cell culture experiments were carried out to check for repeatability. Samples were cleaned in an ultrasound bath with ethanol for 15 minutes prior to the experiments and microscopy. Surface topography and the corresponding roughness of each sample were monitored with confocal laser scanning microscopy (CLSM) at 50 × and 150 × magnifications. The average surface roughness (Ra) values of the samples were evaluated utilizing the scans carried out at 50 × magnification, and by taking the average of scans obtained from 5 different areas with a scan area of 50μm × 50μm on each sample surface. In order to assess the suitability of the steel samples for cell growth, a highly malignant cell type with good attachment characteristics was chosen: the U373 glioblastoma cell line was engineered to express green fluorescent protein (GFP) and seeded on the steel samples featuring five different deformation strains: 0%, 5%, 15%, 25% and 35%. The U373 human glioblastoma cells were obtained from the American Type Culture Collection (ATCC) and grown in standard culture conditions in DMEM supplemented with 10% FBS and 1% Penicillin-Streptomycin (Gibco). Cells were then engineered to express GFP using retroviral transduction as described elsewhere [40]. Accordingly, cells were transduced with pBabeGFP viral particles in medium containing protamine sulfate (10 mg/ml) at a multiplicity of infection (MOI) of 1. GFP expression was visualized by fluorescence microscopy. The U373 cells possessed an average dimension of 18 μm × 13 μm.

Sterilization of the 316L stainless steel samples was accomplished utilizing an autoclave. Each sterile sample was added to one well of a 24-well tissue culture plate (Costar), followed by cell seeding. 1×10^5 U373-GFP cells were seeded on each well containing a steel sample in 1 ml growth medium for 24 hours. Next day, the metal samples with the attached GFP-positive cells

were observed with fluorescence microscopy. Upon fluorescence imaging, the number of cells attached per sample was measured using ATP-based cell viability assays. Accordingly, Cell Titer-Glo® (CTG) Luminescent Cell Viability Assay (Promega, USA) was modified to measure cell viability on the steel samples. For each well, 30 µl CTG reagent was mixed with 300 µl DMEM, and this mixture was added into the well on the metal sample. After a 10 minute incubation period, 100 µl of cell and CTG mixture was transferred to a 96-well plate and was measured by a luminometric plate reader (Synergy H1 Reader, Biotek, USA).

Steel surfaces and cell attachment were also monitored with the addition of field emission scanning electron microscopy (FESEM). The FESEM images of the steel sample surfaces prior to the cell seeding were captured with secondary electron (SE) and an inlens detector at a magnification in the range of 300 – 5000 ×, under an accelerating voltage of 7 kV and current of 278 – 785 pA, and within a working distance of 5.1 – 8.9 mm. The FESEM images of the cell-seeded steel samples were also captured with SE and an inlens detector, but at a magnification of 300 – 4000 ×, under an accelerating voltage of 5 kV and current of 278 – 785 pA, and within a working distance of 6.3 – 8 mm.

2.3 Results and Discussion

The CLSM and FESEM analyses carried out prior to seeding the cells revealed topographical and microstructural distinctions between the samples deformed to different plastic strains (5%, 15%, 25%, 35% and 60%). In particular, as the plastic deformation increased, surface topography of the samples became rougher (Figure 2.1), while the undeformed sample had a rather smooth surface. CLSM was employed in order to quantify the differences between surface topographies of the undeformed and deformed steel samples: topographic representations of the surface heights, also referred to as height images, in Figure 2.2 show prominent differences between the samples, such that an increased density of valleys and peaks, and larger grooves

became more prevalent concomitant with plastic strain increase, which resulted in a greater average surface roughness (Ra) as expected (Table 2.1).

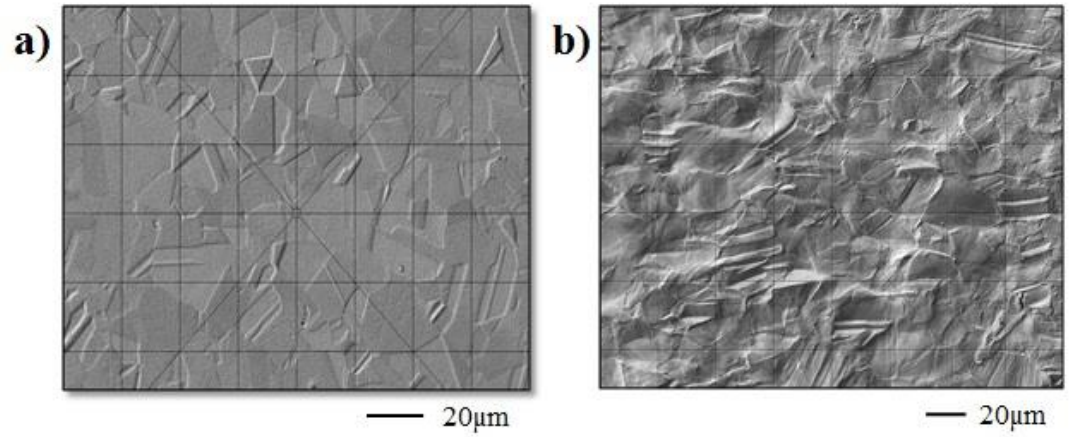

Figure 2.1. FESEM images showing the microstructure and surface texture of **(a)** the undeformed and **(b)** 35% deformed 316L steel samples. Grids appearing on the images helped focusing on the same specific areas of interest under different magnifications.

Table 2.2. Average surface roughness (Ra) data of the undeformed and deformed steel samples in μm obtained by CLSM.

Undeformed	**5%**	**15%**	**25%**	**35%**
0.043 ± 0.002	0.090 ± 0.002	0.250 ± 0.035	0.457 ± 0.016	0.624 ± 0.045

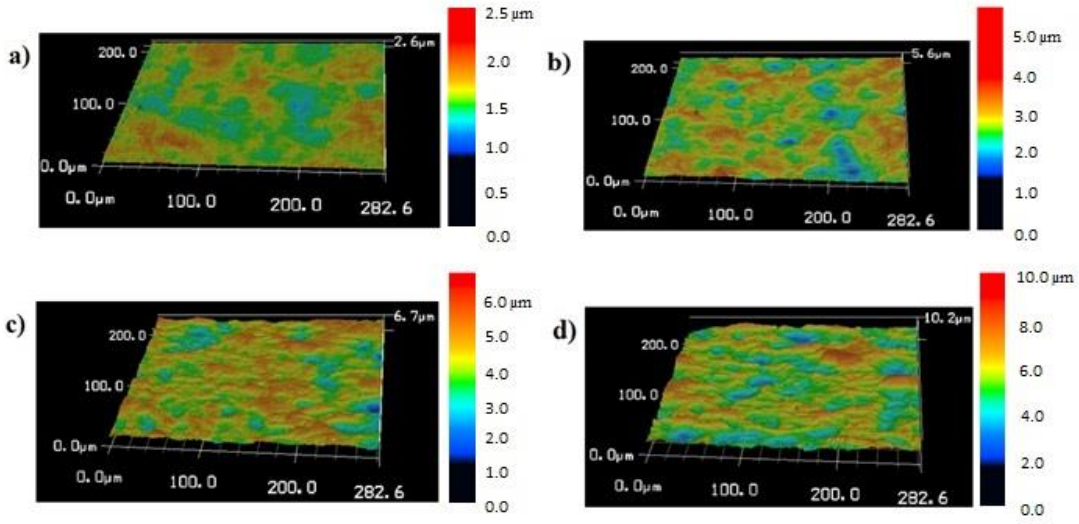

Figure 2.2. Topographic representations of the surface heights (height images) of the samples deformed up to **(a)** 5%, **(b)** 15%, **(c)** 35% and **(d)** 60%.

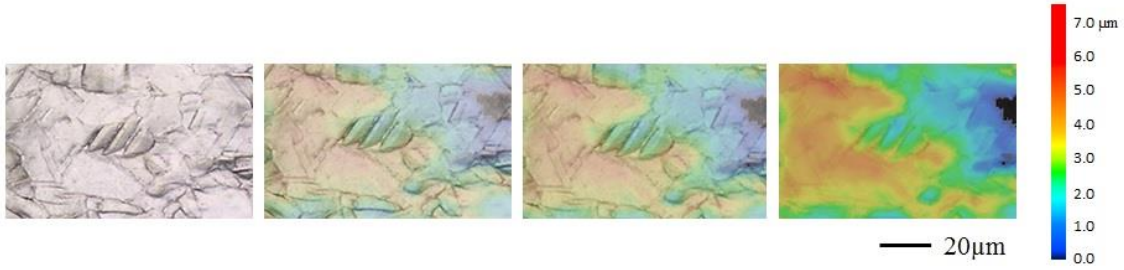

Figure 2.3. Traces of mechanical twins on the surface of the 35% deformed sample. This gradual transition was obtained by superposing the topography and surface images, and adjusting the transparency of the images. The color bar shows the surface roughness defined in terms of peak distance values along the z axis (in µm).

The microstructure of each sample was also investigated in detail with CLSM and FESEM in order to relate the surface roughness to the micro-deformation mechanisms. For instance, as the deformation increased the volume fraction of mechanical twins also increased accompanying the roughness evolution, as recently reported in the literature [25]. In order to gain a better understanding of the role of twinning on the surface roughness, the 35% deformed sample, which featured the largest volume of mechanical twins, was investigated in detail under CLSM: superposition of the height and laser scanning images (also referred to as laser image)

obtained from a twinned region on this sample clearly demonstrated the contribution of twins to the surface roughness, especially when the transparency of one of the images was adjusted accordingly (Figure 2.3). The CLSM line profile of this particular region (Figure 2.4) shows the abrupt changes on the texture stemming from twinning [41]. Even though such an abrupt change can also be observed on an undeformed sample due to pre-existing twins, plastic deformation significantly increases the incidence of such twin-related abrupt changes along with increasing roughness [25]: grains oriented along the <101> orientation exhibited extensive twinning upon plastic deformation, implying that an initial texture with the majority of the grains assuming <101> or near-<101> orientations can provide an effective means of increasing surface roughness upon plastic deformation by facilitating the maximum twinning activity.

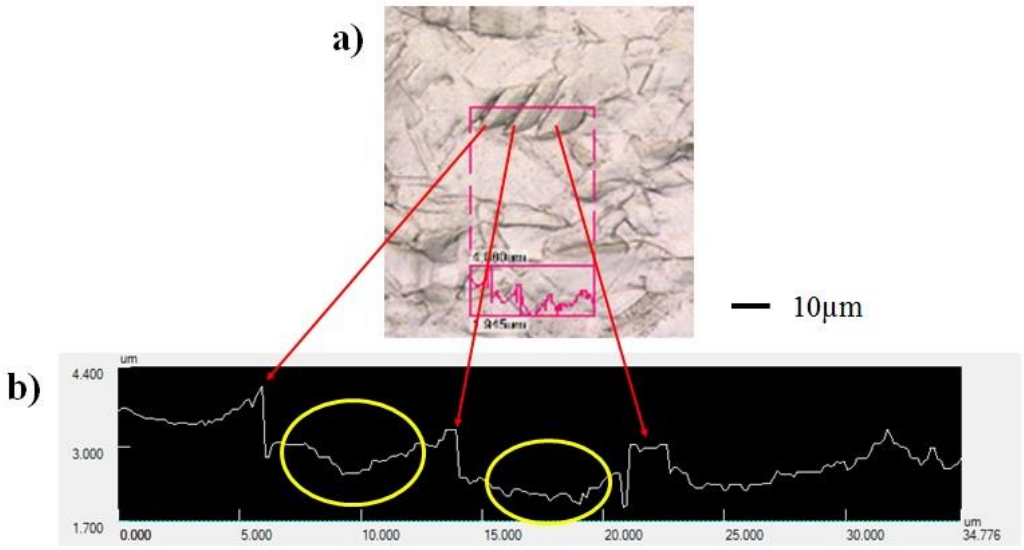

Figure 2.4. CLSM line profile traversing a twinned region on the sample deformed to 35% strain. The encircled areas exhibit a stair-like line profile, where the surface topography changes abruptly, which is characteristic of twinning.

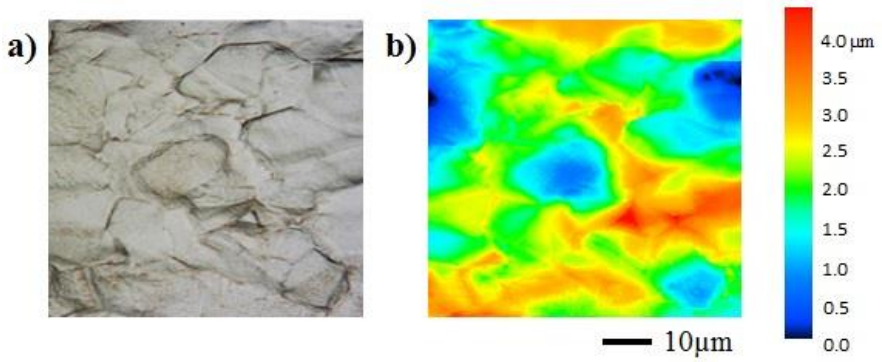

Figure 2.5. (a) Laser **(b)** and height images of grains showing overall surface topography of the sample deformed to 35%. The color bar represents the surface roughness defined in terms of peak distance values along the z axis (in µm).

The laser and height images of the surface of the 35% deformed sample evidence that the surface topography is also governed by the individual orientations of the grains, i.e. the texture of the material (Figure 2.5): due to plastic deformation each grain was reoriented along towards a direction dictated by the loading and material symmetry [42], and identified itself with the resulting surface roughness defined in terms of peak distance values along the normal to the surface. Consequently, the misorientation angle between the neighboring grains also plays an important role since it also increases upon plastic deformation [25,43]. In order to further clarify this point, the boundary between two neighboring grains on the surface of the 35% deformed sample was subjected to CLSM line profiling (Figure 2.6). Accordingly, the line profile shows a sudden drop of the height while traversing the grain boundary, similar to those observed in the twinned regions (encircled zones in Figure 2.4(b)) yet of larger magnitude.

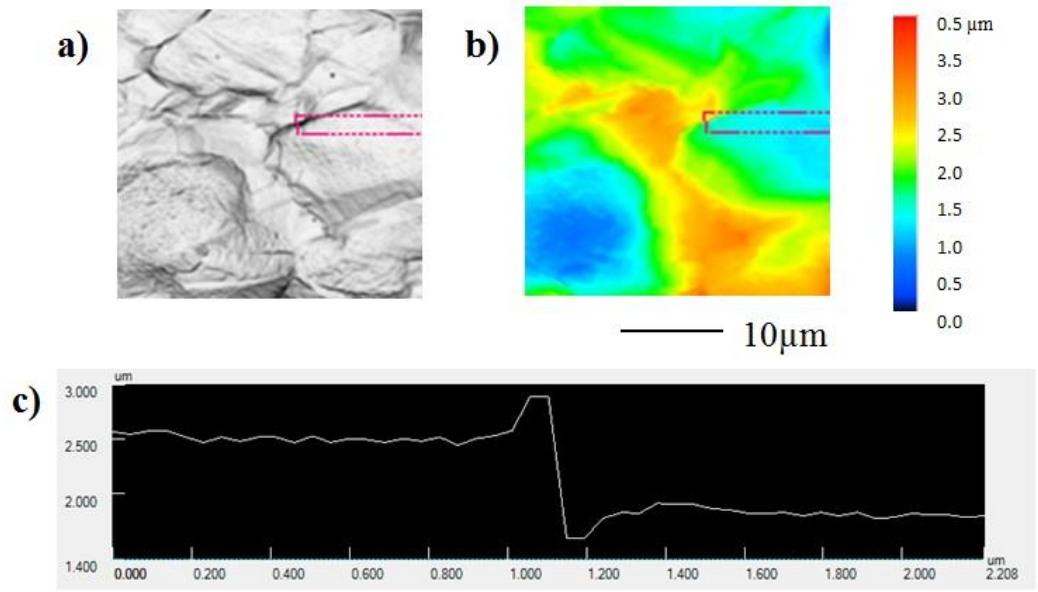

Figure 2.6. (a) Laser **(b)** and height images of the boundary of two neighboring grains on the sample deformed to 35% of strain. **(c)** Line profile obtained from the areas marked in the images (a) and (b) showing the sudden drop in surface height. The color bar shows the surface roughness defined in terms of peak distance values along the normal to the surface (in µm).

The other major micro-deformation mechanism, i.e. slip, became more prevalent with increasing plastic deformation, such that the slip lines are clearly visible on the surface (Figures 2.7 and 8). In addition, as the deformation of the 316L steel proceeded, multiple slip systems became active, eventually leading to twin-slip interactions within the grains (Figure 2.7), also contributing to the strain hardening capacity of the material [41]. As a result of these interactions, twins curtail the dislocation activity [44] and stress concentration increases at these sites [25]. More importantly, the greater surface energy of these regions can later catalyze the adhesion of the cells or deposition of biological molecules [21], and thus, the slip lines were analyzed in detail on the 35% deformed sample. Figure 8 shows the planar slip lines within a grain and a line profile traversing over these slip lines, evidencing the significant contribution of glide dislocations to the surface roughness that dictates the cell adhesion and viability.

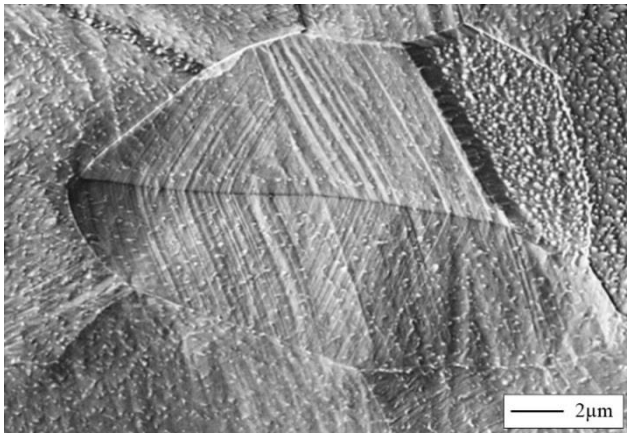

Figure 2.7. FESEM image showing a grain on the sample deformed to 25% strain: twin-slip interactions are prominent within this grain.

FESEM analysis carried out after cells were seeded and fixated on the samples having different levels of plastic deformation revealed that cells displayed a highly attached and spread morphology on deformed steel samples, whereas they did not properly attach to undeformed samples (Figure 2.9). Furthermore, the abundance of filopodial extensions indicates the higher surface affinity of the cells on the deformed samples (Figure 2.9-b), especially on 35% strained samples. These cells were wider and displayed several extensions reminiscent of actin-based filopodia. In addition, intercellular attachment was also observed on the deformed samples (Figures 2.9), where the neighboring cells recognized each other through the membrane proteins and attached with their filopodia. In contrast, the cells that attached to undeformed samples spread on a smaller area without any filopodia. This set of findings implies that an enhanced activity of micro-deformation mechanisms promotes cell attachment and proliferation.

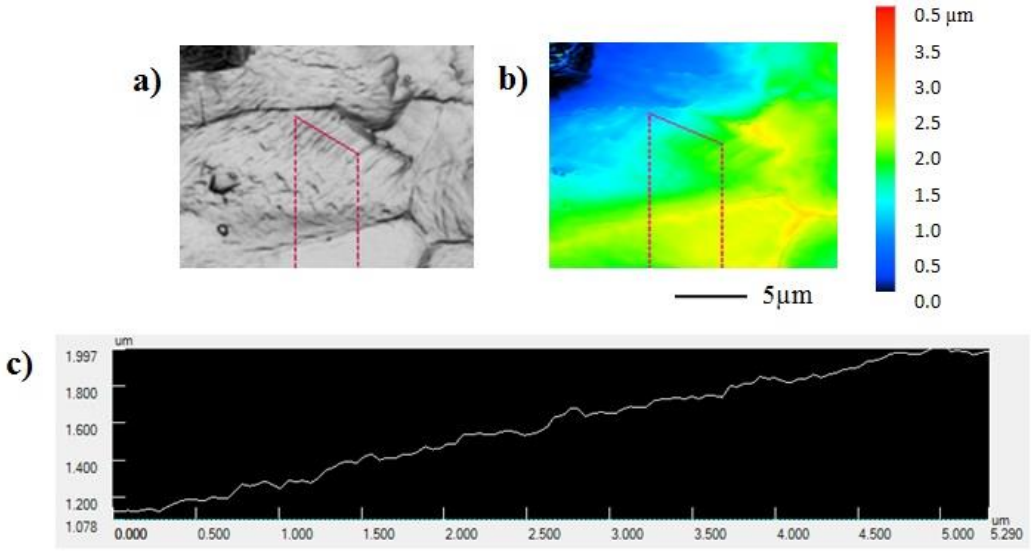

Figure 2.8. (a) Laser **(b)** and height images of the slip lines within a grain in the sample deformed to 35% strain. **(c)** The line profile shows the step-like increase of the surface height by the slip lines within the region marked in (a) and (b). The color bar shows the surface roughness defined in terms of peak distance values along the normal to the surface (in µm).

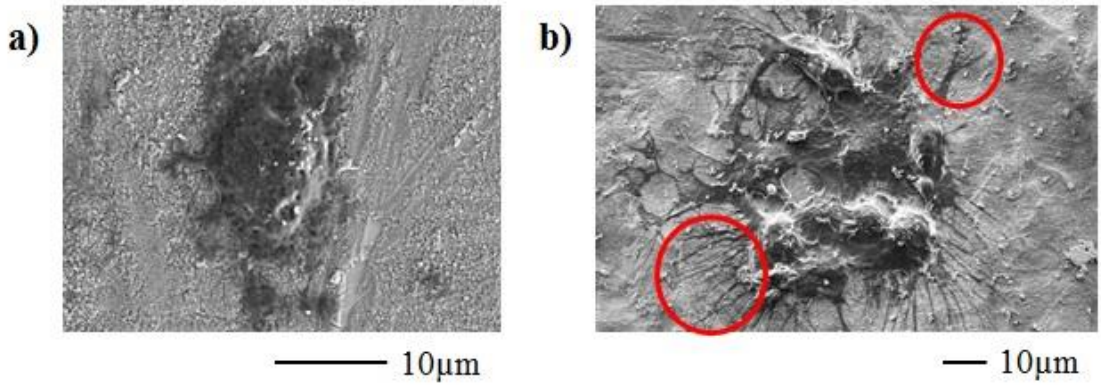

Figure 2.9. FESEM images of the cells cultured on **(a)** the undeformed, and **(b)** the 35% deformed sample, demonstrating the plastic deformation effect on the spread morphology of the cells. The encircled zones indicate the filopodial extensions.

In order to further investigate this argument, a different set of samples was prepared, such that the samples were thin sheets of rectangular shape with dimensions of 200 mm × 50 mm × 1 mm. In this configuration, 60% of strain was attained during tensile loading. Cell adhesion on these samples was imaged by a fluorescent microscope after 24 hours of incubation time (Figure 2.10): the number of cells attached to the deformed samples was markedly higher

than the number of cells attached to the undeformed samples. ATP-based luminometric viability measurements showed 5.33 ± 0.96 fold greater cell viability on the 60% deformed sample in comparison with the undeformed samples. While the deformation strain and cell viability did not linearly correlate, cell attachment and viability reached the highest levels on the most deformed samples, i.e. at 60% strain, for the U373 cells.

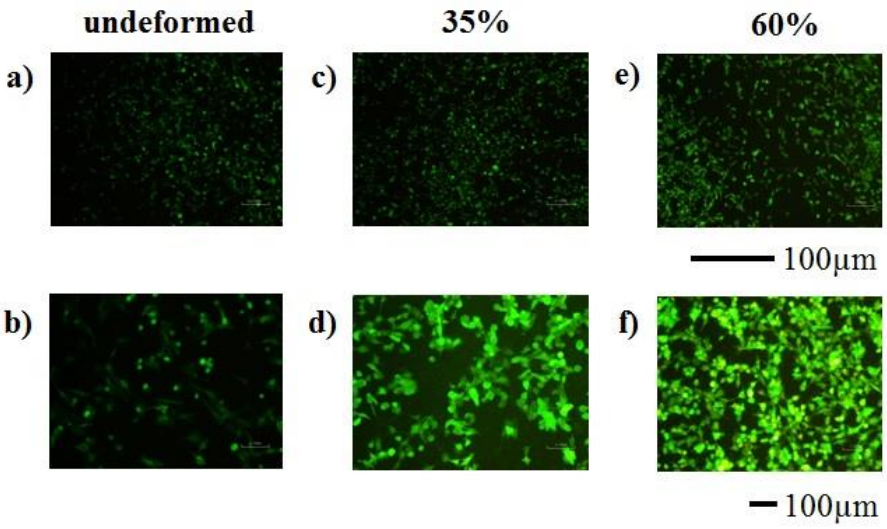

Figure 2.10. Fluorescent microscopy images of the undeformed samples (**(a)** and **(b)**), and those deformed up to 35% (**(c)** and **(d)**) and 60% (**(e)** and **(f)**). The lower row shows high magnification areas from the overviews shown in the top row.

Higher viability and enhanced adhesion behavior of the cells were previously correlated with the increase in the groove size and roughness upon deformation [2,5]. Specifically, the denser and larger valleys and peaks due to plastic deformation led to larger groove size and enhanced roughness, and the largest plastic deformation catalyzed the maximum cell adhesion. Furthermore, as the groove size and surface area become enlarged, the cells adhere on the surface with covering the entire groove [5,29] possibly through the adsorption of the actin binding proteins needed for the cell attachments in these grooves [6]. The current set of results align well with these previous observations, however; none of these works explored the role of micro-

deformation mechanisms, namely twinning and slip, as well as their interactions, on the cell response to the metallic surface. The current findings demonstrate that the micro-deformation mechanisms indeed dictate both the surface roughness and the cell response to the metallic surface, and constitute the primary parameters in optimizing the cell attachment and viability: cells spread on the surface more extensively and exhibited the cytoplasmic extensions which also made the interconnection of the cells possible. In addition, the high energy of the twin-slip interaction sites eased the cell attachment as the cells spent less energy for attachment.

These arguments imply that surface roughness can be directly controlled by micro-deformation mechanisms, i.e. slip and twinning. In particular, adjusting the relative activities and volume fractions of these mechanisms can have a similar effect to that of surface modification techniques to obtain the ideal surface roughness for the cell attachment [12]. For instance, the regions marked with the yellow circles in Figure 2.4 show similarity with the shape of the grooves. Cells can form focal attachment points on these regions, which can enhance the adhesion [6,10,13,29,31]. This, in turn, implies that cell adherence on an implant surface can be improved further by optimizing the surface topography through facilitation of the corresponding twinning activity during manufacturing of the implant.

It was also noted that culturing of the cells on the deformed steel samples was more favorable than seeding them on undeformed samples in terms of their attachment efficiency and viability. This also suggests that deformed steel samples are more biocompatible, allowing for efficient interaction with surrounding cells *in vivo*, which is consistent with previously published work on the relation of osteoblasts [13] or human dermal fibroblasts [45] with artificial material surfaces. Despite these encouraging implications, the current set of results also warrants further investigation to better understand the individual roles of the micro-deformation mechanisms and their interactions, which can eventually open a new venue for the selection and production of the

implant materials that are most favored by the cells of the surrounding tissue, and ensure an improved clinical treatment.

2.4 Conclusions

Cell viability and adhesion behavior of U373 brain tumor cells were investigated on 316L stainless steel samples that were deformed to strains of 5%, 15%, 25% and 35% in order to facilitate varying degrees of micro-deformation mechanism activities. Confocal laser scanning microscopy (CLSM) showed that surface roughness increased concomitant with the plastic deformation, and the topographical representation of the height images obtained from grain boundaries, twinned regions and slip lines revealed that all of these microstructural features have a direct influence on the surface topography. CLSM and field emission scanning electron microscopy (FESEM) results demonstrated that increased deformation enhanced both cell adhesion and filopodial extension of the cells, indicating the affinity of the cells to the surface. Specifically, the cells spread more on the surface by also interconnecting with the other cells, and slip-twin interactions can create high energy sites, which could further catalyze cell adhesion or deposition of biological molecules. Moreover, the maximum viability was obtained upon culturing the cells on the samples that were plastically deformed the most. Overall, the current set of results both warrants further elaboration on the individual roles of the micro-deformation mechanisms and their interactions on the cell response to the metallic surface, and opens a new venue for the selection and production of implant materials that will ensure improved clinical treatments relying on metallic implants.

In order to understand whether a different cell type would react in a similar way or not this study was followed by analyzing the viability and adhesion behavior of fibroblast cells on the plastically deformed steel samples. The findings of this study will be explained in detail in the next chapter.

2.5 Rerefences

[1] K. Anselme, Osteoblast adhesion on biomaterials, Biomaterials. 21 (2000) 667–681. doi:10.1016/S0142-9612(99)00242-2.

[2] S. Bauer, P. Schmuki, K. Von Der Mark, J. Park, Progress in Materials Science Engineering biocompatible implant surfaces Part I : Materials and surfaces, Progress in Materials Science. 58 (2013) 261–326. doi:10.1016/j.pmatsci.2012.09.001.

[3] M. Bigerelle, K. Anselme, B. Noël, I. Ruderman, P. Hardouin, a. Iost, Improvement in the morphology of Ti-based surfaces: a new process to increase in vitro human osteoblast response, Biomaterials. 23 (2002) 1563–1577. doi:10.1016/S0142-9612(01)00271-X.

[4] Q. Chen, G.A. Thouas, Metallic implant biomaterials, Materials Science and Engineering R: Reports. 87 (2015) 1–57. doi:10.1016/j.mser.2014.10.001.

[5] A. Curtis, C. Wilkinson, Topographical control of cells, Biomaterials. 18 (1997) 1573–1583. doi:10.1016/S0142-9612(97)00144-0.

[6] D.D. Deligianni, N. Katsala, S. Ladas, D. Sotiropoulou, J. Amedee, Y.F. Missirlis, Effect of surface roughness of the titanium alloy Ti6Al4V on human bone marrow cell response and on protein adsorption, Biomaterials. 22 (2001) 1241–1251.

[7] M.H. Fathi, M. Salehi, a. Saatchi, V. Mortazavi, S.B. Moosavi, In vitro corrosion behavior of bioceramic, metallic, and bioceramic-metallic coated stainless steel dental implants, Dental Materials. 19 (2003) 188–198. doi:10.1016/S0109-5641(02)00029-5.

[8] R. Flemming, C. Murphy, G. Abrams, S. Goodman, P. Nealey, Effects of synthetic micro- and nano-structured surfaces on cell behavior, Biomaterials. 20 (1999) 573–588.

[9] a G. Gristina, Biomaterial-centered infection: microbial adhesion versus tissue integration., Science (New York, NY). 237 (1987) 1588–1595.

doi:10.1126/science.3629258.

[10] G. Gronowicz, M.B. McCarthy, Response of human osteoblasts to implant materials: integrin- mediated adhesion, Journal of Orthopaedic Research. 14 (1996) 878–887.

[11] B. Kasemo, J. Gold, Implant surfaces and interface processes, Advances in Dental Research. 13 (1999) 8–20. doi:10.1177/08959374990130011901.

[12] L. Le Guéhennec, A. Soueidan, P. Layrolle, Y. Amouriq, Surface treatments of titanium dental implants for rapid osseointegration, Dental Materials. 23 (2007) 844–854. doi:10.1016/j.dental.2006.06.025.

[13] U. Meyer, A. Büchter, H.P. Wiesmann, U. Joos, D.B. Jones, Basic reactions of osteoblasts on structured material surfaces, European Cells and Materials. 9 (2005) 39–49.

[14] N. Turner, M. Armitage, R. Butler, G. Ireland, An in vitro model to evaluate cell adhesion to metals used in implantation shows significant differences between palladium and gold or platinum., Cell Biology International. 28 (2004) 541–7. doi:10.1016/j.cellbi.2004.04.009.

[15] H. Watanabe, K. Saito, K. Kokubun, H. Sasaki, M. Yoshinari, Change in surface properties of zirconia and initial attachment of osteoblastlike cells with hydrophilic treatment, Dental Materials Journal. 31 (2012) 806–814. doi:10.4012/dmj.2012-069.

[16] L. Ponsonnet, K. Reybier, N. Jaffrezic, V. Comte, C. Lagneau, M. Lissac, C. Martelet, Relationship between surface properties (roughness, wettability) of titanium and titanium alloys and cell behaviour, Materials Science and Engineering: C. 23 (2003) 551–560. doi:10.1016/S0928-4931(03)00033-X.

[17] D.G. Castner, B.D. Ratner, Biomedical surface science: Foundations to frontiers, 2002. doi:10.1016/S0039-6028(01)01587-4.

[18] K. Anselme, M. Bigerelle, Topography effects of pure titanium substrates on human

osteoblast long-term adhesion., Acta Biomaterialia. 1 (2005) 211–22. doi:10.1016/j.actbio.2004.11.009.

[19] L.O. Bailey, S. Lippiatt, F.S. Biancanello, S.D. Ridder, N.R. Washburn, The quantification of cellular viability and inflammatory response to stainless steel alloys., Biomaterials. 26 (2005) 5296–302. doi:10.1016/j.biomaterials.2005.01.055.

[20] K. Bordji, J.Y. Jouzeau, D. Mainard, E. Payan, J.P. Delagoutte, P. Netter, Evaluation of the effect of three surface treatments on the biocompatibility of 316L stainless steel using human differentiated cells., Biomaterials. 17 (1996) 491–500. doi:10.1016/0142-9612(96)82723-2.

[21] S.M. Toker, D. Canadinc, Evaluation of Biocompatibility of NiTi Dental Wires: A Comparison of Laboratory Experiments and Clinical Conditions, Materials Science and Engineering: C. 40 (2014) 142–147. doi:10.1016/j.msec.2014.03.060.

[22] S.M. Toker, D. Canadinc, H.J. Maier, O. Birer, Evaluation of passive oxide layer formation-biocompatibility relationship in NiTi shape memory alloys: Geometry and body location dependency., Materials Science & Engineering C, Materials for Biological Applications. 36 (2014) 118–29. doi:10.1016/j.msec.2013.11.040.

[23] K. Kato, A. Yamamoto, S. Ochiai, M. Wada, Y. Daigo, K. Kita, K. Omori, Cytocompatibility and mechanical properties of novel porous 316 L stainless steel, Materials Science and Engineering C. 33 (2013) 2736–2743. doi:10.1016/j.msec.2013.02.038.

[24] F.B.M. Martinesi, S.Bruni, M. Stio, C. Treves, T. Bacci, Biocompability, Journal of Biomedical Materials Research Part A. 81 (2006) 131–145. doi:10.1002/jbm.a.

[25] S. Sinha, J. a. Szpunar, N. a. P. Kiran Kumar, N.P. Gurao, Tensile deformation of 316L austenitic stainless steel using in-situ electron backscatter diffraction and crystal plasticity

simulations, Materials Science and Engineering: A. 637 (2015) 48–55. doi:10.1016/j.msea.2015.04.005.

[26] K. Burridge, K. Fath, T. Kelly, G. Nuckolls, C. Turner, Focal adhesions: transmembrane junctions between the extracellular matrix and the cytoskeleton., Annual Review of Cell Biology. 4 (1988) 487–525. doi:10.1146/annurev.cellbio.4.1.487.

[27] D. Lehnert, B. Wehrle-Haller, C. David, U. Weiland, C. Ballestrem, B. a Imhof, M. Bastmeyer, Cell behaviour on micropatterned substrata: limits of extracellular matrix geometry for spreading and adhesion., Journal of Cell Science. 117 (2004) 41–52. doi:10.1242/jcs.00836.

[28] B.M. Gumbiner, Cell adhesion: The molecular basis of tissue architecture and morphogenesis, Cell. 84 (1996) 345–357. doi:10.1016/S0092-8674(00)81279-9.

[29] B.D. Boyan, T.W. Hummert, D.D. Dean, Z. Schwartz, Role of material surfaces in regulating bone and cartilage cell response., Biomaterials. 17 (1996) 137–46. http://www.ncbi.nlm.nih.gov/pubmed/8624390.

[30] C.L. Wexell, Bone Response to Surface-Modified Titanium Implants : Studies on the Early Tissue Response to Implants with Different Surface Characteristics, International Journal of Biomaterials. 2013 (2013). doi:http://dx.doi.org/10.1155/2013/412482.

[31] G. Zhao, L. Raines, M. Wieland, Z. Schwartz, B.D. Boyan, Requirement for both micron- and submicron scale structure for synergistic responses of osteoblasts to substrate surface energy and topography, Biomaterials. 28 (2007) 2821–2829. doi:10.1016/j.biomaterials.2007.02.024.

[32] D. Falconnet, G. Csucs, H.M. Grandin, M. Textor, Surface engineering approaches to micropattern surfaces for cell-based assays., Biomaterials. 27 (2006) 3044–63. doi:10.1016/j.biomaterials.2005.12.024.

[33] S. Britland, P. Clark, P. Connolly, G. Moores, Micropatterned substratum adhesiveness: a model for morphogenetic cues controlling cell behavior., Experimental Cell Research. 198 (1992) 124–129. doi:10.1016/0014-4827(92)90157-4.

[34] H. Hermawan, D. Ramdan, J.R. Djuansjah, Metals for Biomedical Applications, Biomedical Engineering - From Theory to Applications. (2011) 411–430.

[35] F. Varíola, F. Vetrone, L. Richert, P. Jedrzejowski, J.H. Yi, S. Zalzal, S. Clair, A. Sarkissian, D.F. Perepichka, J.D. Wuest, F. Rosei, A. Nanci, Improving biocompatibility of implantable metals by nanoscale modification of surfaces: An overview of strategies, fabrication methods, and challenges, Small. 5 (2009) 996–1006. doi:10.1002/smll.200801186.

[36] A.M. Dymond, L.E. Kaechele, J.M. Jurist, P.H. Crandall, Brain tissue reaction to some chronically implanted metals., Journal of Neurosurgery. 33 (1970) 574–80. doi:10.3171/jns.1970.33.5.0574.

[37] J. Gimsa, B. Habel, U. Schreiber, U. van Rienen, U. Strauss, U. Gimsa, Choosing electrodes for deep brain stimulation experiments–electrochemical considerations, Journal of Neuroscience Methods. 142 (2005) 251–265. doi:10.1016/j.jneumeth.2004.09.001.

[38] V.S. Polikov, P. a. Tresco, W.M. Reichert, Response of brain tissue to chronically implanted neural electrodes, Journal of Neuroscience Methods. 148 (2005) 1–18. doi:10.1016/j.jneumeth.2005.08.015.

[39] R. Datti, G. Cavagnaro, S. Camici, Stainless steel wire mesh cranioplasty: ten years' experience with 183 patients (100 followed up)., Acta Neurochirurgica. 78 (1985) 133–135. http://www.ncbi.nlm.nih.gov/pubmed/4091052.

[40] and K.S. T. Bagci-Onder, A. Agarwal, D. Flusberg, S. Wanningen, P. Sorger, Real-time imaging of the dynamics of death receptors and therapeutics that overcome TRAIL

resistance in tumors, Oncogene. 32 (2013) 2818–2827. doi:10.1038/onc.2012.304.Real-time.

[41] I. Karaman, H. Sehitoglu, Y.I. Chumlyakov, H.J. Maier, The deformation of low-stacking-fault-energy austenitic steels, Jom. 54 (2002) 31–37. doi:10.1007/BF02700983.

[42] D. Canadinc, H. Sehitoglu, H.J. Maier, D. Niklasch, Y.I. Chumlyakov, Orientation evolution in Hadfield steel single crystals under combined slip and twinning, International Journal of Solids and Structures. 44 (2007) 34–50. doi:10.1016/j.ijsolstr.2006.04.011.

[43] T. Niendorf, D. Canadinc, H.J. Maier, I. Karaman, The role of grain size and distribution on the cyclic stability of titanium, Scripta Materialia. 60 (2009) 344–347. doi:10.1016/j.scriptamat.2008.10.033.

[44] S.M. Toker, D. Canadinc, a. Taube, G. Gerstein, H.J. Maier, On the role of slip–twin interactions on the impact behavior of high-manganese austenitic steels, Materials Science and Engineering: A. 593 (2014) 120–126. doi:10.1016/j.msea.2013.11.033.

[45] S. Nagarajan, M. Mohana, P. Sudhagar, V. Raman, T. Nishimura, S. Kim, Y.S. Kang, N. Rajendran, Nanocomposite Coatings on Biomedical Grade Stainless Steel for Improved Corrosion Resistance and Biocompatibility, (2012).

3. THE EFFECT OF PLASTIC DEFORMATION ON THE VIABILITY AND ADHESION BEHAVIOR OF DIFFERENT CELL TYPES IN METALLIC IMPLANT MATERIALS

The analysis on cell viability and adhesion behavior of the brain tumor cells was explained in the previous chapter. Figuring out the significant improvement in the cell response, the author wanted to find out if another cell type would present a similar result. In order to elucidate this question the fibroblast cells were seeded on the plastically deformed samples and their response was compared with the brain tumor cells.

3.1 Introduction

The use of the first metallic implants dates back to more than a century ago and they were primarily used for the repair of bone fractures [1]. Advances in the manufacturing methods and development of novel materials have paved the way for the introduction of metallic biomaterials into numerous applications, such as orthodontics, cardiovascular surgery and cranioplasty [1,2]. Stainless steel, titanium and its alloys, and cobalt-chrome alloys have widely been the material of choice in these applications [2] as they can satisfy some important mechanical, physical and chemical properties, such as high strength, fracture toughness and biocompatibility, good formability and resistance to corrosion and wear [2,3].

Among the aforementioned properties, biocompatibility of an implant has a crucial role in the overall success of the treatment since it directly influences the cell response on the implant material [2]. Specifically on a biocompatible material, cells can attach and spread through the formation of focal contacts which facilitates mechanical connections between the cell surface and extra cellular matrix (ECM) [4]. The formation of the focal contact points is mediated by the main receptor protein integrin, which regulates cell adhesion on the implant surface by the transduction of the biochemical signals through outside-in and inside-out mechanisms [5]. This bi-directional signaling controls wound healing, survival, proliferation, motility and differentiation

of the cells [5]. In addition, a good assembly of the adhesion proteins prevents chronic inflammation, or any impairment of cellular or tissue functions [6]. The overall cell response on the material surface plays a vital role for the implant treatment and needs to be improved to promote a better tissue-implant integration [2]. In order to enhance the cell response, the implant surface needs to satisfy specific conditions, such as optimized topography, roughness, wettability or high surface energy [2]. Numerous studies have been carried out to improve the cell viability and adhesion behavior on the implant surface through the modification of these properties induced by acid etching, machining, lithography or polishing [7–10]. However, these studies have merely focused on the changes of the macroscopic features on the implant surface. Thus the insufficient information about the effects of microstructural evolution on the surface properties and cell response has motivated the authors to carry out the current study.

In this study, the relation between the plastic deformation and cell response was analyzed on the austenitic 316L stainless steel samples, which were deformed by tensile loading up to 5 different strains: 5, 15, 25, 35 and 60%. Due to plastic deformation, activation of slip and twinning mechanisms in different volume fractions were observed. Two types of cell lines, namely U373 glioblastoma and BJ fibroblasts, were seeded on these samples in order to determine the responses of different cells on the material. Atomic force microscopy (AFM), confocal laser scanning microscopy (CLSM) and secondary electron microscopy (SEM) analyses showed that surface was distorted significantly with the increasing plastic strain, which led to a surface topography with denser grooves, valleys and peaks, and thus greater surface roughness. The activated slip and twinning mechanisms enhanced the adhesion and spreading behavior of the U373 cells by providing regions with greater surface energy. Specifically, U373 cells exhibited filopodial extensions on the deformed samples, which enhanced the surface adhesion of the cells. Conversely, fibroblast cells did not attach and spread as good as tumor cells, which might stem from the greater surface roughness or cell size that limited the formation of focal contacts in the larger groove size. These results show that cell behavior on the implant surface can be enhanced

by the manipulation of the microstructure and surface topography of the implant material. Furthermore, this method can be utilized to improve the biocompatibility of the material, shorten the recovery period after surgery and decrease the possible complications that patient can encounter with.

3.2 Experimental Details

The 316L stainless steel tensile test specimens used in this study were cut in thin plate shape with electro-discharge machining (EDM). The specimens were ground with 400, 800, 1200 and 2500 grit SiC papers, and polished with the diamond abrasives with the particle sizes of 6μm, 3μm and 1μm. Polishing was repeated until a shiny metallic surface free of scratches or marks was obtained. In order to observe the microstructural features on the samples they were etched with a solution containing 200 ml distilled water, 200 ml HCl (with a concentration of 32%), 20 ml HNO_3 (with a concentration of 65%) and 0.6 ml Vogel's inhibitor which was prepared at a working temperature of 70°C. These etched samples were plastically deformed with a servo-hydraulic tensile test machine up to five different strain values: 5, 15, 25 and 35%. For the cell viability measurements, a different sample geometry was utilized to attain the strain value of 60%, such that cell viability could be observed in an extreme plastic deformation. This wide range of strain values promoted the activation of the micro deformation mechanisms in different volume fractions, such that in each sample slip, twinning or their interactions were observed in different degrees. Thereby, the effect of microstructural evolution on the cell behavior was analyzed in more detail. The gauge sections of the samples subjected to the tensile test were cut by EDM to fit in the well plates. Crystallographic structure of the samples were analyzed via X-ray diffraction (XRD) with CuKα radiation, step size of 0.02^0, count time of 1 second per each step, accelerating voltage of 30kV and current of 10mA.

The surface topographies of these samples and micro deformation mechanisms were analyzed in detail via scanning electron microscopy (SEM), confocal laser scanning microscopy

(CLSM) and atomic force microscopy (AFM) in order to comprehend the alterations resulting from the plastic deformations of different levels. The stainless steel samples were analyzed by SEM both prior to and following the seeding of the cells. Prior to seeding the cells, the surfaces of the samples were analyzed with SEM at a magnification in the range of 300 – 5000 ×, under an accelerating voltage of 7 kV, current of 30 pA, and within a working distance of 6 – 7 mm. The SEM images of the cell-seeded steel samples were captured at a magnification of 300 – 4000 ×, under an accelerating voltage of 3 kV, current of 30 pA and within a working distance of 6.3 – 8 mm. Surface roughness (Ra) of each sample was evaluated with CLSM by averaging the five different regions (100μm x 100μm) on the sample surface in the magnification of 50 ×. AFM images were recorded at a tapping mode in air utilizing an antimony (n) doped silicon cantilever with a rotated tip with an 8 nm radius. The linear scanning rate was set to 1 Hz (1 line/s) and the scanning area of 20μm x 20μm.

In order to determine the cell adhesion and viability behavior on the implant surfaces, two different cell types were used in this study: BJ fibroblast and U373 glioblastoma (brain tumor) cells. These cells were obtained from the American Type Culture Collection (ATCC) and grown in standard culture conditions in DMEM supplemented with 10% FBS and 1% Penicillin-Streptomycin (Gibco). Cells were then engineered to express green fluorescent protein (GFP) using retroviral transduction [11]. Accordingly, cells were transduced with pBabeGFP viral particles in medium containing protamine sulfate (10 mg/ml) at a multiplicity of infection (MOI) of 1.

After completing the surface analyses, the steel samples were sterilized with an autoclave and each sample was placed into one well in a 24-well tissue culture plate (Costar). Then brain tumor and fibroblast cells were seeded on each well (1 × 105 cells/well) containing 1 ml growth medium and were incubated at 37°C. After 24 hours, the steel samples with the attached GFP-positive cells were analyzed with fluorescence microscopy. ATP-based cell viability assay was

used to measure the number of cells attached onto the steel surface. Accordingly, Cell Titer-Glo® (CTG) Luminescent Cell Viability Assay (Promega, USA) was modified to measure cell viability on the steel samples. A mixture containing 30 µl CTG reagent and 300 µl DMEM was added into each well. After an incubation period of 10 minutes 100 µl of cell and CTG mixture was transferred to a 96-well plate and was measured by a luminometric plate reader (Synergy H1 Reader, Biotek, USA).

3.3 Results and Discussion

The adhesion behavior and viability of the brain tumor and fibroblast cells were investigated on the 316L stainless steel samples which were subjected to the tensile loading up to 5 different strains: 5, 15, 25, 35 and 60%. Before seeding the cells steel samples were analyzed via XRD, AFM, CLSM and SEM in order to obtain information about their microstructural and surface properties. X-ray diffraction pattern in Figure 3.1 shows that crystal structure of these samples consists of austenite phase.

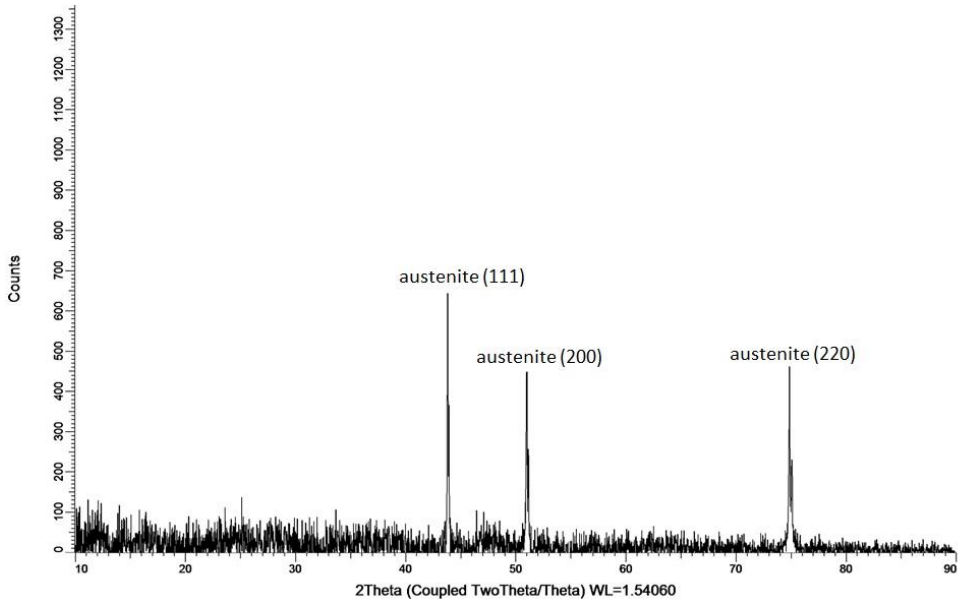

Figure 3.1. X-ray diffraction pattern of the 316L stainless steel.

SEM analyses exhibited the significant effect of the plastic deformation on the surface topography, such that the undeformed sample presents a planar surface while the surface topography of the 35% deformed sample is distorted severely concomitant with the formation of denser slip and twinning mechanisms (Figure 3.2). Surface roughness measurements of the samples via CLSM showed that average surface roughness (R_a) of the %35 deformed sample was 14 fold greater than the undeformed one, affirming the influence of plastic deformation on the surface topography.

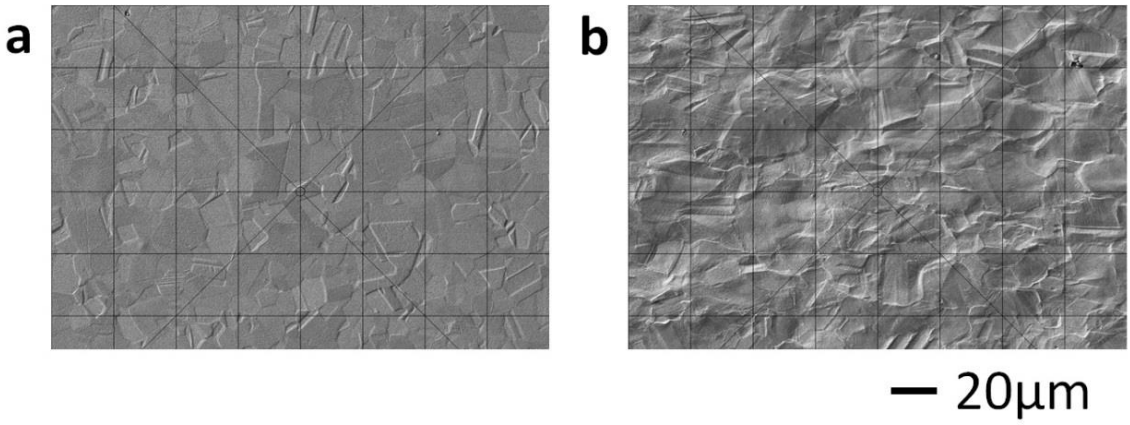

Figure 3.2. SEM images of the **(a)** undeformed and **(b)** 35% deformed 316L stainless steel samples.

The activated micro-deformation mechanisms were analyzed in more detail with AFM, SEM and CLSM in order to understand the alterations on the implant surface due to slip and twinning. The significant effect of the twinning on the sample deformed up to 35% strain was observed via AFM, and is presented in Figure 3.3. The 3D image of the surface topography and the line profile obtained from a twinned region clearly shows the distortion due to plastic deformation. Specifically, the abrupt change on the surface topography due to twinning creates a groove shape which significantly affects the surface roughness. The CLSM analysis carried out on the same sample is presented in Figure 3.4. The line profile image shows that the surface topography was significantly influenced by the activation of slip mechanism as evidenced particularly by the step-like structure.

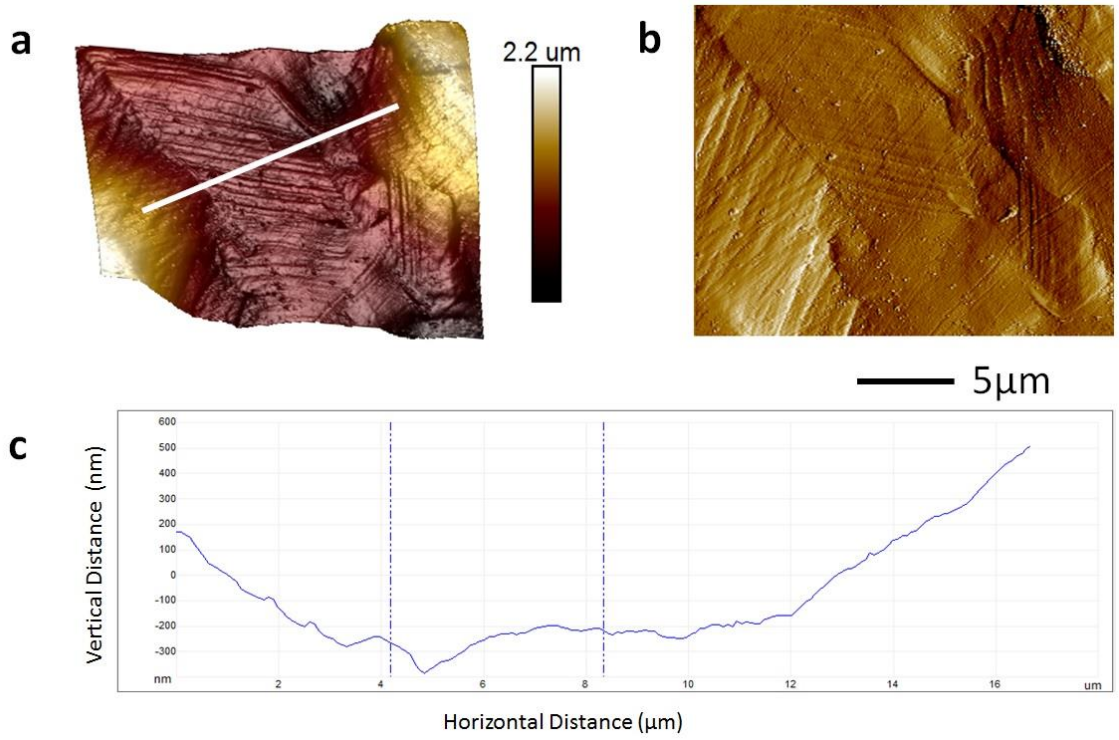

Figure 3.3. AFM images of the sample deformed up to 35% strain captured with (a) 3D image and (b) amplitude error channel. The bottom image (c) represents the line profile obtained from the twinned region.

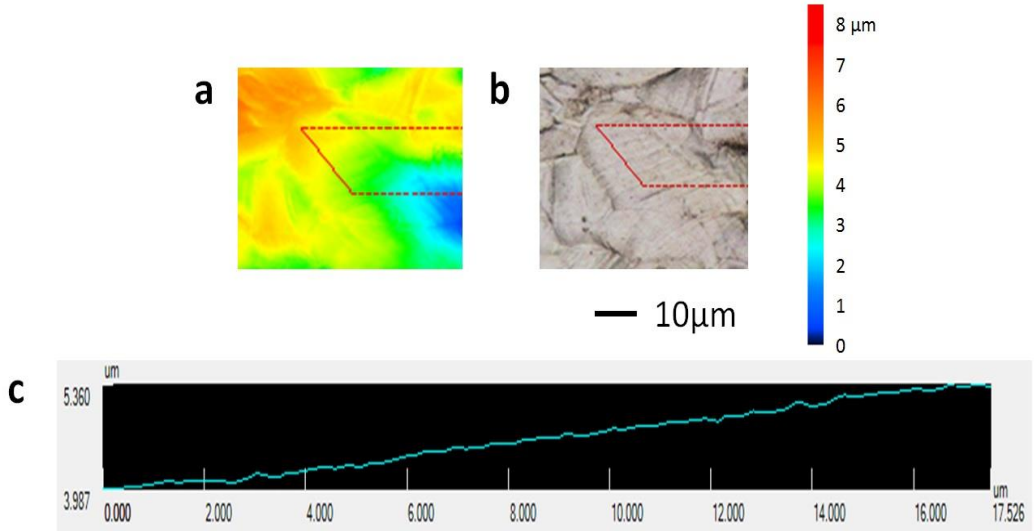

Figure 3.4. (a) Laser (b) and height images (topographic representations of the surface heights) of the slip lines within a grain in the sample deformed to 35% strain. (c) The line profile shows the step-like increase of the surface height by the slip lines within the region marked in (a) and (b). The color bar shows the surface roughness defined in terms of peak distance values along the normal to the surface (in µm).

After completing the surface characterization of the steel samples two different cells (brain tumor and fibroblast cells) were seeded on the samples to observe the response of different cells on the same implant material. Adhesion and spreading behavior of these cells were analyzed with SEM and CLSM analyses. CLSM image of the brain tumor cells in Figure 3.5 shows that these cells were able to attach and spread on the 35% deformed sample with more number of cells than on the undeformed sample. These cells also formed the intercellular attachments, which play a prominent role in the development and maintenance of tissue structure [12].

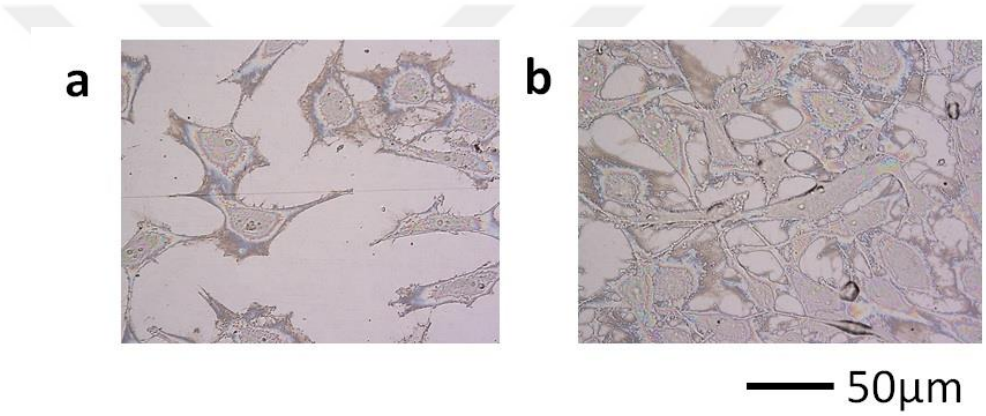

Figure 3.5. CLSM images of the brain tumor cells seeded on the (a) undeformed and (b) 35% deformed stainless steel sample.

The SEM images of the brain tumor and fibroblast cells on the steel samples deformed up to 60% (Figure 3.6) demonstrated a more spread morphology of the brain tumor cells. Specifically, the filopodial extensions encircled in red were excessively present in the tumor cells which contain integrin proteins catalyzing the formation of focal contacts, and promoting cell adhesion and migration [15]. The viability analysis of these two different types of cells showed that brain tumor cells exhibited greater cell viability on the sample deformed up to 60% as compared with the undeformed sample (Figure 3.7). The viability results of the fibroblast cells are not presented in the results because they did not exhibit a regular trend with increasing plastic deformation.

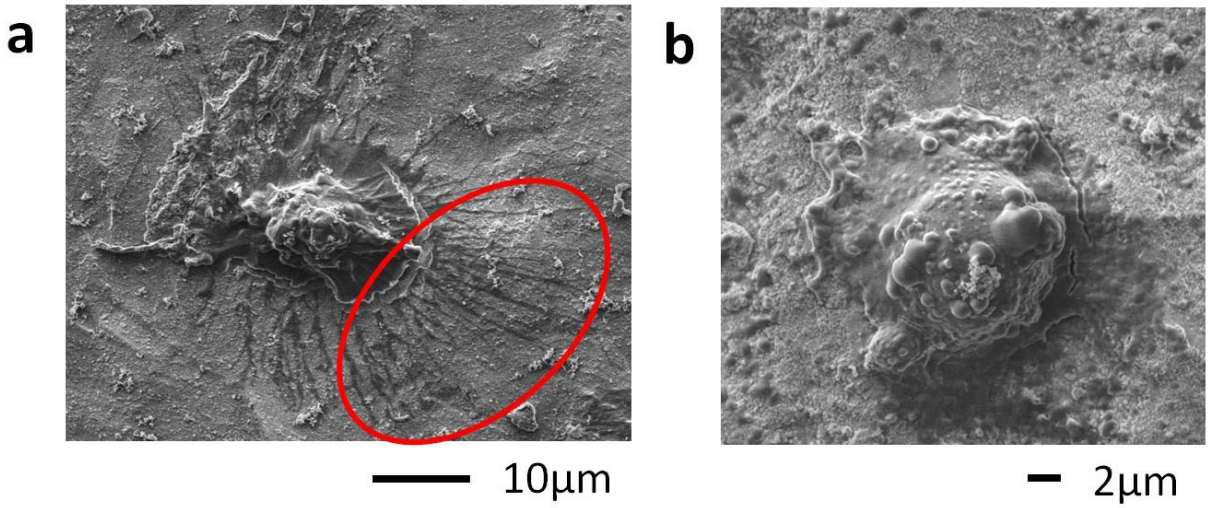

Figure 3.6. SEM images of the (a) brain tumor and (b) fibroblast cells on the stainless steel samples deformed up to 60%.

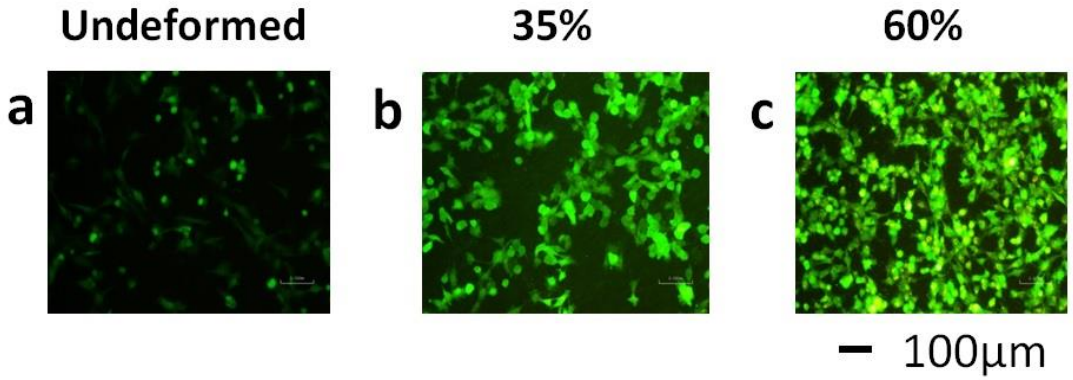

Figure 3.7. Fluorescent microscopy images of the brain tumor cells seeded on the 316L stainless steel undeformed sample (a), and those deformed up to 35% (b) and 60% (c).

The microscopy investigations of the implant surface in parallel with the cell response showed that the plastic deformation induced micro-deformation mechanisms improved the cell viability, attachment and spreading of the brain tumor cells, particularly by distorting the surface topography and enhancing the surface roughness. Specifically, valleys and peaks with the great surface energy catalyzed the formation of focal contacts by accumulating the ECM molecules

within these grooves [14]. By the formation of focal contacts cells were able to attach on the metal surface and motility was initiated through the interaction with the actin cytoskeleton [13] which constitutes importance for the wound healing, proliferation and migration [15]. In addition, twinning and slip mechanisms played significant role on the cell response owing to their great surface energy, which eased the accumulation of ECM molecules, as well promoting the formation of the focal contacts [2,16,17].

It should also be noted that the response of the fibroblast cells did not exhibit a significant change with the increasing plastic strain. The difference in cell viability, adhesion and spreading behavior of these two cell types can be associated with the size of the fibroblast, which might have failed to form focal contacts due to larger groove sizes or greater surface roughness [18]. In addition, the ECM molecules expressed by the fibroblast cells may have not formed a good attachment on the deformed samples due to weak adhesion strength between the substrate and the cells owing to the physical and chemical properties of the implant material [19]. This result shows that, in order to achieve a successful implant treatment, microstructural properties and surface topography of the implant materials need to be tailored to provide the optimum cell response in the specific body location where the implant is placed. It should also be noted that the unique composition and topology of ECM in each different tissue [20,21] necessitates the manufacturing of tissue-specific implants by also considering the physical, chemical and mechanical properties of the material, instead of implanting the same material in different body locations. Thus, the manufacturing of implants by the selection of the most suitable material for the cell type that the metal will interact with throughout the treatment will improve the tissue-implant integration. Thereby, the implantation would cause less impairment of cellular functions and postsurgical complications, which would overall enhance the life quality of the patient and the success of the treatment.

3.4 Conclusions

Adhesion, attachment and spreading behavior of the brain tumor and fibroblast cells were investigated on the 316L stainless steel samples deformed up to different strains which triggered the activation of micro-deformation mechanisms in varying degrees. Surface characterization and microscopy analyses showed that surface topographies of the samples were heavily influenced by the micro-deformation mechanisms, which specifically increased the average surface roughness and distorted the surface topography. Higher surface energy of the twinning and slip mechanisms promoted the adhesion of ECM molecules on the implant surface and formation of focal contacts. Specifically, tumor cells exhibited a greater viability and adhesion behavior on the sample with greatest plastic deformation. Filopodial extensions formed by these cells showed the higher affinity of the tumor cells on the deformed samples. Conversely, fibroblast cells did not exhibit enhanced cell response on the deformed samples, which might stem from the size of these cells or the failure of the adhesion of ECM molecules secreted by the fibroblast cells. These results show that surface and microstructural properties can be manipulated through the activation of micro deformation mechanisms and the ideal implant material specific for a body location can be manufactured. Thereby, enhanced cell adhesion and viability can be achieved which would lead to a more successful treatment.

3.5 References

[1] Q. Chen, G. Thouas, Metallic implant biomaterials, Materials Science and Engineering: R: Reports. 87 (2015) 1–57. doi:10.1016/j.mser.2014.10.001.

[2] B. Uzer, S.M. Toker, A. Cingoz, T. Bagci-Onder, G. Gerstein, H. Maier, D. Canadinc, An exploration of plastic deformation dependence of cell viability and adhesion in metallic implant materials, Journal of the Mechanical Behavior of Biomedical Materials. 60 (2016) 177–186. doi:10.1016/j.jmbbm.2016.01.001.

[3] I. Gotman, Characteristics of Metals Used in Implants, Journal of Endourology. 11 (1997)

383–389.

[4] B. Größner-Schreiber, M. Herzog, J. Hedderich, A. Dück, M. Hannig, M. Griepentrog, Focal adhesion contact formation by fibroblasts cultured on surface-modified dental implants: An in vitro study, Clinical Oral Implants Research. 17 (2006) 736–745. doi:10.1111/j.1600-0501.2006.01277.x.

[5] C.K. Miranti, J.S. Brugge, Sensing the environment: a historical perspective on integrin signal transduction., Nature Cell Biology. 4 (2002) E83–E90. doi:10.1038/ncb0402-e83.

[6] S. Bauer, P. Schmuki, K. von der Mark, J. Park, Engineering biocompatible implant surfaces, Progress in Materials Science. 58 (2013) 261–326. doi:10.1016/j.pmatsci.2012.09.001.

[7] S. Britland, P. Clark, P. Connolly, G. Moores, Micropatterned substratum adhesiveness: a model for morphogenetic cues controlling cell behavior., Experimental Cell Research. 198 (1992) 124–129. doi:10.1016/0014-4827(92)90157-4.

[8] R. Flemming, C. Murphy, G. Abrams, S. Goodman, P. Nealey, Effects of synthetic micro- and nano-structured surfaces on cell behavior, Biomaterials. 20 (1999) 573–588.

[9] L. Le Guéhennec, A. Soueidan, P. Layrolle, Y. Amouriq, Surface treatments of titanium dental implants for rapid osseointegration, Dental Materials. 23 (2007) 844–854. doi:10.1016/j.dental.2006.06.025.

[10] M.H. Kim, K. Park, K.H. Choi, S.H. Kim, S.E. Kim, C.M. Jeong, J.B. Huh, Cell adhesion and in vivo osseointegration of sandblasted/acid etched/anodized dental implants, International Journal of Molecular Sciences. 16 (2015) 10324–10336. doi:10.3390/ijms160510324.

[11] T. Bagci-Onder, A. Agarwal, D. Flusberg, S. Wanningen, P. Sorger, Real-time imaging of the dynamics of death receptors and therapeutics that overcome TRAIL resistance in tumors, Oncogene. 32 (2013) 2818–2827. doi:10.1038/onc.2012.304.Real-time.

[12] A.P. Kowalczyk, E.A. Bornslaeger, S.M. Norvell, H.L. Palka, K.J. Green, Desmosomes:

intercellular adhesive junctions specialized for attachment of intermediate filaments, Int Rev Cytol. 185 (1999) 237–302. doi:10.1016/S0074-7696(08)60153-9.

[13] P.K. Mattila, P. Lappalainen, Filopodia: molecular architecture and cellular functions, Nature Reviews Molecular Cell Biology. 9 (2008) 446–454. doi:10.1038/nrm2406.

[14] D.D. Deligianni, N. Katsala, S. Ladas, D. Sotiropoulou, J. Amedee, Y.F. Missirlis, Effect of surface roughness of the titanium alloy Ti6Al4V on human bone marrow cell response and on protein adsorption, Biomaterials. 22 (2001) 1241–1251.

[15] M.A. Wozniak, K. Modzelewska, L. Kwong, P.J. Keely, Focal adhesion regulation of cell behavior, 1692 (2004) 103–119. doi:10.1016/j.bbamcr.2004.04.007.

[16] S.M. Toker, D. Canadinc, H.J. Maier, O. Birer, Evaluation of passive oxide layer formation-biocompatibility relationship in NiTi shape memory alloys: Geometry and body location dependency., Materials Science & Engineering C, Materials for Biological Applications. 36 (2014) 118–29. doi:10.1016/j.msec.2013.11.040.

[17] B. Uzer, B. Gumus, S.M. Toker, D. Sahbazoglu, D. Saher, C. Yildirim, S. Polat-Altintas, D. Canadinc, A Critical Approach to the Biocompatibility Testing of Niti Orthodontic Archwires, International Journal of Metallurgy and Metal Physics. 1 (2016) 1–7.

[18] R.G. Richards, The effect of surface roughness on fibroblast adhesion in vitro, Injury. 27 (1996) 38–43. doi:10.1016/0020-1383(96)89031-0.

[19] N.J. Hallab, K.J. Bundy, R.L. Moses, J.J. Jacobs, Evaluation of Metallic and Polymeric Biomaterial Surface Energy and Surface Roughness Characteristics for Directed Cell Adhesion, 7 (2001) 55–71.

[20] C. Frantz, K.M. Stewart, V.M. Weaver, The extracellular matrix at a glance., Journal of Cell Science. 123 (2010) 4195–4200. doi:10.1242/jcs.023820.

[21] B.P. Chan, K.W. Leong, Scaffolding in tissue engineering: General approaches and tissue-specific considerations, European Spine Journal. 17 (2008). doi:10.1007/s00586-008-074

4. INVESTIGATION OF THE DISSOLUTION – REFORMATION CYCLE OF THE PASSIVE OXIDE LAYER ON NITI ORTHODONTIC ARCHWIRES

Having thoroughly understanding the relationship between the viability and adhesion response of different cells and the microstructure of the implants, the author wanted to better understand the parameters affecting the biocompatibility of the implants. Protective oxide layer covering the material surface was shown to play a critical role in the literature since its presence directly influences toxic Ni ion release. Researches showed that due to the corrosive environment of the intra oral environment oxide layer goes through a dissolution-reformation cycle which motivated the author of this thesis to carry out the experiment to be explained in this chapter.

4.1 Introduction

The Nickel-Titanium (NiTi) shape memory alloys (SMAs) have been employed in biomedical applications at an increasing rate within the last decades owing to their superior thermo-mechanical properties [1–10]. Specifically, the NiTi alloys can assume two distinctly different shapes by means of solid-to-solid phase transformation between austenitic and martensitic phases upon temperature change or loading [2,5,8–11], opening the venue for their utility in various dental, cardiovascular and orthopedic applications [2,7].

One of the well-known applications is the orthodontic archwire, which benefits from the pseudoelastic property of NiTi [2,5,7,9]: austenite-to-martensite phase transformation upon loading allows for attaining a state of constant stress for a relatively wide strain range [2,7,9,11], which eliminates the need for frequent readjustments of the orthodontic arch wire to keep the stress at an optimum level for simultaneous tooth movement and periodontal tissue regeneration despite the changing strain on the wires [9]. Shape memory gloves which are used for the physiotherapy of partially atrophied muscles benefit from another important property, namely the two-way shape memory effect, such that the natural motion of a hand is mimicked with the wires placed in the regions over the fingers which contract and stretch by heating and cooling [5,12].

Consequently by the assistance of this glove the activity of the injured hand is maintained and the original hand motion would be promoted [12].

Even though the NiTi alloy has been employed as a material of choice in various biomedical applications, biocompatibility related issues have constituted a significant concern and continue to come under focus in various studies [1–10,13]. In particular, when NiTi alloys are implanted in the body they are attacked by the aggressive ions of the body fluids, such as chlorides, hydrocarbonates or sulfates [14]. For instance, the high concentration of chloride ions in the saliva can cause pitting corrosion on the surface, which would further damage the material though the bulk and enhance the release of Ni ions in greater amounts [14–16]. As a result of corrosion assisted ion release the biocompatibility of the alloy, and thus, the success of the treatment could be significantly altered. In addition, stress corrosion cracking (SCC) constitutes another complication for the orthodontic treatments, such that when the archwires are loaded or archwire-bracket contact sites develop excessive stress along with the corrosivity of the saliva, the cracking of the archwires, and thereby the release of toxic Ni ions are enhanced [17,18]. When the amount of Ni ion release reaches a critical value of 0.12-0.5 mg/L, serious toxic, carcinogenic and allergic effects may prevail, necessitating additional treatment [2,8].

Recently, evidence has been forwarded demonstrating that the Ni ion release is dictated by several parameters, including the body location where the NiTi implant comes into contact with tissue, surface morphology of the implant material, and the passive oxide layer on the alloy surface [8,9]. Among these parameters, the passive oxide layer plays a critical role since it influences the Ni ion release, which in turn affects the biocompatibility of the implant [2,6]. Thermodynamically, formation of titanium oxide is favored over that of nickel oxide since titanium oxidizes more easily, and particularly forms titanium dioxide, which is stoichiometrically the most favorable oxide on the alloy surface [8,9]. Indeed, the surface of NiTi implants is usually covered with a protective oxide layer during the manufacturing process to prevent ion release [2].

However, this protective layer does not constitute a thorough prevention against ion release since it can possess cracks or defects which can be acquired during manufacturing or service [2,4].

Surface roughness of the archwires has also been reported to be an important parameter since it affects the biocompatibility of the material, friction between the archwire and the brackets, and the efficient sliding mechanism, all of which dictate the success of the orthodontic treatment [17,19,20]. For instance, the archwire-bracket contact sites possessing greater surface roughness than the remaining parts of the archwire, which are not in direct contact with the brackets, significantly increase the friction force and hinder an efficient arch-guided tooth movement [17,19]. In this case, application of greater forces on the wires becomes necessary for the remainder of the treatment, yet this can result in the undesirable SCC leading to significant Ni ion release [17].

Growth of the passive oxide layer during service, and its correlation with Ni ion release rate and the biocompatibility of NiTi implants have been addressed in various immersion studies [2,8,10]. An excess amount of Ni release was reported on the second day of an immersion experiment as opposed to significantly smaller amounts in the later stages of the experiment [8]. Particularly, an oxide layer forms on the outer layer mostly with Ti depleted Ni, and the initially dissolved Ni ions start to form compounds with the Ti ions beneath the oxide layer during the later stages of the immersion, which results in the decrease of the Ni ion concentration in the culture media [8].

The passive oxide layer does not grow monotonously in an immersion experiment. Depending on the pH of the environment, a dissolution-reformation cycle may take place, dictating the instantaneous thickness of the oxide layer, Ni release rate and the biocompatibility of the implant material [2,21]. When the oxide layer dissolves faster than it reforms, the rate of ion release increases owing to the weaker protection provided by the thinner oxide layer [2]. On the other hand, a reformation faster than the dissolution yields a thicker oxide layer and a nickel rich oxide-metal interface [4,13]. A thicker oxide layer exhibits a more brittle behavior as

compared to a thin oxide layer, and thus, promotes formation of defects or cracks, both of which can eventually result in more severe Ni ion release [4,13]. Therefore, the oxide layer on the implant material needs to meet important criteria, such as minimum toxic Ni ion release and lowest corrosion rate to achieve a successful treatment. Consequently, the dissolution-reformation cycle constitutes one of the major parameters influencing the biocompatibility of the implant, and lack of knowledge about this cyclic alteration warrants further investigation.

The dissolution-reformation cycle of orthodontic applications depends strongly on the pH of the saliva [18,22,23]. Saliva with acidic pH values (pH<7) is more corrosive and can attack on the archwire surface resulting in Ni ion release from the archwire into the intra oral cavity. Natural saliva exhibits varying pH values depending on the changing saliva flow rate, which is affected by age, genetic heritage, dietary habits, exercise and medication [24–27]. While the normal pH values are between 6.2-7.4, values as low as 2.0-2.5 are also possible [26–28]. The current study was undertaken with the motivation of understanding the dissolution-reformation cycle of the oxide layer on NiTi archwires in detail, and establishing its relationship with the Ni ion release from the alloy. For this purpose, static immersion experiments were carried out, where NiTi orthodontic archwires were immersed in artificial saliva (AS) solutions with different pH values simulating various possible intra oral environments. Dissolution-reformation cycle of the oxide layer was investigated on the archwires immersed in AS solution with a 2.3 pH value for 1, 7, 14 and 30 days since this particular AS solution represents the most corrosive intra oral environment. The current findings demonstrate that the protective titanium oxide layer on the NiTi archwires immersed in the AS with a pH of 2.3 undergo a dissolution-resolution cycle that complies well with the ion release into the solution within the first 14 days of the immersion period. Furthermore, the current results also point at the necessity of eliminating any alterations to the surface roughness and topography of the archwires during manufacturing in order to ensure the biocompatibility of archwires and provide an efficient treatment for the patients.

4.2 Experimental Details

Dissolution-reformation cycle of the passive oxide layer on the NiTi samples was investigated by utilizing static immersion experiments. The NiTi specimens used in this study were orthodontic archwires[1] having a chemical composition of 54.5-57 wt. % Ni [29] and an austenite finish temperature within the range of 20 - 40 ° C (as specified by the manufacturer). Prior to the immersion, they were cleaned in an ultrasound bath with ethanol in order to remove dirt, dust or metallic powder that may have been left on the surface. The native oxide layer on the NiTi sample surfaces was not removed since the implants employed in human body also possess this protective layer. For the immersion experiments, intraoral environment was simulated by artificial saliva (AS) which was prepared with the chemicals listed in Table 4.1.

Table 4.1. Chemical content of the artificial saliva used in immersion experiments.

Ingredients	*Amount of Ingredients (g/l)*
NaCl	0.4
KCl	0.4
$CaCl_2 \bullet 2H_2O$	0.906
$NaH_2PO_4 \bullet 2H_2O$	0.690
$Na_2S \bullet 9H_2O$	0.005
Urea	1

These chemicals were mixed in a beaker with deionized water and the solution was heated up to and kept constant at body temperature (37°C) by a hot plate stirrer. These solutions were prepared with three different pH values, namely 2.3, 3.3 and 4.3, with the intention of better understanding of the corrosive effect of the different acidic pH values on the NiTi archwires.

[1] 3M Unitek Nitinol heat-activated archwires with 0.36 mm diameter were used in the experiments.

The acidity of the solutions was adjusted by adding 1M HCl slowly. Dissolution-reformation cycle was investigated on the orthodontic archwires immersed in the solution with the pH value of 2.3 for 1, 7, 14 and 30 days of immersion periods which will be referred to as D1, D7, D14 and D30 throughout the text, respectively. A different set of experiments was carried out by the immersion of NiTi archwires in the AS solutions with the pH values of 2.3, 3.3 and 4.3 for 30 days long in order to evaluate the overall oxide layer thickness dependence on the acidity of the intraoral environment. Each archwire sample was immersed in a certain amount of AS solution which meets a predefined solution volume per surface area ratio of 20mL/cm^2 [30]. Throughout the immersion experiments, samples were kept in separate sealed tubes and placed into an electronically controlled water bath which sustained the body temperature.

The surface topography of each sample was monitored with field emission scanning electron microscopy (FESEM, Ultra Plus, Zeiss, Germany) both prior to and following immersion experiments. The samples were investigated with 5 kV of primary electron energy to avoid charging and surface damage. The samples were not coated with a thin conducting layer. The images were taken with two different detectors simultaneously and displayed on split screen mode, such that one part of the image was recorded by the in-lens detector which detects primarily SE1 type secondary electrons, enhancing the material contrast. The other part of the image was recorded by the Everhart-Thornley secondary electron detector, which detects SE1+SE2+SE3 type secondary electrons and is sensitive to surface morphology.

The surface chemical composition and depth profiles of samples were analyzed by X-ray photoelectron spectroscopy (Thermo Scientific K-alpha XPS). In order to achieve a statistical consistency, XPS results were collected from 3 different points on each sample. The XPS system had a monochromatic aluminum target micro-focus X-ray source (1486.7 eV). The samples were taped to the edge of the sample holder so that 10 mm segments were suspended freely in air. The analyses were carried out with a 300 micrometer X-ray spot size on the suspended regions of the

wires to avoid superfluous substrate signals. The spectra were recorded in the so called "snap shot" mode where the pass energy was 150 eV and the 128-pixel detector saw the corresponding energy spread of electrons. The spectra were later energy deconvoluted with the point spread function to reach an effective energy resolution equivalent of 50 eV pass energy, i.e. 0.5 eV. A flood gun was used for charge compensation. The base pressure of $1x10^{-9}$ mbar rose to $1x10^{-7}$ mbar under operation. The depth profiling was carried out with 2 keVAr^{+} beam. The spectra were referenced for the C 1s signal at 285.0 eV and quantified with Avantage v5 software by Thermo Fischer Scientific. The carbon and oxygen regions were fitted with 40/60 Gaussian/Lorentzian peaks. The high resolution titanium spectra, on the other hand, was analyzed with principal component analysis (PCA) due to the complex nature of oxide/interface/bulk metal regions and the multitude of sub-stoichiometric species. The nickel 2p signal (Ni^{0}) was integrated and quantified using the Scofield factor. An estimated 0.14 nm/s etch rate was used to convert etch time to depth values.

Released Ni and Ti ions from the archwires into immersion fluids were detected with ICP-MS equipped with octopole reaction system helium collision cell for spectral interference removal, rather than ICP-OES, considering the μg/L (ppb) level ion detection capability of the former. The ICP-MS was operated with MicroMist glass concentric nebulizer, quartz Scott-type spray chamber and Ni sampler/skimmer cones. Daily instrumental optimizations were performed using 1 μg/L tuning solution for the short-term stability of the instrument. The corresponding instrument settings and parameters are provided in Table 4.2.

Table 4.2. ICP-MS operating parameters.

Number of points per peak	3	**Plasma gas flow (Argon)**	15L/min
Replicates	5	**Helium gas flow (Collision cell)**	4.3ml/min
Sweeps/replicate	100	**Carrier gas flow (Argon)**	1L/min
Integration time per mass	0.12s	**Plasma Forward Power**	1550W

Surface roughness of each archwire sample was evaluated by atomic force microscopy (AFM). Considering the irregularities on the archwire surface due to manufacturing processes AFM images were obtained from the uniform regions which were detected by scanning the archwires' surfaces thoroughly. This technique eliminated the deviations between each measurement and provided more reliable surface roughness results. The AFM images were captured in the tapping mode in air utilizing an antimony (n) doped silicon cantilever with a rotated tip of a radius 8 nm and resonance frequency of 75 kHz. The linear scanning rate was set as 1 Hz (1 line/s) and image size was 30 × 30 μm^2. The measurements were repeated at least 5 times for the sake of reliability and statistical consistency, and the surface roughness (R_a) values were determined based on their average.

4.3 Results and Discussion

Biocompatible NiTi orthodontic archwires were subjected to static immersion experiments for different durations in AS solutions featuring different pH values, and the ICP-MS, AFM, SEM and XPS analyses demonstrated prominent differences between the samples immersed in different solutions. For instance, Ni and Ti ion releases from the archwires into the AS solutions with 2.3 pH were significantly more as compared to Ni and Ti ions released into other solutions (Figure 4.1). When the pH of the solution increased from 2.3 to 3.3 the Ni and Ti ion release decreased about 16 fold. However, further increase of the AS solution pH to 4.3 led to only a very slight decrease in ion release (Figure 4.1). The prominent change in the ion release behavior when the pH values increased from 2.3 to 3.3 shows that the AS solution's pH in this range influences ion release behavior drastically and makes the archwires more prone to corrosion.

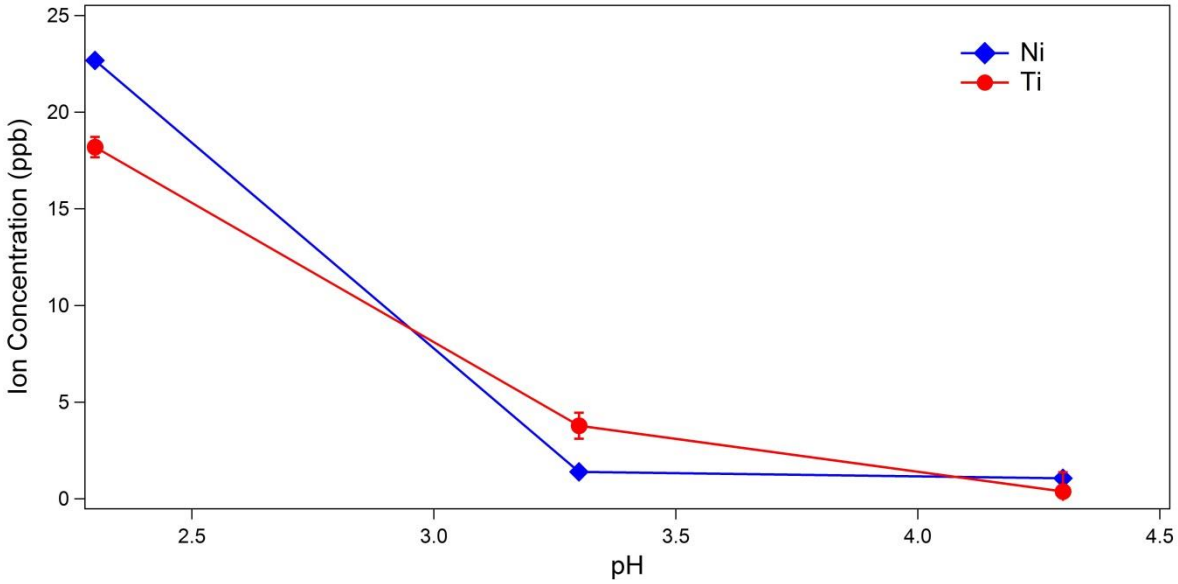

Figure 4.1. The concentration of released Ni and Ti ions in the AS solution with the pH values of 2.3, 3.3 and 4.3. It should be noted that error bars are present for each data point, however; they are not easily identified on the graph for measurements with very small error.

The significant effect of the solution pH on the ion release was previously analyzed in scientific studies, and the adverse effect of the acidic pH on biocompatibility was pointed out [23,31,32]. In particular, analyses of archwires immersed in solutions with a wide range of pH values showed that the amount of metal ion release was almost undetectable in the solutions with pH ≥ 3.75, which implies that significant ion release takes place especially in the solutions with the pH < 3.75 [31]. In the current study, the most significant decrease of the ion release was observed in the solutions with the pH < 3.3, however; detectable ion release was prominent when pH ≥ 3.3, as well (Figure 4.1). The current results demonstrate that the orthodontic archwires are significantly affected by the solution pH and metal ions release is the greatest in the most acidic environment. However, it should also be noted that Ni ion released into all of the utilized solutions stayed far below the critical Ni level (0.12-0.5 ppm) that may cause allergic reactions [17]. The released Ti ions detected by ICP-MS, on the other hand, do not pose any threat because they are not cytotoxic as Ni ions, however; the Ti ion presence in the solution implies the dissolution of the protective Ti oxide layer, which could eventually lead to enhanced

Ni ion release [31]. This argument can be supported by the SEM analysis of the tested samples: the SEM images of these archwires which were immersed in the AS solutions with pH values of 2.3, 3.3 and 4.3 for 30 days are presented in Figure 4.2. The surfaces of the archwires immersed in 3.3 and 4.3 pH solutions look rather smooth when compared with the that of the one immersed in 2.3 pH AS, which stems from the more aggressive environment imposed by the lower pH. Specifically, non-uniform dissolution of the protective oxide layer due to the greater acidity of the solution leads to a lower corrosion resistance [3], which, in turn, enhances Ti ion release (Figure 4.2), deteriorates the surface and alters the topography (Figure 4.2(a)).

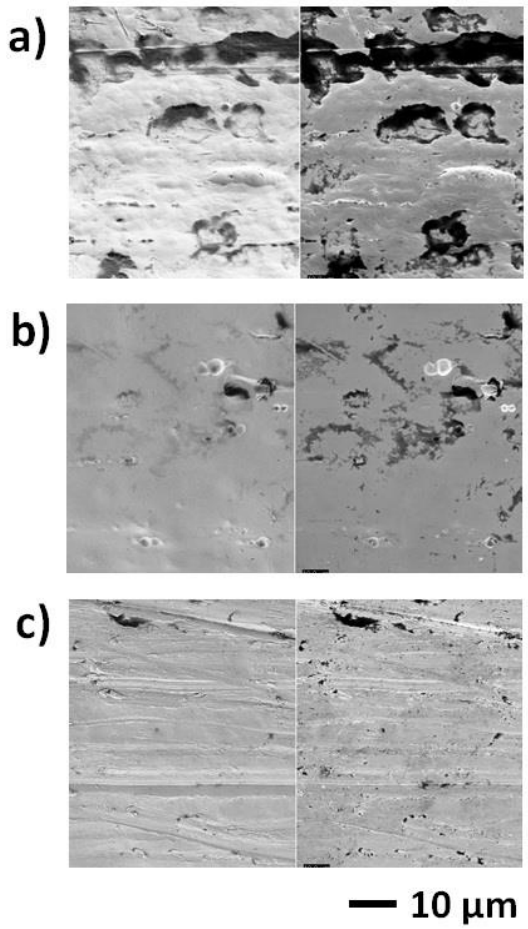

Figure 4.2. SEM images obtained by inlens (the left frame) and SE detectors (the right frame) of the NiTi archwire surfaces immersed for 30 days in the AS with a pH value of **(a)** 2.3, **(b)** 3.3, and **(c)** 4.3.

In order to understand the effect of dissolution-reformation cycle of the titanium oxide layer on the ion release behavior, a different set of experiments were performed for four different time periods (1, 7, 14 and 30 days - referred to as D1, D7, D14 and D30, respectively) in the AS solution with a pH of 2.3. The cumulative amounts of Ni and Ti ions released from the archwires into this solution were also measured and presented in Figure 4.3.

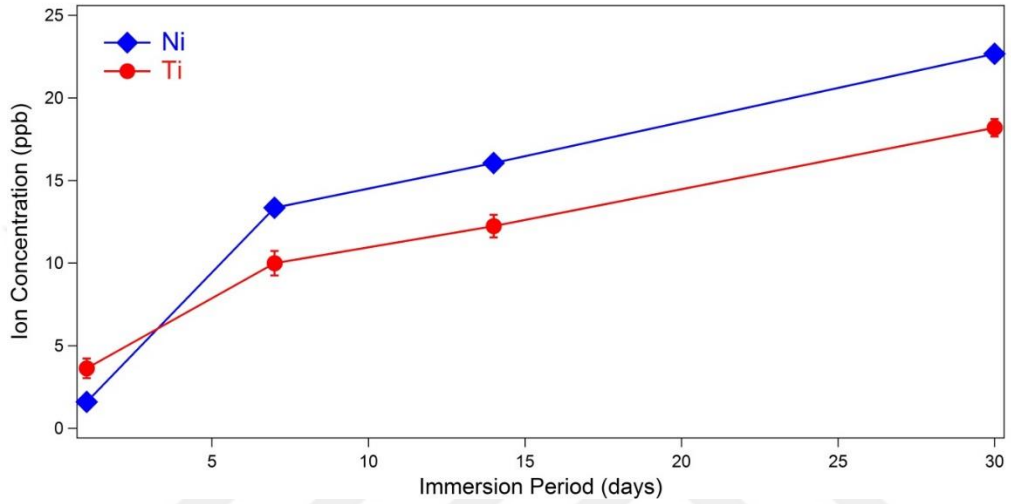

Figure 4.3. The concentration of released Ni and Ti ions in the AS solution with the pH value of 2.3 for 1, 7, 14 and 30 days. It should be noted that error bars are present for each data point, however; they are not easily identified on the graph for measurements with very small error.

In order to analyze the net ion release within each immersion interval the ion release concentration of the previous time period was subtracted from the following one. . For instance, in order to find out the net ion release within the immersion interval of D7–D14, the total ion release concentration of D7 was subtracted from the total value of D14. These net ion release values are plotted in Fig. 4.4, which are also presented in Table 4.3 in a normalized fashion (by the number of days within each interval) for the sake of obtaining the ion release rate within each immersion interval. This table reveals an interesting result, such that the ion release rate of Ti ion from D0 to D1 shows a greater value than the Ni ion release rate, which might stem from the initial dissolution of protective oxide layer. The Ti ion release rate drops between D1 and D7, while that of the Ni ion increases slightly possibly due to weaker

protection against corrosion. For both Ti and Ni, the release rate drops significantly after D7. Following D14, the ion release rate was lower compared to the release rate of immersion for the interval of D0–D7. These results show that the orthodontic archwires were more prone to corrosion during the immersion period of D0–D7, and thus the major ion release occurred within the first 7 days of immersion, which agrees well with the literature [32].

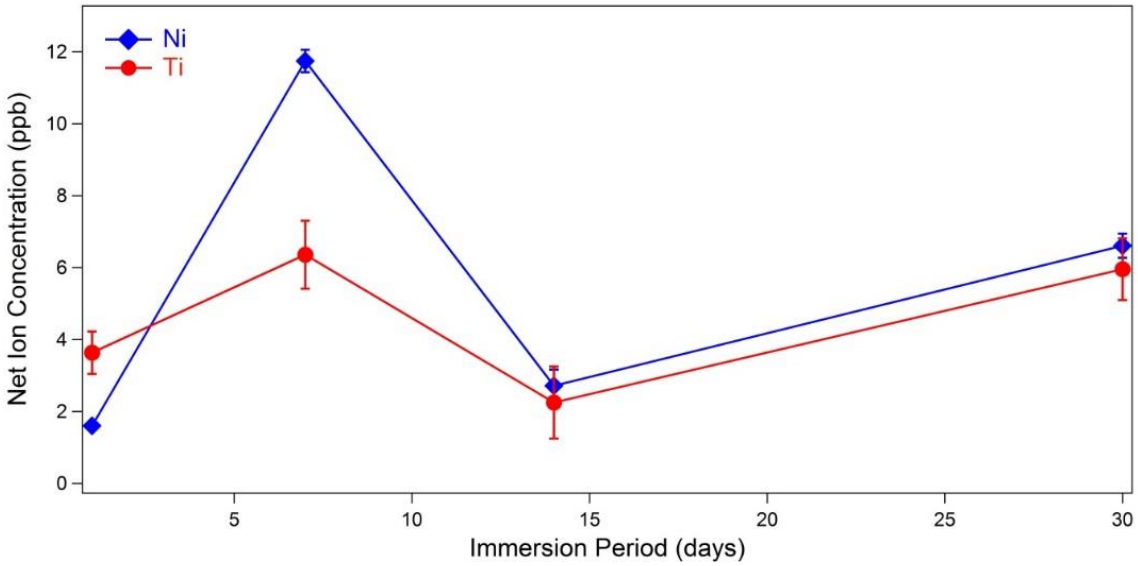

Figure 4.4. The concentration of net Ni and Ti ions in the AS solution with the pH value of 2.3 for 1, 7, 14 and 30 days. It should be noted that error bars are present for each data point, however; they are not easily identified on the graph for measurements with very small error.

Table 4.3. The net ion release within each immersion interval and release rate of Ni and Ti which was obtained by normalizing the net ion release within each immersion interval by the number of the days in each interval.

	Ni		Ti	
Time Interval (days)	**Net Ion Release (ppb)**	**Release Rate (ppb/day)**	**Net Ion Release (ppb)**	**Release Rate (ppb/day)**
0-1	1.601	1.601	3.634	3.634
1-7	11.746	1.958	6.359	1.06
7-14	2.715	0.388	2.251	0.322
14-30	6.61	0.413	5.96	0.372

In order to comprehend the oxide layer dissolution-reformation cycle, XPS analysis was carried out on the as-is, D1, D7, D14 and D30 samples (D30 immersed in pH 2.3, 3.3 and 4.3), and the corresponding depth profile data is presented in Figure 4.5. The Ti region XPS spectra were processed using principal component analysis to identify the oxide, intermediate sub-oxide and the metallic moieties. The quantification of these moieties was performed with the Scofield factors and plotted as atomic percentages as a function of etching time. The x-axis of this plot can be converted to a depth axis, however a reliable etch rate is difficult to assign to different species. Nevertheless, an estimated etch rate of 0.14 nm/s can be assigned for Ta_2O_5 etching under these conditions. The plot shows the relative amounts of the oxide, intermediate and metallic titanium species on the surface of the species. The ion energy of 500 V was specifically chosen not to reduce the titanium +4 species during bombardment and not to yield superfluous signal. One can use the following plot to compare the oxide thicknesses of the samples using either the maximum amount of the intermediate species or the rising edge of the metallic titanium species. We have chosen the initial signal obtained from the metallic titanium which was achieved by the bombardment of the archwire surface with the argon ions and removal of the oxide layer covering the archwire surface. In order to speculate about the oxide layer thicknesses of the archwires the etch time (depth axis) corresponding to the time of the first metallic Ti signal acquisition was multiplied by the etch rate (0.14 nm/s). The oxide layer thickness of the days 1, 7, 14 and 30 was approximately evaluated as 5.64, 1.64, 4.36 and 7.1 nm. The depth profile data of the as-is archwire showed a significantly thinner oxide layer than all of the immersed archwires. But the sample immersed in AS even for 1 day exhibited a thicker oxide layer than the as-is one. This result can affirm that the oxide layer formation due to AS solution-archwire interaction started right after the immersion [8]. After D1, oxide layer dissolution was observed on the sample immersed in AS for 7 days. After D7, it started reforming again until D14, and thereafter it kept increasing until D30 in a more stable manner. It is noteworthy that the oxide layer dissolution-reformation cycle follows a trend in the first 14 days of immersion. Accordingly, there

might be a decrease in the oxide layer thickness during D14-D21, followed by an increase during D21-D30. Since D21 was not included in the current experiments, this aspect was left for future work

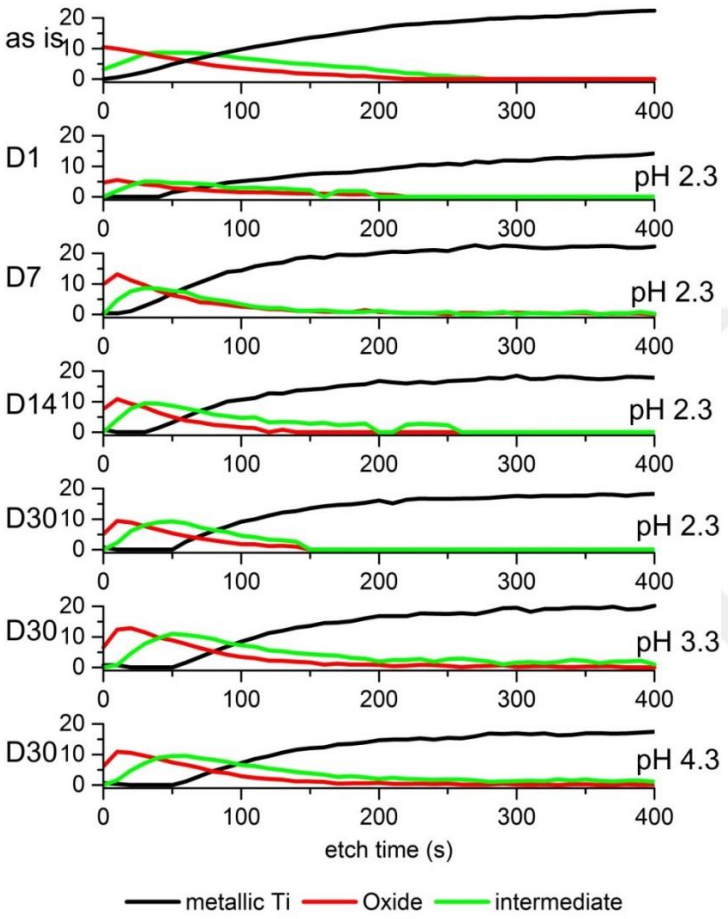

Figure 4.5. Depth profile data obtained by XPS.

The XPS spectra recorded during the depth profiling of the sample immersed in AS with the pH of 2.3 for 30 days is presented in Figure 4.6. The y-scales of the spectra are kept the same for each element in 3 panels for direct comparison. The labels on the left indicate the extent of argon ion bombardment with t=0 corresponds to the pristine sample surface. The top surface was dominated by Ti oxide with the Ti $2p_{3/2}$ signal located at 458.5 eV for the Ti^{4+} species. The O1s region was deconvoluted to 3 peaks, which corresponds to the metal oxide (TiO_2, 530 eV),

sub-oxide ($TiO_{x<2}$, 531.5 eV) and surface adsorbed water (533 eV). The nickel $2p_{3/2}$ region had a very weak signal for the metallic nickel indicating the inertness of Ni and the thickness of the Ti oxide on the surface. As the surface etching proceeded (t=50 s), the carbon signal started to decrease, and signals from the oxide layer increased accordingly. The Ti region shows the sub-oxide peaks, as well as weak metallic moiety, while the oxygen region peaks show slight enhancement due to the removal of the carbon contamination. The Ni signal increased without a change in binding energy, i.e. still in metallic phase. Towards the end of the etching study (t=400 s), the carbon species still persisted as a weak signal, which indicates that the carbon was actually embedded into material during production, surface treatment or due to carbon deposition throughout the immersion period in AS solution, which contained urea. The metallic Ni and metallic Ti signals dominated the spectra, while some oxygen species still remained. A possible reason for tenacious oxygen presence is that the surface was not smooth and may have several nano and micro cracks. Therefore, the oxide presence on the surface could be detected even for extended periods of vigorous ion bombardment.

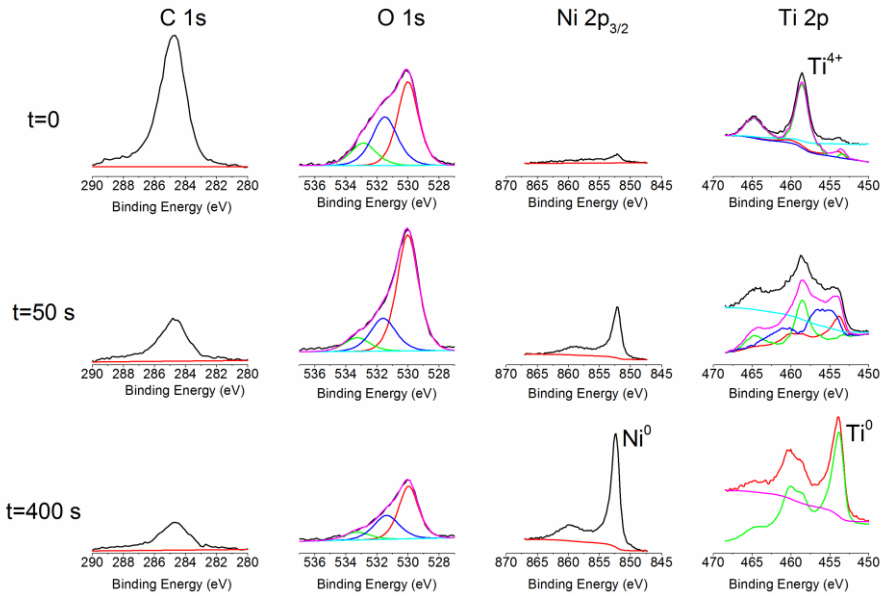

Figure 4.6. The XPS spectra recorded during the depth profiling of the archwire immersed in AS with a pH of 2.3 for 30 days.

In addition to the dissolution-reformation cycle, the oxide layer thickness has also a critical effect on the ion release behavior from the archwire into the AS solution, such that when the oxide layer dissolves the total amount of ions in the AS solution increases [2]. This can be verified by examining the ICP-MS data obtained from the archwires immersed in the AS solution for different immersion periods (Figure 4.4). For instance the significant decrease observed in the oxide layer thickness from D1 to D7 is noteworthy because dissolution of the oxide layer leads to the release of notable amount of Ti ions from the oxide and Ni ions either from the substrate or Ni-rich sublayers [4]. After D7, the Ti ions released in the AS solution takes role in the reformation of the oxide layer in D14, which explains the decrease of the amount of Ti ions in the AS. During this reformation, Ni ions move towards the oxide metal interface where they can join the bulk, form different compounds underneath or within the TiO_2 layer. In particular, the ICP-MS results show that on D1 the total amount of Ti ion is more than that of Ni ions. This can be due to the initial release of the Ti ions from the initial protective oxide layer on the outer surface of the archwires. Therefore, to attack the Ni-rich layers or substrate, and lead to Ni ion release, aggressive chloride ions need to move through the oxide layer and reach underneath. However, from D1 to D7, the total Ni ion release exceeded the Ti ion release, which can be associated with the stability of the Ti oxide layer [34].

The surface roughness of the archwires also plays a critical role on their biocompatibility, and the efficiency of the medical treatment [17]. Specifically, any irregularities on the archwire surface create high energy regions, which become more prone to corrosion, and thus, enhance ion release. In order to eliminate this unfavorable ion release, surface uniformity and quality need to be ensured [4,35,36]. However, SEM analysis of the as-is archwires demonstrated that irregularities and/or imperfections were present on the surfaces, increasing the surface roughness and potentially enhancing the corrosion assisted ion release (an example is shown in Figure 4.7).

Thus, for an efficient orthodontic treatment and for the sake of biocompatibility, maintaining high quality during the manufacturing of the archwires is of utmost importance.

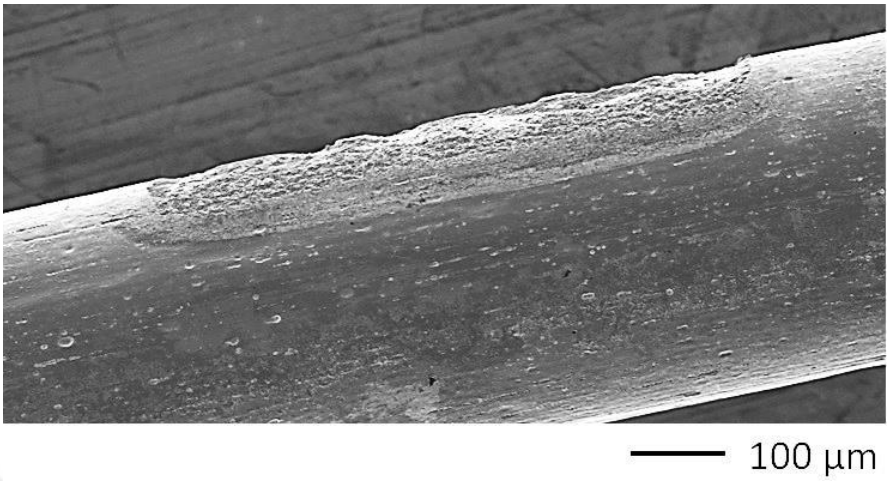

Figure 4.7. The deteriorated portion of surface on an as-is NiTi orthodontic archwire.

Surface roughnesses (R_a) of the archwires which were immersed for 1, 7, 14 and 30 days in the AS solution with 2.3 pH, and those immersed in the AS solutions with the pH values of 3.3 and 4.3 for 30 days were evaluated with AFM, and the corresponding results are listed in Table 4.3.

Table 4.3. Surface roughnesses (R_a, in nm) of the archwires immersed in AS with pH values of 2.3, 3.3 and 4.3 for 1,7,14 and 30 days of immersion periods.

As-is 72.1 ± 3.8		***Immersion Period (days)***			
		D1	**D7**	**D14**	**D30**
Solution pH	**2.3**	78.2 ± 3.86	81.7 ± 4.3	50.6 ± 4.8	53.1 ± 4.55
	3.3	**-**	**-**	**-**	51.3 ± 5.62
	4.3	**-**	**-**	**-**	56.45 ± 7.2

Accordingly, the surface roughness increased slightly when the archwire was immersed in the AS solution and subjected to corrosion even only for 1 day which might stem from a weaker protection against corrosion because of a thinner oxide layer. Between D1 and D7 R_a continued to increase, which verifies the corrosive effect of the AS between D1 and D7. This result is compatible with the oxide layer thickness and the ion release measurements, such that in this immersion period (D1-D7) archwire surface was attacked by Cl ions, which eventually leads to oxide layer dissolution, enhances ion release and increases the surface roughness. However, the roughness analysis of the archwire immersed for 14 days revealed a drastic decrease in roughness from D7 to D14. This result also affirms the findings of the oxide layer and ion release measurements, such that Ti ions form the Ti oxide with the dissolved oxygen in the AS, and this reformed oxide layer deposits specifically over the grooves within the peaks and valleys of the archwire which possess relatively larger surface energy, making the reformation easier, and eventually resulting in a smoother archwire surface (Figure 4.8) [17]. Specifically, the deposition of the corrosion products on cracks, pitting sites or surface defects is favored because of their greater surface energy [2,14,17]. Eventually, oxide layer formation on the rough regions leads to the decrease of surface roughness, meanwhile the ion release is hindered owing to the thicker oxide layer. From D14 to D30 a slight increase in the roughness was observed, implying that the oxide layer formation had reached to a more stable state.

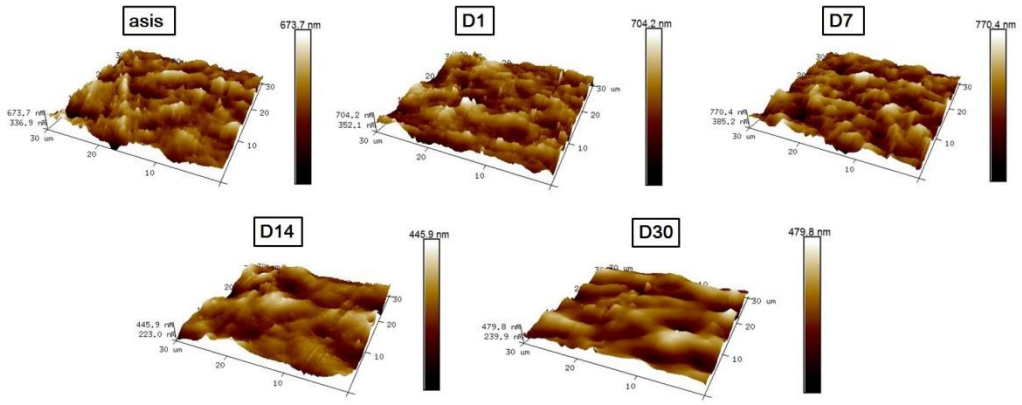

Figure 4.8. AFM images representing the surface topographies of the NiTi archwires immersed in the AS with pH 2.3 for 1, 7, 14 and 30 days of immersion period (referred to as D1, D7, D14

and D30, respectively). An as-is archwire surface topography was also inserted in the figure for comparison purpose.

4.4 Conclusions

The experimental work presented in this paper showed that the protective titanium oxide layer on the NiTi orthodontic archwires studied in the current work undergoes dissolution and reformation cycle within the first 14 days of the immersion period. The archwires immersed in artificial saliva (AS) solution for different time periods (1, 7, 14 and 30 days) and pH values (2.3, 3.3 and 4.3) exhibited the greatest amount of Ni ion release within the first 7 days of the immersion, i.e. the dissolution of the oxide layer; whereas the net ion release decreased significantly along with the reformation of the oxide layer within days 7-14. The change of the surface roughness was observed to stand in good agreement with the dissolution-reformation cycle, such that the reformation of the oxide layer within the peaks and valleys of the archwire surface resulted in a significant decrease of the surface roughness. Additional immersion experiments carried out in the AS solutions with different pH values clearly presented the aggressive effect of the most acidic environment (pH=2.3) with the deteriorated surface and enhanced ion release. In addition, the surface defects due to the manufacturing processes were observed to enhance corrosion. Overall, the current findings clearly demonstrated that the oxide layer dissolution-reformation cycle needs to be analyzed thoroughly along with surface roughness and ion release behavior in order to ensure the highest biocompatibility standards for NiTi orthodontic archwires.

4.5 References

[1] H. Tian, D. Schryvers, D. Liu, Q. Jiang, J. Van Humbeeck, Stability of Ni in nitinol oxide surfaces., Acta Biomaterialia. 7 (2011) 892–9. doi:10.1016/j.actbio.2010.09.009.

[2] S.M. Toker, D. Canadinc, H.J. Maier, O. Birer, Evaluation of passive oxide layer

formation-biocompatibility relationship in NiTi shape memory alloys: Geometry and body location dependency., Materials Science & Engineering C, Materials for Biological Applications. 36 (2014) 118–29. doi:10.1016/j.msec.2013.11.040.

[3] P.A. Trepanier C, Venugopalan R, Corrosion resistance and biocompatibility of passivated NiTi, Springer Berlin Heidelberg, 2000.

[4] L. Zhu, C. Trépanier, A.R. Pelton, J. Fino, Oxidation of Nitinol and Its Effect on Corrosion Resistance, in: 2003: pp. 156–161.

[5] L.G. Machado, M. a Savi, Medical applications of shape memory alloys., Brazilian Journal of Medical and Biological Research = Revista Brasileira de Pesquisas Médicas E Biológicas / Sociedade Brasileira de Biofísica [et Al]. 36 (2003) 683–91. http://www.ncbi.nlm.nih.gov/pubmed/19221641.

[6] S. Shabalovskaya, G.C. Rondelli, A.L. Undisz, J.W. Anderegg, T.D. Burleigh, M.E. Rettenmayr, The electrochemical characteristics of native Nitinol surfaces., Biomaterials. 30 (2009) 3662–71. doi:10.1016/j.biomaterials.2009.03.034.

[7] T. Duerig, The Use of Superelasticity in Modern Medicine, MRS Bulletin. February (2002) 101–104.

[8] J. Ryhänen, E. Niemi, W. Serlo, E. Niemelä, P. Sandvik, H. Pernu, T. Salo, Biocompatibility of nickel-titanium shape memory metal and its corrosion behavior in human cell cultures., Journal of Biomedical Materials Research. 35 (1997) 451–7. http://www.ncbi.nlm.nih.gov/pubmed/9189823.

[9] S.M. Toker, D. Canadinc, Evaluation of Biocompatibility of NiTi Dental Wires: A Comparison of Laboratory Experiments and Clinical Conditions, Materials Science and Engineering: C. 40 (2014) 142–147. doi:10.1016/j.msec.2014.03.060.

[10] D.J. Wever, A.G. Veldhuizen, M.M Sanders, J.M. Schakenraad, J.R. Van Horn, Cytotoxic ,

allergic and genotoxic activity of a nickel-titanium alloy, Biomaterials. 18(16) (1997), 1115–1120.

[11] K. Otsuka, X. Ren, Recent developments in the research of shape memory alloys, Intermetallics. 7 (1999) 511–528. doi:10.1016/S0966-9795(98)00070-3.

[12] L. Petrini, F. Migliavacca, Biomedical Applications of Shape Memory Alloys, Journal of Metallurgy. 2011 (2011) 1–15. doi:10.1155/2011/501483.

[13] S. Shabalovskaya, H. Tian, J.W. Anderegg, D.U. Schryvers, W.U. Carroll, J. Van Humbeeck, The influence of surface oxides on the distribution and release of nickel from Nitinol wires., Biomaterials. 30 (2009) 468–77. doi:10.1016/j.biomaterials.2008.10.014.

[14] T. Hu, C. Chu, Y. Xin, S. Wu, K.W.K. Yeung, P.K. Chu, Corrosion products and mechanism on NiTi shape memory alloy in physiological environment, Journal of Materials Research. 25 (2010) 350–358. doi:10.1557/JMR.2010.0051.

[15] X. Li, J. Wang, E. Han, W. Ke, Influence of fluoride and chloride on corrosion behavior of NiTi orthodontic wires., Acta Biomaterialia. 3 (2007) 807–815. doi:10.1016/j.actbio.2007.02.002.

[16] F. Ma, Corrosive Effects of Chlorides on Metals, INTECH Open Access Publisher, 2012. doi:DOI: 10.5772/32333.

[17] B. Uzer, B. Gumus, S.M. Toker, D. Sahbazoglu, D. Saher, C. Yildirim, S. Polat-Altintas, A Critical Approach to the Biocompatibility Testing of Niti Orthodontic Archwires, International Journal of Metallurgy and Metal Physics. 1 (2016) 1–7.

[18] J. Wang, N. Li, G. Rao, E.-H. Han, W. Ke, Stress corrosion cracking of NiTi in artificial saliva., Dental Materials : Official Publication of the Academy of Dental Materials. 23 (2007) 133–137. doi:10.1016/j.dental.2006.01.001.

[19] R.M. Castro, P.S. Neto, M.C.R. Horta, M.M. Pithon, D.D. Oliveira, Comparison of static friction with self-ligating, modified slot design and conventional brackets., Journal of Applied Oral Science : Revista FOB. 21 (2013) 314–9. doi:10.1590/1678-775720130097.

[20] C. Bourauel, T. Fries, D. Drescher, R. Plietsch, Surface roughness of orthodontic wires via atomic force microscopy, laser specular reflectance, and profilometry., European Journal of Orthodontics. 20 (1998) 79–92. doi:10.1093/ejo/20.1.79.

[21] T. Hanawa, In vivo metallic biomaterials and surface modification, Materials Science and Engineering A. 267 (1999) 260–266.

[22] H. Kim, J.W. Johnson, Corrosion of stainless steel, nickel-titanium, coated nickel-titanium, and titanium orthodontic wires. Angle Orthodontist. 69 (1999) 39–44.

[23] H.H. Huang, Surface characterizations and corrosion resistance of nickel-titanium orthodontic archwires in artificial saliva of various degrees of acidity. Journal of Biomedical Materials Research - Part A. 74 (2005) 629–639.

[24] R.G. Schipper, E. Silletti, Vingerhoeds, M.H.: Saliva as research material: biochemical, physicochemical and practical aspects. Archives of Oral Biology. 52 (2007) 1114–1135.

[25] M.W. Dodds, D.A. Johnson, C.K. Yeh, Health benefits of saliva: a review. Journal of Dentistry. 33 (2005) 223–233

[26] A.M. Diaz-Arnold, C.A. Marek, The impact of saliva on patient care: A literature review. Journal of Prosthetic Dentistry. 88 (2002) 337–343.

[27] J.L. Chicharro, A. Lucía, M. Pérez, A.F. Vaquero, R. Ureña, Saliva composition and exercise. Sports Medicine. 26 (1998) 17–27.

[28] S. Chiappin, G. Antonelli, R. Gatti, F. Elio, Saliva specimen: A new laboratory tool for diagnostic and basic investigation. Clinica Chimica Acta. 383 (2007) 30–40.

[29] O. Onal, B. Gumus, B. Aksoy, G. Gerstein, B.E. Alaca, H.J. Maier, D. Canadinc, Micro-scale cyclic bending response of NiTi shape memory ally. Mater. Trans. 57 (2016) 472-475.

[30] R.A. Corbett, Corrosion Tests and Standards: Application and Interpretation-Second Edition (2005)

[31] H.H. Huang, Y.H. Chiu, T.H. Lee, S.C. Wu, H.W. Yang, K.H. Su, C.C. Hsu, Ion release from NiTi orthodontic wires in artificial saliva with various acidities, Biomaterials. 24 (2003) 3585–3592.

[32] M. Kuhta, D. Pavlin, M. Slaj, S. Varga, M. Lapter-Varga, M. Slaj, Type of archwire and level of acidity: Effects on the release of metal ions from orthodontic appliances. Angle Orthodontist. 79 (2009) 102–110.

[33] G.S. Firstov, R.G. Vitchev, H. Kumar, B. Blanpain, J. Van Humbeeck, Surface oxidation of NiTi shape memory alloy, 23 (2002) 4863–4871.

[34] J. Ryhänen, Biocompatibility Evaluation of Nickel- Titanium Shape Memory Metal Alloy. Springer (1999)

[35] H.H. Huang, Corrosion resistance of stressed NiTi and stainless steel orthodontic wires in acid artificial saliva. Journal of Biomedical Materials Research Part A. 66 (2003) 829–839.

[36] C. Trepanier, M. Tabrizian, L.H. Yahia, L. Bilodeau, D.L Piron, Effect of modification of oxide layer on NiTi stent corrosion resistance. Journal of Biomedical Materials Research. 43 (1998) 433–440.

5. A CRITICAL APPROACH TO THE BIOCOMPATIBILITY TESTING OF NiTi ORTHODONTIC ARCHWIRES

The study explained in the previous chapter constitutes significance in the pursuit to better understand the biocompatibility of the metallic implants. The relation of the Ni ion release with the oxide layer dissolution-reformation cycle was figured out with a static immersion technique without incorporating the realistic mechanical loads on the archwires throughout the experiment period. Therefore the following experiment was carried out in order to comprehend the ion release behavior which would give more realistic results.

5. 1 Introduction

Nickel-Titanium (NiTi) shape memory alloys continue to attract significant attention in medicine due to their superior shape memory and pseudoelastic properties, especially in the fields of cardiovascular surgery and orthodontics [1-4]. The pseudoelastic behavior stands out in dental applications: for instance, in the case of orthodontic archwires, the pseudoelastic property of NiTi makes the application of constant stress possible over large tooth displacements [1,2], which not only minimizes tissue damage during treatment [5], but also eliminates readjustment procedures - which are quite uncomfortable for the patients - required for archwires made of conventional materials, such as medical grade stainless steel [1,6-9]. Specifically, the austenite-to-martensite phase transformation above the austenite finish temperature (A_f) and under straining beyond the elastic limit of the NiTi alloy leads to a state of constant stress, which is known as pseudoelasticity [10].

Despite their remarkable pseudoelastic capacity and wide utility in medical applications, the biocompatibility of NiTi alloys is still subject to debate, mainly due to potential Ni release, which can lead to serious health problems, especially in Ni-allergic patients [11,12]. It has been shown that, nickel hypersensitivity is one of the most commonly encountered adverse effects of NiTi archwires by orthodontists [12]. Specifically, Ni ions released into the intraoral cavity may cause

complications, such as burning sensations and inflammation around or in the mouth, and gingival hyperplasia [12]. Therefore Ni ion release is very critical in terms of determining the biocompatibility of NiTi archwires. The Ni ion release depends mainly on the applied stress state, and the type of body fluid (or tissue) the sample comes into contact with [11]. Specifically, it has been demonstrated that Ni ion release increases concomitant with both plastic deformation and acidity of the fluid [11,13]. Furthermore, the geometry of the sample has been demonstrated to play a vital role in the ion release behavior, where the corresponding surface finish and properties dictate the amount of ion release along with the fluid contacting the material [11]. Furthermore, hardness, topography and roughness were also showed to significantly influence the corrosion behavior and biocompatibility [14]. As for the effect of applied stress on the Ni ion release behavior, biocompatibility experiments featuring both static [5,13] and cyclic [15,16] loads on NiTi samples have been carried out, where the loading was restricted to simple three-point bending, which does not represent the actual stress state of archwires during clinical treatment.

The sliding mechanism, which is defined as the movement of the teeth and brackets along the archwire, plays also a significant role in achieving a successful and comfortable orthodontic treatment [17]. The effect of archwire surface hardness, topography and roughness on an efficient arch-guided tooth movement has been pointed out in numerous studies [14,18-20]. Specifically, the sliding mechanism is strongly influenced by the friction force present in the archwire-bracket contact sites [20], which depends on the type of orthodontic archwire used for the treatment and its surface roughness [17]: the bracket slot roughness has a positive correlation with the frictional force and it adversely affects the smooth movement of teeth throughout the treatment [20]. In addition, the stresses developed at these contact sites can lead to further Ni ion release [11], and therefore, the roughness of archwire-bracket contact sites constitute one the most important parameters affecting the orthodontic treatment [20]. The archwire manufacturers aim to minimize the roughness of these sites in order to achieve a more efficient sliding mechanism [17,20,21], and therefore the roughness of these sites have been analyzed in detail by

mechanical testing of various archwire and bracket sets [18,20,21]. However, these testing methods fell short of simulating the realistic conditions of the chemical and mechanical contact conditions of exposure in the actual intraoral cavity. Thus, in order to reduce the friction force and attain an efficient sliding mechanism, the stress-assisted corrosion cracking (SCC) needs to be incorporated into the *ex-situ* experiments.

The importance of adopting a more realistic loading scenario becomes more clear once the possibility of SCC is realized, where applied stress enhances crack initiation on the surface, and then crack propagation from surface into the bulk in corrosive environments [15]. In the case of NiTi alloys, the core of the material becomes exposed directly to the corrosive environment if the protective film that formed during the initial processing is damaged under applied stress, which leads to Ni release [22]. In addition, the chemically-, thermally- or stress-induced changes in the surface properties, such as surface roughness and morphology, promote crack initiation and/or propagation due to dissolution [23-25].

Despite the findings forwarded on the Ni ion release and corrosion behavior of NiTi orthodontic archwires [5,11-13,15,16,25-30], to the best of the authors' knowledge, an investigation focusing on the biocompatibility and Ni ion release behavior of NiTi alloys in the presence of SCC, and under realistic chemical and mechanical contact conditions has not been forwarded yet. The current work was undertaken with the motivation of addressing this issue, such that laboratory experiments closely simulating the actual clinical conditions were designed and carried out on commercially available NiTi orthodontic archwires. For this purpose, static immersion experiments were carried out in artificial saliva (AS) with the incorporation of mechanical contact of archwires and brackets. Specifically, NiTi archwires were subjected to AS for 31 days while attached to brackets fixated on upper dental arch mold model of an actual patient. This allowed for the simulation of the stresses that arise by the contact of wires with brackets and remain constant on the wire throughout the treatment with the alignment of the teeth owing to the pseudoelastic property of the archwire. Following the immersion experiments,

both the NiTi archwires and AS solutions were inspected for changes in chemical content, and the surface properties of the tested archwires were carefully monitored. The outcomes of these analyses clearly demonstrate the necessity of simulating both chemical and mechanical contact within the intraoral cavity while carrying out laboratory experiments, for the sake of a realistic biocompatibility assessment.

5.2 Materials and Methods

The current work employed static immersion experiments in AS in order to investigate the stress-assisted corrosion-induced changes in the surface properties of and possible ion release from NiTi orthodontic archwires[1] in intraoral cavity. Specifically, metal brackets[2] were fixated to a dental mold model made of acrylic, and were bonded to the dental mold with light cure adhesive (3M Unitek Transbond XT).

In this study, the commercially available heat activated NiTi archwires [3] with a chemical composition of 54.5-57 wt.% Ni [31] were utilized. The orthodontic archwires exhibit variety in their austenite finish temperatures (A_f) depending on their chemical compositions or manufacturing processes [32]. The NiTi alloy utilized in the current study had an A_f temperature ranging between 20-40°C [31]. The amount of force which moves the teeth throughout the orthodontic treatment was measured with three point bending test and found to be in a range of 0.6-1.0 N at 3mm deflection [31]. The archwires were placed into the bracket slots with the following sequence: both bonding of the brackets and the binding procedure were performed from upper left second premolar to upper right second premolar. The NiTi archwire was bound conventionally with ligature wire. The archwire was inserted passively because there was no crowding or rotations on plaster models. This passive bound was found sufficient to simulate the aimed mechanical contact, since the NiTi wires used in the current study have the ability to retain

[1] 3M Unitek Smart Clip Nitinol heat activated archwires with 0.36mm diameter were used in the experiments.
[2] 18' slot 3M Unitek Gemini Roth brackets and the corresponding metallic bases were manufactured from17-4PH and 304L stainless steels, respectively.

at almost a constant stress throughout the alignment of the teeth during treatment, owing to their pseudoelastic properties. Three different sets of experiments were carried out to detect the amount of Ni ions released both from the archwire and the brackets individually, and each individual set was repeated for at least three times for the sake of reliability and statistical consistency. The first experimental set considered the immersion of the undeformed archwire only (UA) (Figure 5.1-a), while the second set also included the dental model with only brackets bonded on (B) (Figure 5.1-b). The third experimental set featured the dental model with the brackets, and the archwire bound on the brackets (BA) (Figure 5.1-c).

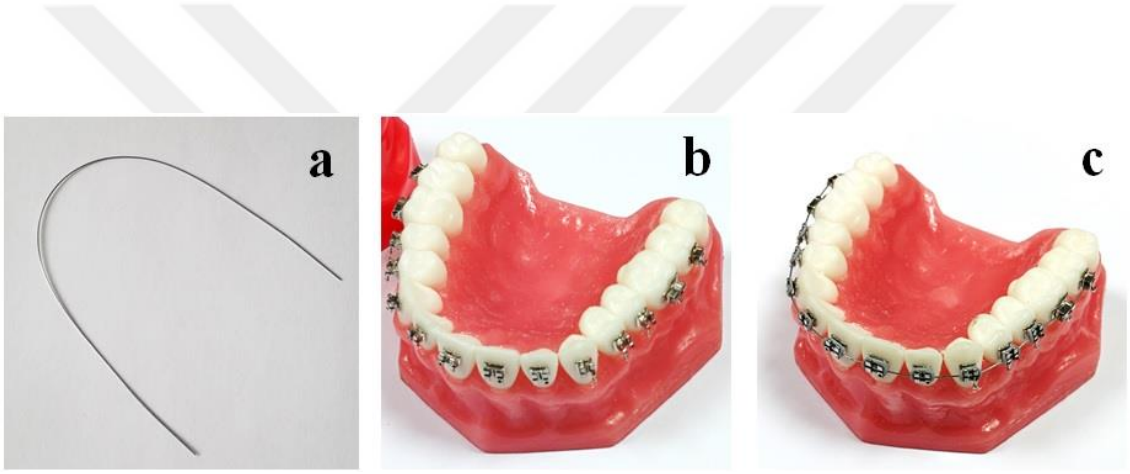

Figure 5.1. Three different experimental sets prepared for the immersion experiments: **(a)** UA: the undeformed archwire, **(b)** B: the dental model with only brackets bonded on, and **(c)** BA: the dental model both with brackets bonded on and archwire bound on the brackets.

These sets were subjected to static immersion in AS for 31 days in separate containers and the released ions from each set were detected by Inductively Coupled Plasma-Mass Spectroscopy (ICP-MS). The ingredients and the pH value of the AS employed in the current work are presented in Table 5.1. It should be noted that the pH of the natural saliva is about 7, however; a lower pH value (2.3) was preferred for AS in this study in order to incorporate the effects of acidic environment caused by possible dental plaque, and simulate the aggressive environment that would potentially stem from nutritional habits, and the corresponding organic depositions

and intraoral microorganisms [9,11,33]. Moreover, as the protective titanium-oxide layer is expected to undergo degradation at pH values below 3 [12], the pH value of 2.3 was also suitable in terms of incorporating the effects of changes in oxide-layer characteristics during the exposure to AS. While preparing the AS, 1M of HCl was slowly added to the initial AS solution with pH value of near 7 until a level of acidity corresponding to a pH value of 2.3 was attained [28,29,33]. The prepared fluid was initially observed to be stable and remained the same throughout the experiments confirming the absence of salt deposition. Each model was immersed in a separate sealed beaker with 180ml of prepared AS. The immersed samples were kept in an electronically controlled water bath sustaining the temperature at 37 °C, corresponding to the body temperature.

Table 5.1. Properties of the AS utilized in the current immersion experiments.

Ingredients	Amount of Ingredients (g/l)	pH
NaCl	0.4	2.3
KCl	0.4	
$CaCl_2$•$2H_2O$	0.906	
NaH_2PO_4•$2H_2O$	0.69	
Na_2S•$9H_2O$	0.005	
Urea	1	

Following an immersion period of 31 days, the immersed undeformed and bound archwires were comparatively investigated using scanning electron microscopy (SEM) and Energy dispersive X-ray spectroscopy (EDX) in order to detect SCC and the corresponding surface morphological changes, as well as to identify the elements deposited on the archwire and specifically on archwire-bracket contact sites. Three samples were analyzed via SEM and EDX for each different condition. The SEM and EDX analyses were conducted on an SEM, where the SEM images were captured with a secondary electron detector at a magnification of 1000 – 5000 ×, an accelerating voltage (EHT) of 5 kV, current of 30 pA and a working distance of 11mm.

The EDX results were obtained at an EHT of 10 kV and current of 1000 pA. Surface topography and roughness of each archwire, and the sites in contact with the brackets on the archwires were analyzed by atomic force microscopy (AFM). The AFM images were recorded at a tapping mode in air utilizing an antimony (n) doped silicon cantilever with a rotated tip with a radius of 8 nm. The linear scanning rate was set as 1 Hz (1 line/s) and the surface topography of the materials was monitored on 30 × 30 μm^2 scanning area.

The surface roughness results of the immersed archwires were compared with an as-is (as received from the manufacturer) archwire in order to better understand the corrosion induced roughness changes. Released Ni ions from the archwire and bracket sets in immersion fluids were detected with ICP-MS equipped with octopole reaction system helium collision cell for spectral interference removal, rather than ICP-OES, considering the μg/L (ppb) level ion detection capability of the former. The ICP-MS was operated with MicroMist glass concentric nebulizer, quartz Scott-type spray chamber and Ni sampler/skimmer cones. Daily instrumental optimizations were performed using 1 μg/L tuning solution for the short-term stability of the instrument. The corresponding instrument settings and parameters are provided in Table 5.2.

Table 5.2. ICP-MS operating parameters.

Number of points per peak	3	**Plasma gas flow (Argon)**	15L/min
Replicates	5	**Helium gas flow (Collision cell)**	4.3ml/min
Sweeps/replicate	100	**Carrier gas flow (Argon)**	1L/min
Total acquisition time	41.900s	**Plasma Forward Power**	1550W
Integration time per mass	0.12s		

5.3 Results and Discussion

The surfaces of the as-is NiTi archwire and, the archwires UA and BA which were immersed in artificial saliva for 31 days were investigated via SEM, EDX and optical microscopy following the immersion experiments and compared with the as-is archwire surface. The SEM images of the as-is, and UA and BA are presented in Figures 5.2-4. Figure 5.2 demonstrates that

the as-is archwire features a relatively smooth surface, except for the processing marks and rare impurities, implying that any foreign particle observed on the UA surfaces must be new structures that formed upon immersion in AS.

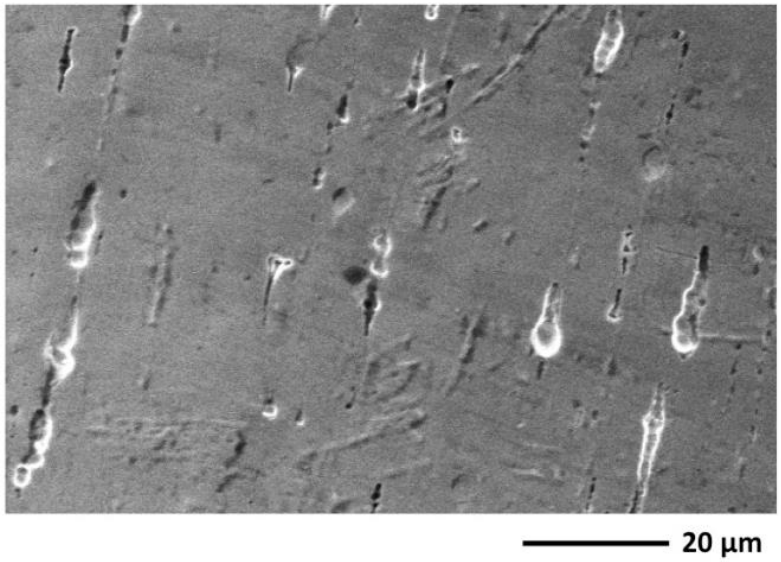

Figure 5.2. Representative SEM image of the as-is orthodontic archwire surface.

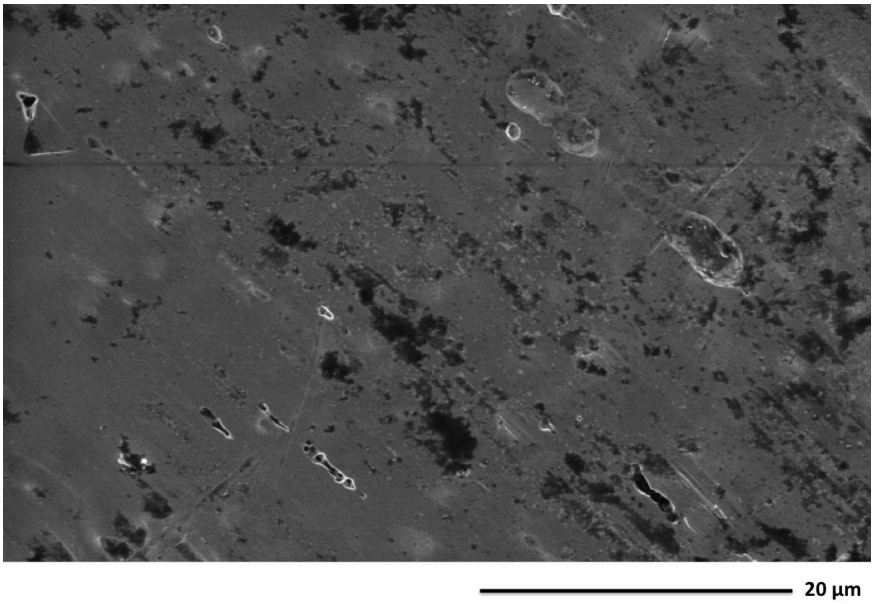

Figure 5.3. Representative SEM image of the undeformed orthodontic archwire (UA) surface immersed into AS.

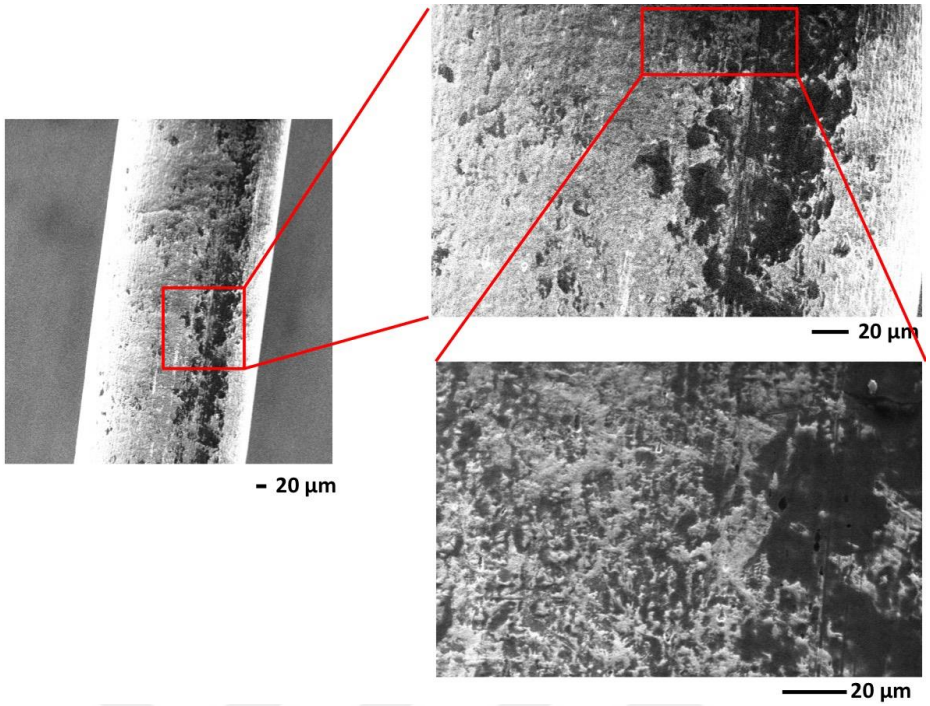

Figure 5.4. SEM images demonstrating C deposition on the bound orthodontic archwire (BA) immersed in AS.

The SEM images of the UA show rare dark spots which are randomly located on the archwire surface (Figure 5.3). Quantitative EDX analysis from these regions indicated that these dark spots are mainly C containing structures (Table 5.3). Considering the high C content of AS and the previous experience on the C deposition on NiTi upon immersion in AS [9,11], it can be argued that the observed C-rich particle formation on the immersed undeformed NiTi archwires is reasonable. The random localization of these particles on the archwire surface stems from the uniformity of the archwire and the lack of distinctive and repetitive structures on the archwire surface. Specifically, the only available sites for nucleation of new structures were the impurities, which were randomly distributed on the archwire surface, leading to this observed random deposition of corrosion products.

Table 5.3. Relative quantities of the elements (provided in wt.%) detected by energy dispersive X-ray spectroscopy (EDX) on the as-is archwire, and new structures present on the archwires UA and BA which were immersed in AS for 31 days (Figures 5.3 and 5.4). All the detected Ni and Ti quantities were found statistically significant with P<.01 for UA and P<.001 for BA. (Elements with signals lower than 0.1wt.% were not included in the table.)

	As-is	**UA**	**BA**
Carbon	**-**	4.59 ± 1.01	4.22 ± 0.47
Titanium	46.43 ± 0.78	46.06 ± 2.74	45.99 ± 1.23
Nickel	53.57 ± 0.78	49.36 ± 2.33	49.79 ± 1.14
Representative SEM images of the regions analyzed by EDX	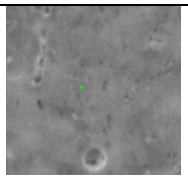 5μm	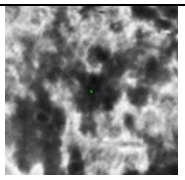 5μm	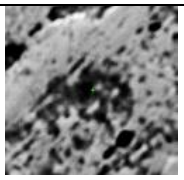 5μm

The SEM examination of the archwire-bracket contact sites in BA also demonstrated presence of dark spots, which, however; were located with certain intervals on the surface rather than a random localization (Figure 5.4). Furthermore, each spot occupied a wider area (Figure 5. 4) as compared to those observed on the immersed undeformed archwire (Figure 5.3). The quantitative EDX analysis indicated that these dark spots were also C-rich structures similar to those present on the UA (Table 5.3). In order to track the localization of all the corrosion products with certain intervals on the BA, the sample was also investigated with optical microscope, from which several images were gathered together for a more comprehensive picture of the overall archwire surface (Figure 5.5).

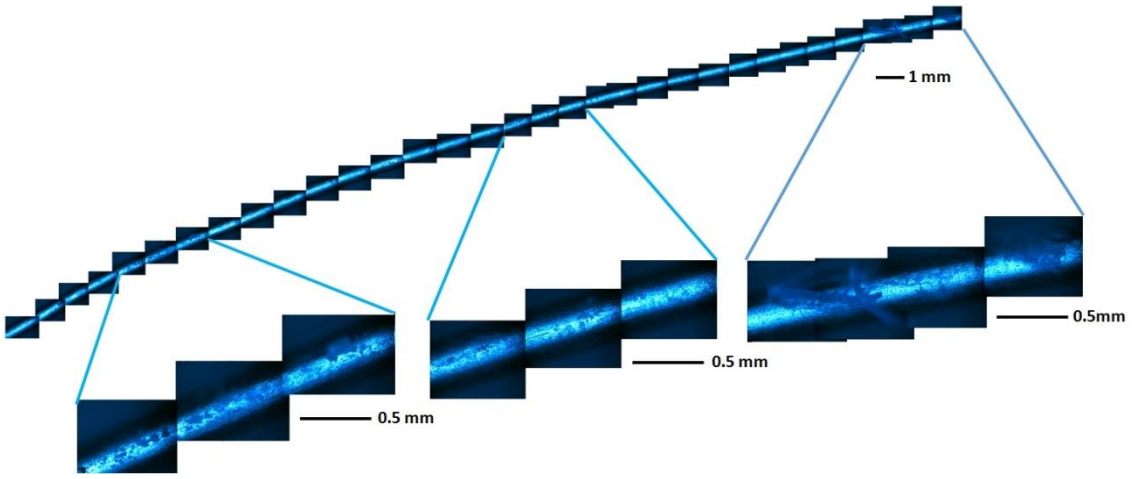

Figure 5.5. Optical microscope images of the bound orthodontic archwire (BA) immersed in AS Multiple high resolution images were gathered together to show the status of a meaningful segment of the wire upon being released from the mold.

The optical microscopy images clearly evidence the newly formed structures on the BA are located with almost equal intervals to each other (Figure 5.5). Moreover, measurement from the optical microscopy images demonstrates that the length of these intervals (about 1 cm) is close to the average distance between the brackets bonded to two consecutive teeth on the mold. This result justifies that the new particles are mainly deposited around the archwire-bracket contact zones. This localized precipitation of corrosion products is in good agreement with the findings of a similar study that compared an as-is archwire immersed in AS with a companion archwire that was retrieved from a patient after exposure to actual intraoral conditions for the same time interval [9]. Specifically, C-rich structure formation was observed on both archwires, however; the depositions on the retrieved archwires, which were localized at the archwire-bracket contact sites were dense enough to be visible to the naked eye. On the contrary, the deposition was random and observable only under SEM in the case of the immersed archwire [9]. This finding was attributed to the stress concentration induced by the contact of archwire and brackets, which created more available sites for the nucleation of corrosion products [9]. Similar observations were also made in a work where in-service SCC based fracture of NiTi archwires were examined [5]. Specifically, the microstructural and elemental analyses of the fracture surfaces showed that C

rich products precipitated in the vicinity of the crack tip, which constituted one of the highest stress concentration sites on the archwire [5].

In order to better understand the SCC effect on the archwires their surface topography and roughness were analyzed by AFM. Figure 5.6 compares the surface topographies of the two different archwires: UA and BA. The latter possesses a surface with denser peaks and valleys, which stems from the SCC at the archwire-bracket contact sites. The average roughness (R_a) values of each set are presented in Table 5.4. UA which was exposed to the corrosive environment of the AS for 31 days shows higher roughness value than the as-is archwire. On the other hand BA shows higher roughness value than the UA. This result shows that when the archwire is under the effect of both stress and corrosion its surface roughness increases more significantly. Moreover, the archwire-bracket contact site of the BA had the highest roughness value, which implies that the high energy regions create local higher roughness sites on the archwire surface, further contributing to the localized precipitation in these regions.

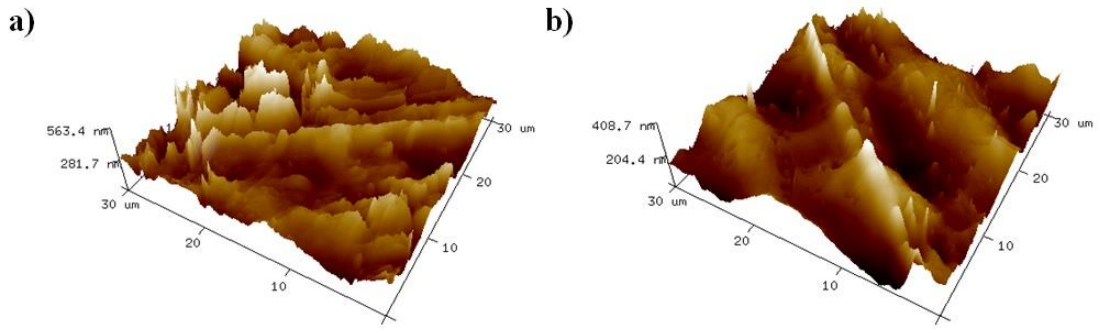

Figure 5.6. Surface topographies of the **(a)** undeformed (UA) **(b)** bound archwire (BA) obtained by AFM.

Table 5.4. AFM Surface roughness measurements of the archwires.

As-is	UA	BA
40.8nm	56.6nm	108nm

The simulation of the actual state of contact between the archwires and the brackets, and the incorporation of the mechanical conditions into *ex situ* experiments provided more realistic surface roughness results. It should be noted that in order to speculate on the effect of the roughness on the sliding mechanism the dynamic forces created by mastication and the chemical condition of the intra oral environment also need to be included in the experiments. Thereby, the friction coefficient of these sites can be minimized more significantly to achieve a more efficient sliding mechanism and orthodontic treatment.

The preferential particle deposition at stress concentration zones have been subject to several studies, which evidenced that grain boundaries, impurities and other stress concentration points create ideal sites for nucleation of new phases, where the existing high energy facilitates precipitation of new structures by spending minimum energy [34,35]. Similarly, the current results showed that the C ions within the AS solution preferentially pile up in the form of C- particles on the archwire-bracket contact sites of BA which had the highest surface roughness value. The higher surface energy of these sites has further catalyzed the deposition of the corrosion products [11].

Moreover, a closer look into these sites demonstrated that the stress induced by the contact of the archwire with brackets causes formation of micro-cracks on the archwire surface as a result of SCC (Figure 5.7(a)). Specifically, the archwire surface becomes more prone to the stress created at the bracket contact sites due to the corrosive nature of AS, which enables crack initiation and propagation. Similar to the aforementioned stress concentration sites, cracks also constitute high energy regions, and thus, favor deposition of corrosion products in their close

vicinity. Figure 5.7(b) evidences that the precipitates preferentially nucleate around the cracks on the BA. This argument is further strengthened by the random localization of corrosion products on the surface in the absence of micro-cracks in the case of the UA, which was not loaded during the immersion period. Therefore, formation and localization of new particles at certain locations with almost equal intervals, which correspond to the archwire-bracket contact sites, can be explained with the stress concentration created at these contact sites due to SCC and the resulting micro-cracks. Yet, in contrast to the archwire that was exposed to actual intraoral conditions [9], the C-rich structures nucleated on the BA were not visible to naked eye. This difference can be attributed to the more complex composition and variable constituents of actual intraoral environment, which involves not only the saliva but also the nutrients that are specific to the patient, implying that eating habits of the patient also significantly influence particle accumulation on the archwires in actual clinical conditions.

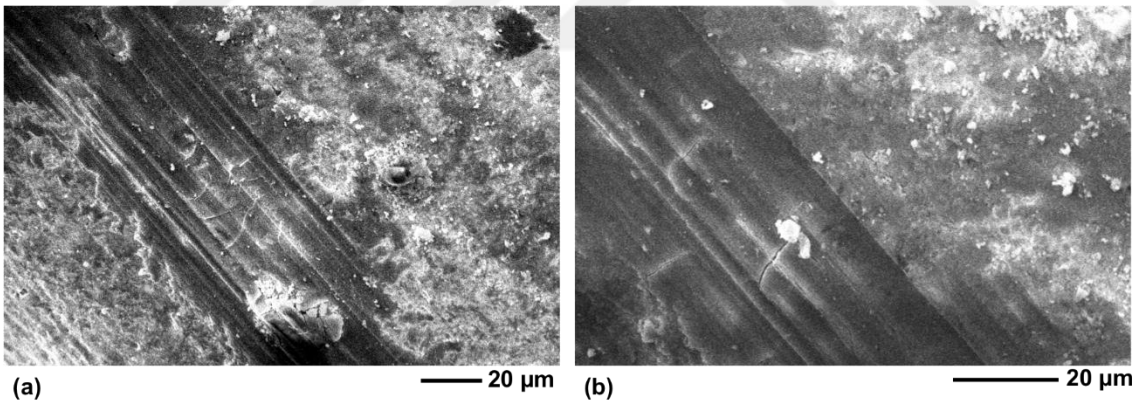

Figure 5.7. SEM images demonstrating **(a)** the crack formation due to SCC, and **(b)** the localization of the corrosion products near the cracks on the bound orthodontic archwire (BA) immersed in AS.

For the detection of potential Ni ion release from the archwires into the AS solutions and to investigate the effect of SCC on the ion release behavior of the archwires, all the AS solutions were subjected to ICP-MS following the experiments. The Ni amounts measured in the three test solutions are presented in Table 5. The amount of Ni ion release from the dental model with only

brackets was higher than the Ni ion release from the UA. This result shows that significant amount of Ni has released from the brackets. On the other hand AS with BA had the highest amount of released Ni ions when compared with the other AS sets. It is remarkable that the amount of Ni ions in the AS with BA was more than the total amount of the Ni ions released from the UA and the brackets. This result verifies the fact that extra Ni ion had released due to SCC and resulting cracks in the archwires. Considering the critical limit of Ni intake (0.12-0.5mg/L) the Ni contents of these 3 AS solutions were far below this limit and therefore doesn't constitute toxicity for human body [30], indicating that the commercially available NiTi archwires can be considered safe for the patients within the immersion period considered in the current experiments. This finding also demonstrates that the archwire-bracket contact zones did not significantly enhance ion release despite being ideal sites for deposition of corrosion products. This can be attributed to the micron-size cracks promoted by SCC, which were not large enough to lead to significant ion release, in addition to becoming blocked by the deposited corrosion products, further preventing ion release. As the new particle nucleation preferentially takes place at the contact regions and in the vicinity of cracks, it is suggested that the ion release from these zones was prevented by the particles deposited on the cracks. Moreover, the ICP-MS results demonstrated that, although BA exhibited the highest amount of Ni ion release compared to UA and B as a result of the SCC induced by wire-bracket contact, the released amount is still lower than the critical value which can be toxic for the human body, due to the prevention of further ion release by the preferential precipitation of corrosion products at potential ion release sites such as cracks. This finding is in good agreement with previously forwarded evidence for reduction in ion release due to oxide layer deposition on the stress-induced cracks [13].

Another mechanism which can be critical for the Ni release of NiTi archwires in contact with brackets is galvanic corrosion. The introduction of new archwires and brackets with novel materials and designs into the orthodontics offers orthodontists a variety of choice in their combination [36]. Among these different combinations researchers aim to find the specific

archwire-bracket combination providing the best treatment with the ultimate efficiency in the sliding mechanism [20]. When the selected archwire-brackets are composed of two different metals the contact of these two dissimilar metals can lead to galvanic corrosion in the existence of saliva [12,36,37]. However, previous analysis focusing on the galvanic corrosion of NiTi archwires demonstrated that different archwire-bracket combinations did not lead to significant Ni ion release [36]. Therefore, in the current study, galvanic corrosion was not considered as an effective mechanism for Ni release and was not separately analyzed.

Overall, the current results indicate that the stress concentration stemming from the archwire-bracket contact dictates both deposition of corrosion products on the surface and the ion release from orthodontic archwires. Moreover, the current set of experiments demonstrated that the actual intraoral conditions the orthodontic archwires become exposed to can be successfully simulated in terms of both physical and chemical conditions through static immersion experiments when archwire-bracket contact is provided.

5.4 Conclusions

The biocompatibility of commercial Nickel-Titanium (NiTi) orthodontic archwires was evaluated through *ex situ* experiments incorporating realistic chemical and mechanical contact conditions the archwires become subject to during actual intraoral stay. The results indicated that the archwire-bracket contact sites constitute critical regions for the deposition of corrosion products owing to elevated stress concentration, which creates high energy zones around the contact areas. On the other hand, these products prevented significant Ni or Ti ion release from the archwires by blocking the cracks formed as a result of SCC in the same areas. Moreover, the results of the experiments involving archwire-bracket contact significantly differed from the experiments where mechanical contact was not provided, such that the former set of experiments successfully simulated the actual intraoral cavity in terms of formation and localization of corrosion products at the archwire-bracket contact sites. Overall, the current study demonstrates

that the incorporation of both chemical and mechanical contact conditions of exposure in the actual intraoral cavity is necessary for a reliable biocompatibility experiment.

5.5 References

[1] R.J. Nikolai, Orthodontic wire: a continuing evolution., Semin. Orthod. 3 (1997) 157–165.

[2] T. Duerig, A. Pelton, D. Sto, An overview of nitinol medical applications, Mater. Sci. Eng. A. 275 (1999) 149–160.

[3] G. Mani, M.D. Feldman, D. Patel, C.M. Agrawal, Coronary stents: a materials perspective., Biomaterials. 28 (2007) 1689–1710.

[4] A. Bansiddhi, T.D. Sargeant, S.I. Stupp, D.C. Dunand, Porous NiTi for bone implants: a review., Acta Biomater. 4 (2008) 773–782.

[5] J. Wang, N. Li, G. Rao, E.-H. Han, W. Ke, Stress corrosion cracking of NiTi in artificial saliva., Dent. Mater. 23 (2007) 133–137.

[6] Z. Davidovitch, V. Krishnan, Role of basic biological sciences in clinical orthodontics: a case series., Am. J. Orthod. Dentofacial Orthop. 135 (2009) 222–231.

[7] H. Wehrbein, P. Göllner, Skeletal anchorage in orthodontics--basics and clinical application., J. Orofac. Orthop. 68 (2007) 443–461.

[8] A. Van Schepdael, J. Vander Sloten, L. Geris, Mechanobiological modeling can explain orthodontic tooth movement: three case studies., J. Biomech. 46 (2013) 470–477.

[9] S.M. Toker, D. Canadinc, Evaluation of Biocompatibility of NiTi Dental Wires: A Comparison of Laboratory Experiments and Clinical Conditions, Mater. Sci. Eng. C. 40 (2014) 142–147.

[10] S. Miyazaki, K. Otsuka, Development of shape memory alloys., ISIJ Int. 29 (1989) 353–377.

[11] S.M. Toker, D. Canadinc, H.J. Maier, O. Birer, Evaluation of passive oxide layer formation-biocompatibility relationship in NiTi shape memory alloys: Geometry and body location dependency., Mater. Sci. Eng. C. Mater. 36 (2014) 118–129.

[12] K. House, F. Sernetz, D. Dymock, J.R. Sandy, A.J. Ireland, Corrosion of orthodontic appliances--should we care?, Am. J. Orthod. Dentofacial Orthop. 133 (2008) 584–592.

[13] J.-K. Liu, T.-M. Lee, I.-H. Liu, Effect of loading force on the dissolution behavior and surface properties of nickel-titanium orthodontic archwires in artificial saliva., Am. J. Orthod. Dentofacial Orthop. 140 (2011) 166–176.

[14] C. Bourauel, F. Thomas, D. Dieter, P. Reinhard, Surface roughness of orthodontic wires via atomic force microscope, laser specular reflectance, and profilometry, The European Journal of Orthodontics. 20 (1998) 79-92.

[15] O. Prymak, A. Klocke, B. Kahl-Nieke, M. Epple, Fatigue of orthodontic nickel–titanium (NiTi) wires in different fluids under constant mechanical stress, Mater. Sci. Eng. A. 378 (2004) 110–114.

[16] A. Milheiro, C. Kleverlaan, J. Muris, A. Feilzer, P. Pallav, Nickel release from orthodontic retention wires-the action of mechanical loading and pH., Dent. Mater. 28 (2012) 548–553.

[17] M.R. Pacheco, C.J. Wellington, D.O. Dauro, The role of friction in orthodontics, Dental Press Journal of Orthodontics. 17 (2012) 170-177.

[18] T. Inami, T. Yasuhiro, Y. Masaru, S. Yo, N. Norihiro, K. Kazutaka, Surface topography, hardness, and frictional properties of GFRP for esthetic orthodontic wires, Journal of Biomedical Materials Research Part B: Applied Biomaterials. 104 (2016) 88-95.

[19] M. Iijima, M. Takeshi, A.B. William, M. Itaru, Comparisons of nanoindentation, 3-point bending, and tension tests for orthodontic wires, American Journal of Orthodontics and Dentofacial Orthopedics. 140 (2011) 65-71.

[20] U.H. Doshi, A.B. Wasundhara, Static frictional force and surface roughness of various bracket and wire combinations, Am. J. Orthod. Dentofacial Orthop. 139 (2011) 74-79.

[21] R.P. Kusy, Q.W. John, Friction between different wire-bracketconfigurations and materials, In Seminars in Orthodontics, WB Saunders. 3 (1997) 166-177.

[22] E.M. Al-Waheidi, Allergic reaction to nickel orthodontic wires: a case report., Quintessence Int. 26 (1995) 385–387.

[23] M.R. Grimsdottir, A. Hensten-Petterseri, Surface analysis of nickel-titanium archwire used in vivo, Dent. Mater. 13 (1997) 163–167.

[24] H.-H. Huang, Variation in surface topography of different NiTi orthodontic archwires in various commercial fluoride-containing environments., Dent. Mater. 23 (2007) 24–33.

[25] D.K. Pun, D.W. Berzins, Corrosion behavior of shape memory, superelastic, and nonsuperelastic nickel-titanium-based orthodontic wires at various temperatures., Dent. Mater. 24 (2008) 221–227.

[26] C. Heßing, J. Frenzel, M. Pohl, S. Shabalovskaya, Effect of martensitic transformation on the performance of coated NiTi surfaces, Mater. Sci. Eng. A. 486 (2008) 461–469.

[27] O. Mockers, D. Deroze, J. Camps, Cytotoxicity of orthodontic bands, brackets and archwires in vitro, Dent. Mater. 18 (2002) 311–317.

[28] T.H. Lee, C.C. Wang, T.K. Huang, L.K. Chen, M.Y. Chou, H.H Huang, Corrosion resistance of titanium-containing dental orthodontic wires in fluoride-containing artificial saliva. Journal of Alloys and Compounds. 488 (2009) 482-489.

[29] X. Li, J. Wang, E. Han, K.Wei, Influence of fluoride and chloride on corrosion behavior of NiTi orthodontic wires, Acta Biomater. 3 (2007) 807–815.

[30] H.-H. Huang, Y.-H. Chiu, T.-H. Lee, S.-C. Wu, H.-W. Yang, K.-H. Su, et al., Ion release from NiTi orthodontic wires in artificial saliva with various acidities, Biomaterials. 24 (2003) 3585–3592.

[31] Archwire NH. 3M Unitek Orthodontic Wire Properties – Nitinol Archwires 3M Unitek Orthodontic Wire Properties – Nitinol Archwires 3M Unitek Orthodontic Wire Properties – Nitinol Archwires (2014)

[32] V. Brosens, I. Ghijselings, M. Voet, P. Leemans, J.V. Humbeeck, G. Williems, Transformation Behaviour, Bending Properties and Surface Quality of 22 Commercial Nickel- Titanium Wires: A Batch-to-Batch Evaluation. Br J Med Med Res. 2 (2012) 597–620.

[33] R.R. Al-Hity, H.F. Kappert, S. Viennot, F. Dalard, B. Grosgogeat, Corrosion resistance measurements of dental alloys, are they correlated?, Dent. Mater. 23 (2007) 679–687.

[34] R. Huang, Y. Han, The effect of SMAT-induced grain refinement and dislocations on the corrosion behavior of Ti-25Nb-3Mo-3Zr-2Sn alloy., Mater. Sci. Eng. C. Mater. Biol. Appl. 33 (2013) 2353–2359.

[35] Y. Estrin, E.P. Ivanova, A. Michalska, V.K. Truong, R. Lapovok, R. Boyd, Accelerated stem cell attachment to ultrafine grained titanium., Acta Biomater. 7 (2011) 900–906.

[36] F. Heravi, N. Mokhber, E. Shayan, Galvanic Corrosion among Different Combination of Orthodontic Archwires and Stainless Steel Brackets, J Dent Mater Tech. 3 (2014) 118–122.

[37] M. Iijima, K. Endo, T. Yuasa, H. Ohno, K. Hayashi, M. Kakizaki, I. Mizoguchi, Galvanic corrosion behavior of orthodontic archwire alloys coupled to bracket alloys, Angle Orthod. 76 (2006) 705–711.

6. NANOTWIN FORMATION IN HIGH-MANGANESE AUSTENITIC STEELS UNDER EXPLOSIVE SHOCK LOADING

After thoroughly understanding the biocompatibility of the metallic materials under different circumstances and constructed its relationship with the microstructure of the material, further studies were carried out on the materials which facilitate the observation of complex microstructure. These materials were selected intentionally to better understand the activation of the plastic deformation mechanisms and observe the interaction with each other. In this way the knowledge gained from these studies would be utilized for the selection of the material with the ideal mechanical and microstructural properties in the applications including aerospace, automotive, civil engineering or biomedical.

6. 1 Introduction

Despite having been studied for decades, high-manganese austenitic steels continue to attract attention owing to the variety of active micro-deformation mechanisms and interactions [1–4], which are indeed responsible for the superior mechanical properties these materials possess, such as combined high strength, rapid strain hardening capability, high wear resistance and substantial elongation to failure [5–7]. The micro-deformation mechanisms facilitating this superior combination of mechanical properties include slip-twin interactions [7], slip - dense dislocation wall interactions [5,6], and as recently demonstrated, nanotwin formation within primary twins [7–10]. Most of the significant volume of work carried out on high-manganese austenitic steels, including Hadfield steel and twinning-induced plasticity (TWIP) steels, focused on the deformation response and the corresponding microstructure evolution of these materials at rather slow or medium rates of deformation [7], and the state of the micro-deformation mechanisms governing the high-velocity deformation behavior have been left unattended with the exception of a small number of studies [7,11].

Recent studies exploring the possibility of utilizing high-manganese austenitic steels as armor materials or improving their impact bearing capacities [8–10] led to important discoveries regarding the micro-deformation mechanisms active in high-manganese austenitic steels under high-velocity loading. In particular, nanotwin formation within primary twins has been shown to significantly increase the load bearing capacity of high-manganese austenitic steels when deformed at high velocity and low temperatures. When the primary twin formation or thickening cannot facilitate further deformation, enhanced hardening owing to the interaction with glide dislocations is expected to result in failure, however; nanotwin formation within the primary twins allows for plastic deformation to continue, and thus, enhances the material's capacity to absorb the applied loading [7–10].

The aforementioned observations were made for temperatures ranging from -170 °C to 200 °C and strain rates ranging from 300 1/s to 800 1/s were covered. However, in order to assess the suitability of high-manganese austenitic steels as armor materials or the basis for new generation ballistic protection technologies, a more realistic loading scenario is needed. In order to address this issue and to further investigate the micro-deformation mechanisms at very high deformation rates and high temperatures, a high-manganese austenitic steel was subjected to explosive shock loading utilizing military ballistic testing equipment, and the corresponding micro-deformation mechanism activities and interactions in the microstructure were studied in detail. Even though utilizing explosives under the laboratory conditions to induce hardening and severe plastic deformation on metallic materials, including Hadfield steel [12], to the best of the authors' knowledge, this is the first true ballistic experiment carried out on high-manganese austenitic steels in a military facility reported in the open literature. The current findings demonstrate that a single nanotwin system is activated within a single system of primary twins upon explosive loading, significantly enhancing the material's load bearing capacity. A comparison of the current findings with the previous reports of high-velocity deformation of

high-manganese austenitic steels revealed that the velocity of deformation is the dominant parameter governing the micro-deformation activities in this class of alloys.

6. 2 Experimental Details

The material studied in this work was an austenitic high-manganese steel with the following chemical composition: 12.340 wt.% Mn, 1.090 wt.% C, 0.432 wt.% Si, 0.148 wt.% Ni, 0.297 wt.% Cr, 0.035 wt.% V, 0.044 wt.% Co, 0.007 wt.% Ti, and balance Fe. The bulk material subjected to explosive loading was removed from a larger as-cast slab, such that the test block was in form of a rectangular prism with dimensions of 100 mm × 80 mm × 10 mm. The test block was removed from the as-cast steel slab utilizing electrical discharge machining (EDM) in order not to induce any residual stresses.

For applying the ultra-high speed deformation to the test block, explosive material equivalent of 50 g TNT was pasted in the middle of one of the 100 mm × 80 mm surfaces, and the explosion was carried out within a protective bunker. The resulting explosive shock loading is estimated to have caused a deformation velocity in excess of 500 m/s, corresponding to a strain rate beyond 1 × 104 s-1. Following the shock loading, the sample remained intact despite the large cracks along both of the longer edges and one of the shorter edges (Figure 6.1). In order to investigate the microstructure evolution due to shock loading, three slices were cut utilizing EDM as shown in Figure 6.1, such that the material volumes directly affected from the explosion (Sample 1) and the nearby locations (Samples 2 and 3) could be investigated in a comparative manner, in order to clearly reveal the role of deformation velocity on the micro-deformation mechanism activities.

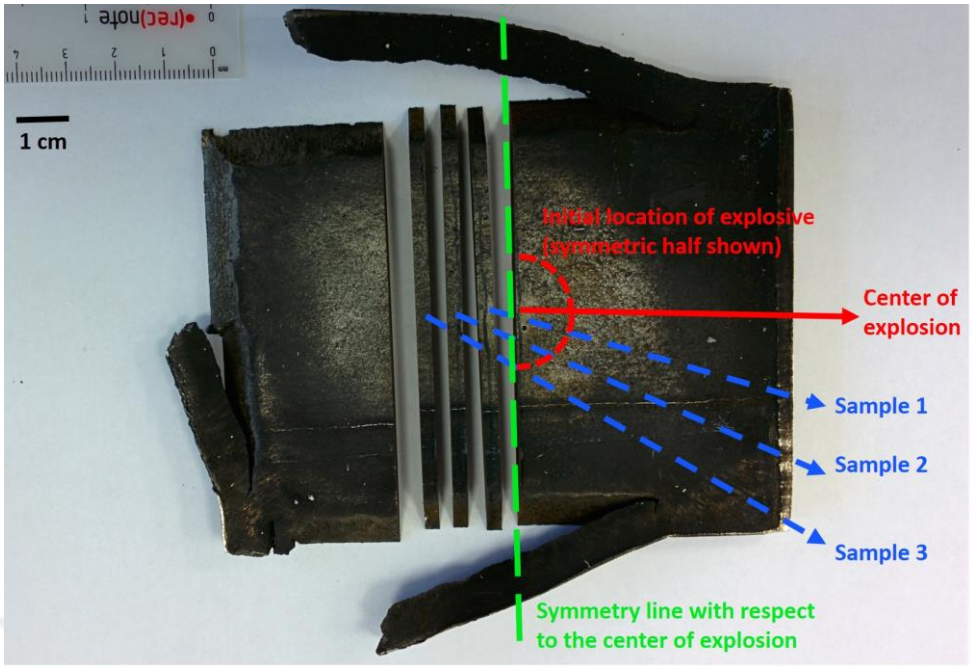

Figure 6.1. The high-manganese austenitic steel sample subjected to explosive shock loading following the experiment.

Microstructures of the samples were analyzed in detail utilizing a Tecnai G2 F30 transmission electron microscope (TEM) operating at an accelerating voltage of 300kV. A DualBeam NanoLab 600i focused ion beam (FIB) was employed to extract the TEM specimens from the bulk in lamella form. The TEM samples were extracted close to the surface that was subjected to the explosion. Prior to milling procedure, specimen surfaces with the dimensions of 2 μm × 16 μm were coated with a protective platinum layer of 1.5 μm thickness, which was followed by the milling of both sides with a (gallium ion) beam current of 6.5 nA until achieving a depth of 8μm. For the cross-section thinning, the specimens were milled down to 50 nm thickness using decreasing ion current in the following order: 2.8 nA, 0.28 nA, 48 pA and 28 pA. In the final step, both surfaces of the specimens were cleaned employing an accelerating voltage of 5 kV and a beam current of 47 pA for 90 seconds.

6.3 Results and Discussion

A comparison of the detailed microstructure analysis carried out on Samples 1 and 3 under the TEM revealed the significant differences between the microstructure evolutions at the center (Figure 6.2) and relatively remote from (Figure 6.3) the explosion. Accordingly, at the center of the explosion (Sample 1), forest hardening due to enhanced dislocation activity is evident, which is not surprising in this class of alloys due to the high strain rates attained during deformation [13]. In addition to dense dislocation activity, twinning is also prevalent, such that one major twin system is accompanied by nanotwins that formed within these primary twins (Figure 6.2). As opposed to Sample 1, Sample 3 exhibited only one major twin system in addition to dense dislocation activity (Figure 6.3), indicating that nanotwin formation within the primary twins is restricted to the zones affected the most from the explosion, i.e. where the rate of deformation was the highest. This is in agreement with previous reports on the impact response of Hadfield steel, where nanotwin formation within primary twinning was observed in the vicinity of the crack zones that were subjected to the largest plastic strains and highest rates of deformation [7]. Specifically, when the deformation rate is high, forest hardening and major mechanical twinning activity quickly saturate, and cannot proceed easily due to slip-slip, twin-twin or slip-twin interactions. However, if the material can still bear loading, an additional mechanism is needed in the microstructure for the plastic deformation to continue, which turns out to be nanotwin formation within primary twins. The dislocations interacting with the primary twin boundaries facilitate the nanotwin formation: the separation of full dislocations into a glissile Shockley and a sessile Frank partial, where the Frank partial acts as the anchored pole and the Shockley glissile revolves about the pole, creating twinned material upon each revolution [14]. When this interaction at the boundaries of the primary twins takes place in the undeformed zones within the primary twins, it leads to the formation of nanotwins. Such interaction of the dislocations at the twin boundaries is evident in Sample 1 (Figure 6.2(a)), whereas it was not prevalent in Sample 3 (Figure 6.3).

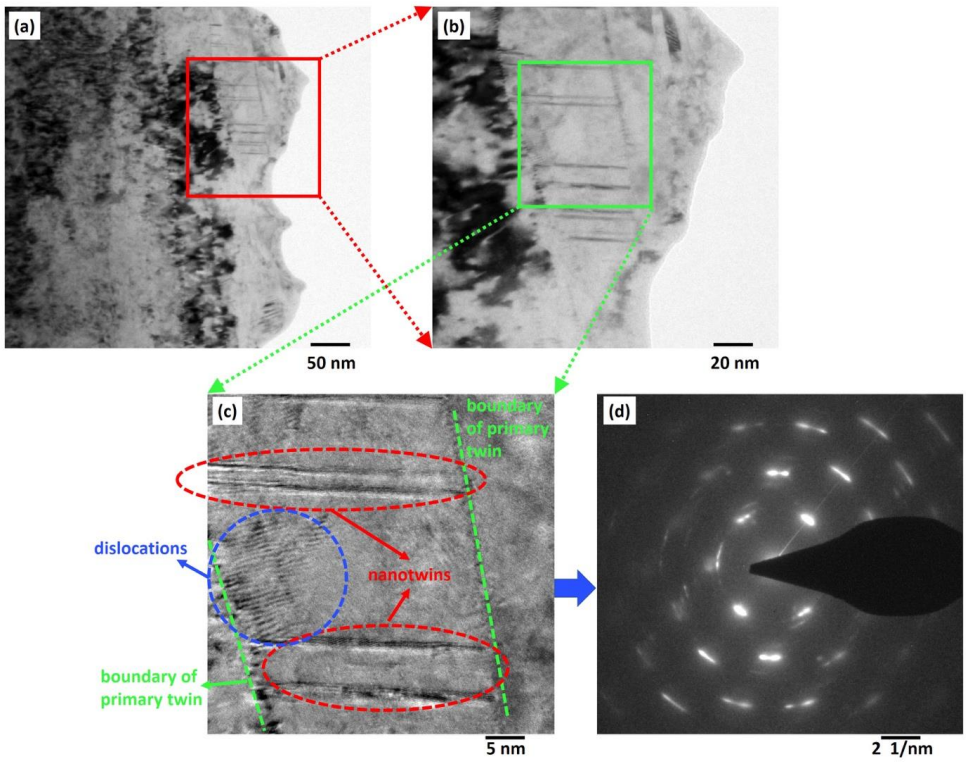

Figure 6.2. TEM images demonstrating the microstructure of Sample 1: (a) an overview showing nanotwins within a primary twin, and dislocations at the primary twin boundary, (b) high-magnification image of the selected area in (a), (c) high-magnification image of the selected area in (b), and (d) the SAD pattern corresponding to (c).

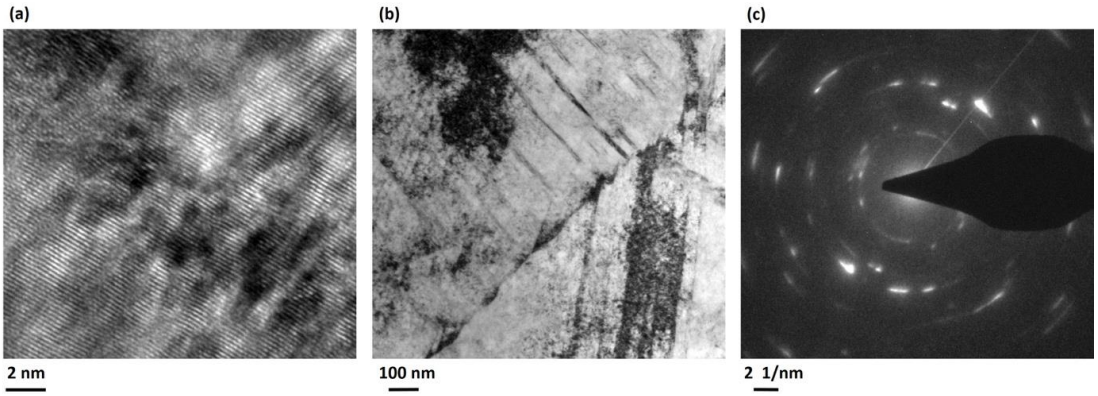

Figure 6.3. TEM images demonstrating the microstructure of Sample 3: mostly (a) dislocations and (b) primary twins are prevalent. (c) The corresponding SAD pattern.

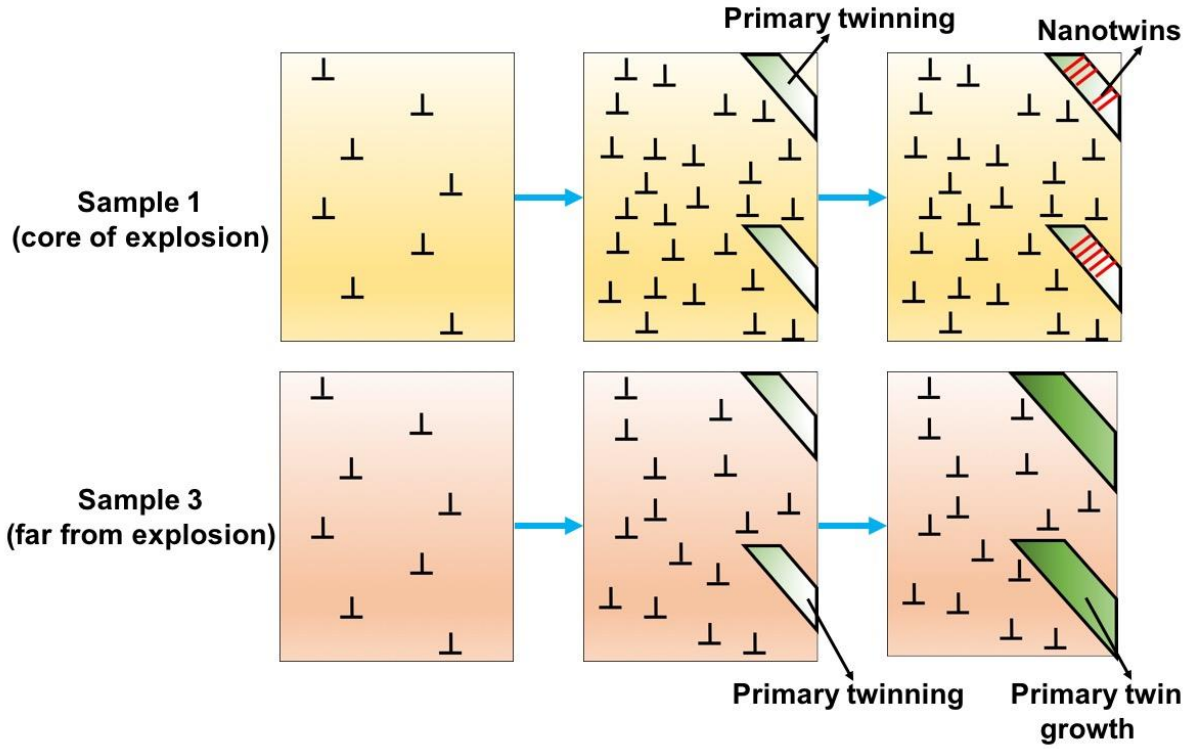

Figure 6.4. Schematic describing the microstructure evolution observed in Samples 1 and 3.

Another important observation is regarding the width of the primary twin bands in each case: a comparison of Figure 6.2(a) and Figure 6.3(b) reveals that the twin bands are much wider in the case of Sample 3 (Figure 6.3(b)), i.e. far from the center of the explosion. This can be explained by the continuous growth of the twins upon nucleation, while the faster deformation at the core of the explosion (Sample 1) does not leave much room for the growth of the nucleating primary twins due to more intense dislocation burst (Figure 6.4). Instead, nanotwins form within the primary twins, facilitating progression of the plastic deformation within the undeformed zones (Figure 6.4).

6.4 Conclusions

The current set of results clearly demonstrate that the ultra fast deformation of high-manganese austenitic steels promotes the formation of nanotwins within primary twins, which

emerges as a secondary mechanism plastic deformation relies on to continue despite the very high strains attained. Therefore, the current findings imply that the performance of both conventional and relatively new grades of high-manganese steels, such as TWIP steels, can be significantly improved under heavy service conditions upon facilitating nanotwin formation in the microstructure.

6.5 References

[1] D.V. Lychagin, A.V. Filippov, O.S. Novitskaia, Y.I. Chumlyakov, E.A. Kolubaev, O.V. Sizova, Friction-induced slip band relief of -Hadfield steel single crystal oriented for multiple slip deformation, Wear. 374–375 (2017) 5–14. doi:10.1016/j.wear.2016.12.028.

[2] A. Kwiatkowski da Silva, G. Leyson, M. Kuzmina, D. Ponge, M. Herbig, S. Sandlöbes, B. Gault, J. Neugebauer, D. Raabe, Confined chemical and structural states at dislocations in Fe-9wt%Mn steels: A correlative TEM-atom probe study combined with multiscale modelling, Acta Materialia. 124 (2017) 305–315. doi:10.1016/j.actamat.2016.11.013.

[3] M. Koyama, Y. Yamamura, R. Che, T. Sawaguchi, K. Tsuzaki, H. Noguchi, Comparative study on small fatigue crack propagation between Fe-30Mn-3Si-3Al and Fe-23Mn-0.5C twinning-induced plasticity steels: Aspects of non-propagation of small fatigue cracks, International Journal of Fatigue. 94 (2017) 1–5. doi:10.1016/j.ijfatigue.2016.09.003.

[4] C. Chen, F.C. Zhang, F. Wang, H. Liu, B.D. Yu, Effect of N+Cr alloying on the microstructures and tensile properties of Hadfield steel, Materials Science and Engineering A. 679 (2017) 95–103. doi:10.1016/j.msea.2016.09.106.

[5] D. Canadinc, H. Sehitoglu, H.J. Maier, Y.I. Chumlyakov, Strain hardening behavior of aluminum alloyed Hadfield steel single crystals, Acta Materialia. 53 (2005) 1831–1842. doi:10.1016/j.actamat.2004.12.033.

[6] D. Canadinc, H. Sehitoglu, H.J. Maier, D. Niklasch, Y.I. Chumlyakov, Orientation evolution in Hadfield steel single crystals under combined slip and twinning, International Journal of Solids and Structures. 44 (2007) 34–50. doi:10.1016/j.ijsolstr.2006.04.011.

[7] S.M. Toker, D. Canadinc, a. Taube, G. Gerstein, H.J. Maier, On the role of slip-twin interactions on the impact behavior of high-manganese austenitic steels, Materials Science and Engineering A. 593 (2014) 120–126. doi:10.1016/j.msea.2013.11.033.

[8] B. Gumus, B. Bal, G. Gerstein, D. Canadinc, H.J. Maier, F. Guner, M. Elmadagli, Twinning activity in high-manganese austenitic steels under high velocity loading, Materials Science and Technology. 32:5 (2016) 463–465. doi:10.1179/1743284715Y.0000000111.

[9] B. Gumus, B. Bal, G. Gerstein, D. Canadinc, H.J. Maier, F. Guner, M. Elmadagli, Twinning activities in high-Mn austenitic steels under high-velocity compressive loading, Materials Science and Engineering A. 648 (2015) 104–112. doi:10.1016/j.msea.2015.09.045.

[10] B. Bal, B. Gumus, G. Gerstein, D. Canadinc, H.J. Maier, On the micro-deformation mechanisms active in high-manganese austenitic steels under impact loading, Materials Science and Engineering A. 632 (2015) 29–34. doi:10.1016/j.msea.2015.02.054.

[11] W.-S. Lee, T.-H. Chen, Plastic deformation and fracture characteristics of Hadfield steel subjected to high-velocity impact loading, Proceedings of the Institution of Mechanical Engineers, Part C: Journal of Mechanical Engineering Science. 216 (2002) 971–982. doi:10.1243/095440602760400940.

[12] F.C. Liu, B. Lv, F.C. Zhang, S. Yang, Enhanced work hardening in Hadfield steel during explosive treatment, 65 (2011) 2333–2336. doi:10.1016/j.matlet.2011.05.041.

[13] D. Canadinc, C. Efstathiou, H. Sehitoglu, On the negative strain rate sensitivity of Hadfield steel, Scripta Materialia. 59 (2008) 1103–1106. doi:10.1016/j.scriptamat.2008.07.027.

[14] C. Efstathiou, H. Sehitoglu, Strain hardening and heterogeneous deformation during twinning in Hadfield steel, Acta Materialia. 58 (2010) 1479–1488. doi:10.1016/j.actamat.2009.10.054.

7. ORIENTATION DEPENDENCE OF THE MECHANICAL RESPONSE AND MICROSTRUCTURAL EVOLUTION OF NICOCR SINGLE CRYSTAL MEDIUM ENTROPY ALLOYS

The findings of the previous study presented the significant effect of the nanotwin formation upon ultra fast deformation. Twin inside twin formation has further improved hardenability of the material which resulted with an improved mechanical response. The aim of the study to be presented in the next chapter was to investigate the plastic deformation mechanism dependent on the orientation of the material. For this purpose single crystal samples were subjected to plastic deformation by eliminating the complexities which might stem due to grain interactions. In addition to that the orientations were selected in a way to preferentially activate the desired mechanisms. This provided to better understand the mechanical behavior dependence of the material on the microstructural evolution.

7.1 Introduction

Metallic materials have been broadly used throughout the centuries and the discovery of the new alloys with superior physical and mechanical properties further expands their use in new applications. In the recent decade the systems with multicomponent alloys have attracted the attention of the researchers due to their unique combination of high strength, ductility, fracture toughness, and wear and corrosion resistance [1–9]. These alloys are composed of multiple elements in near equiatomoic compositions which differ significantly from the conventional alloys that are composed of single principal element and minor additional alloying elements such as stainless steel or nickel based alloys [2,7,10]. Instead of exhibiting a complex structure high configurational entropy of the multi principal element alloys (MPEAs) can overcome the mixing enthalpy of intermetallic phases and lead to a structure with a simple phase [10,11]. MPEAs with 5 or more elements are grouped as high entropy alloys (HEAs), whereas the alloys with 3 or 4 elements are regarded as medium entropy alloys (MEAs). HEAs and MEAs alloys have been

subjected to numerous mechanical testings and have shown unprecedented mechanical strength without sacrificing the ductility [4,5,9,10,12]. One of the most important reasons for this improved mechanical response can be given as the highly distorted lattice structure due to cumulative effect of the different atoms within the first coordination shell [13]. It should be noted that the strain field created by this local distortion plays important role for the strengthening of these alloys thorough impediment of the gliding dislocations [13,14]. Among the all MPEAs NiCoCr MEA alloy has presented the best combination of mechanical strength and fracture toughness without sacrificing the ductility [4,15,16]. Stacking fault energy (SFE) of this alloy was measured as 22 ± 4 mJ m^{-2} whereas the one of FeMnCrCoNi was determined as 22 ± 4 mJ m^{-2} [17]. In addition to that the slightly lower shear modulus of NiCoCr in concomitant with the lower SFE made it easier to reach the critical stress for the twin formation which leaded to enhanced ductility through postponing the necking instability [4,15]. The activity of the plastic deformation mechanisms of the polycrystalline NiCoCr upon tensile loading at different test temperatures have been addressed recently [4,15,18]. The results showed improvement in the mechanical strength, damage tolerance and ductility at the lower temperatures specifically due to the activation of nanotwinnings [15,19,20]. Due to these superior properties NiCoCr constitutes a promising alloy among all the MPEAs and its microstructural and mechanical properties need further investigation. Specifically to the best of authors' knowledge a study presenting the thorough analysis to understand the dependence of the uniaxial stress-strain response of NiCoCr MEAs on crystal orientation has not been forwarded yet. The current study was undertaken to address this issue by utilizing single crystal NiCoCr alloys in order to eliminate the complications that may stem from the grain boundary effect and the interactions between the neighboring grains [21]. In addition the use of single crystals also provides a better understanding of the effect of the governing plastic deformation mechanisms through preferentially activating the desired mechanisms and controlling the number of active slip systems. For this purpose three different crystallographic orientations were selected: [110], [111] and [123]. The activation of deformation

twinning and slip show differences in each orientation depending on their Schmid factors in each crystal. For example in FCC crystals the formation of twinning is most favorable in [111] orientation because the Schmid factor for twinning (m_{tw} = 0.314) is larger than for slip (m_{sl} = 0.27) in this orientation [22]. On the other hand in the same orientation activation of multiple slip systems is expected, whereas only one system is expected in [110] and [123] orientations [23].

In the current study single crystal NiCoCr MEAs have been subjected to uniaxial tension test and their stress-strain response was evaluated. Analyses on the single crystals of this alloy with three different crystallographic orientations enabled the authors to observe orientation dependence of the activation of slip and twinning mechanisms which has not been reported yet [24]. In order to understand the microstructural evolution in different levels of deformation the tensile test was interrupted at different strain levels. In this way the activation of plastic deformation mechanisms and their interactions were captured in the initial stages via transmission electron microscopy (TEM) and optical microscopy (OM) techniques. Critical stress value to initiate twinning was evaluated for the sample in [111] orientation which is the most favorable orientation for twinning [22]. These findings were used to elucidate the reasons for the superior mechanical properties of this alloy compared with its quinary and quaternary counterparts.

7.2. Experimental Details

The equiatomoic single crystal NiCoCr medium entropy alloy specimens used in this study were grown by the Bridgeman method. Specifically workpiece blanks were melted in a resistance furnace and the NiCoCr single crystal bulk was obtained in an argon atmosphere. The melting process was repeated three times for the homogenous distribution of the atoms throughout the bulk. The tensile test samples with different crystallographic orientations ([110], [111] and [123]) were cut by electric discharge machining (EDM) from the bulk. The samples were sealed in a quartz tube with argon atmosphere and homogenized at 1473°K for 24 hours

[8]. The surfaces of the tensile test specimens were ground with 600, 800, 1000 and 1200 grit SiC sandpapers and polished with 6, 3 and 1μm size diamond abrasives respectively. Prior the mechanical testings material characterization techniques were utilized. X-ray diffraction analysis (XRD) was used for the phase identification and texture analysis. Elemental composition of the samples was quantified with wavelength dispersive X-ray spectroscopy (WDS) by collecting the data from 10 different points which were at least 300μm apart from each other. Electron backscatter diffraction (EBSD) technique was utilized for the understanding of the microstructural evolution. The samples analyzed with EBSD and WDS were also polished with colloidal silica suspension as the final polishing step. Three samples in each orientation were subjected to tensile test up to fracture with a MTS Tensile Test Setup with the strain rate of 5×10^{-4} s^{-1} at room temperature. Additional tests were run by interrupting the tensile test at different strain levels in order to better understand the microstructural evolution and the effect of governing deformation mechanisms on the mechanical behavior in the early stages of the deformation. Surface relief on the sample surfaces were investigated with secondary electron microscope (SEM) and optical microscopy (OM) and the activation of plastic deformation mechanisms was analyzed via transmission electron microscope (TEM). TEM samples were prepared by grinding the deformed tensile samples down to 60μm thickness with 600 grit SiC sandpaper and punching them into discs with 3mm of diameter. Then these discs were twin-jet electropolished in the working temperature of -20°C with an electrolyte consisting of 75% of methanol and 25% of nitric acid at 20V. TEM analyses were carried out with the FEI Tecnai 20ST model operating at 200kV.

7.3. Results and Discussion

Prior the mechanical testings elemental composition analysis of the NiCoCr single crystal samples via WDS showed that the samples contained almost equal atomic concentrations of Ni, Co and Cr elements which are reported respectively as 33.42 ± 0.14, 33.60 ± 0.68 and 32.98 ±

0.72. Phase and crystal structure analyses of the samples with XRD and EBSD showed that the alloy had simple FCC phase and single crystal structure. Lattice parameter was determined with XRD as 0.3575nm which is in good agreement with the numbers reported in the literature earlier [15].

When the tensile response (Figure 7.1) of these three orientations were compared sample in [111] orientation exhibited the greatest yield and ultimate tensile strength which is greater than the Cantor alloy in the same orientation [3]. On the other hand the greatest elongation to fracture was observed in [123] orientation similar to the results obtained with the Hadfield steel in the literature [21,24]. In order to understand the how the deformation was accommodated in each sample microstructures of the fractured samples were analyzed with transmission electron microscopy (TEM) and twins in nanometers of thickness were observed on each orientation (Figure 7.2, 7.3 and 7.4). In addition to that twin-twin interactions were observed on the samples which increase the local stress concentration [25].

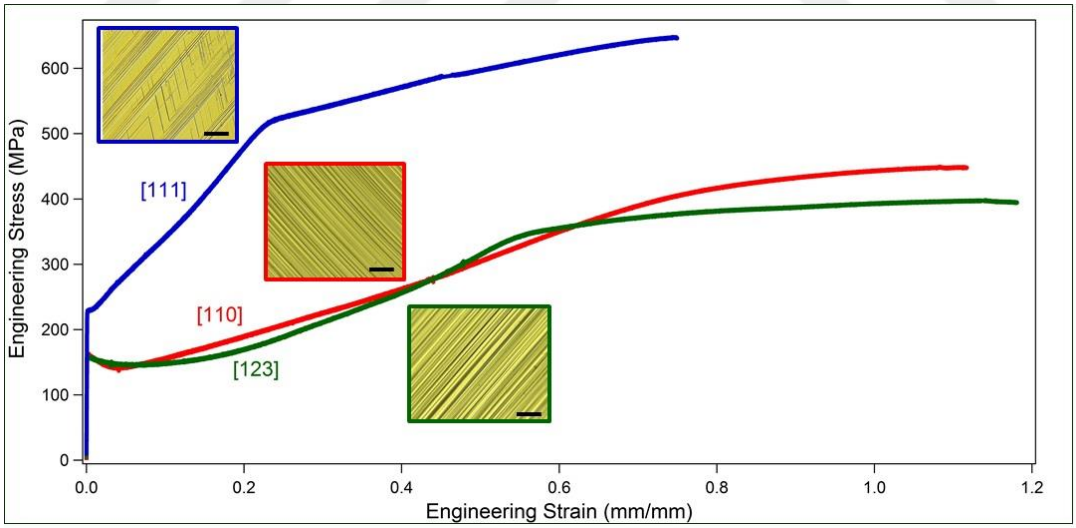

Figure 7.1. Stress-strain curve of the NiCoCr samples in [110], [111] and [123] orientations deformed up to fracture under tensile loading. The optical microscopy (OM) images within the graph were obtained from the samples deformed up to 4% ([110]) and 10% ([111] and [123]) of strain. The crystallographic orientation of the images from top to bottom is: [111], [110] and [123]. The scale bar in OM images is 50μm. (To better understand the graph and its corresponding OM image the reader is referred to the web version of this paper.)

The engineering stress-strain curves of each sample (Figure 7.1) present the orientation dependency of the mechanical response of these samples where each orientation presents a different strain hardening behavior with different deformation stages. Specifically while the samples in [110] and [123] orientations present upper and lower yield strengths and the Lüder's type propagation of localized deformation the sample in [111] orientation exhibited a linear hardening regime. This difference stems from the activation of different number of slip systems, such as in [110] and [123] 1 slip system prevails on the other hand in [111] more than 1 system is activated. Owing to this difference [111] crystal exhibits a small region of stage I hardening on the contrary to the [110] and [123]. In order to elucidate the activation of plastic deformation mechanisms in the early stages of deformation tension tests were interrupted at lower strain levels. Figure 7.2.a shows the dislocation pile ups in the twin boundary of the [111] sample deformed up to 10% of deformation strain [20,26]. In addition to that stacking faults and nanotwins are also observed. The mutual interaction of these mechanisms has promoted the strengthening of the material and provided the stage II deformation with a greater work hardening rate (WHR) [3,17,20,24,26]. Specifically the blockage of dislocation glide by a twin These results are in good agreement with the earlier studies carried out on single crystal Hadfield steel and austenitic stainless steel in the [111] orientation [27,26].

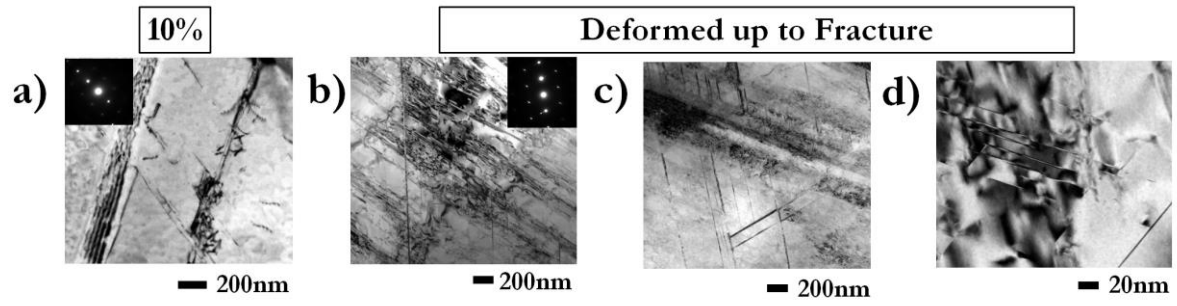

Figure 7.2. TEM micrographs and diffraction patterns of the samples in [111] orientation deformed up to **(a)** 10% and **((b), (c) and (d))** fracture.

Easy glide regime of [110] and [123] samples have leaded to a lower work hardening rate compared with the [111] sample. In order to understand the activation of deformation mechanisms in the early stage of plasticity the surface relief of the samples deformed up to 4% ([110]) and 10% ([111] and [123]) of strain were analyzed with optical microscopy. These images (within the Figure 7.1) show the localized deformation in the gauge sections of the [110] and [123] orientations however the deformation bands showed a spread behavior on all over the gauge section of the [111] sample which was stemming from the activation of multiple slip systems in this crystallographic orientation [22].

The recent studies on the deformation mechanism of polycrystalline NiCoCr have shown that the early stage of plasticity takes place by the splitting of the 1/2<110> type perfect dislocations into 1/6<112> type Shockley partials dislocations [15]. In the later stages of deformation twinning gets activated through the interaction of these stacking faults and dislocations which provides the stress required for the twin nucleation. These formed twins act as obstacles for the dislocations and increase the work hardening of the material which delays the onset of necking and consecutively increases the ductility [4,15]. The propensity to form twinnings in these alloys were supported by a recent study where the twinnability of this alloy showed higher value than all pure fcc metals and it was comparable with the Fe-Cr-Ni TWIP steels [20]. Specifically the activation of multiple twin systems has created a 3D twin structure which has significantly enhanced the ductility of the material by offering multiple pathways for the dislocation motion along the boundaries [20]. In order to better understand the underlying mechanisms initiating the twin nucleation in the earlier deformation stages of the single crystal NiCoCr alloy additional tests were carried out in the current study. Specifically the TEM micrographs of the tensile test specimen interrupted at the strain of 10% in [111] orientation shows the interaction of dislocations and stacking faults clearly (Figure 7.2a). It should be noted that the observed stacking faults in the early stage of plasticity of low stacking fault energy alloys contribute to the formation of twinnings in the later stages of the deformation by serving as

precursor [21]. Specifically the Lomer-Cottrell barriers which have prevented the dislocation motion provided the stress concentration for the twin nucleation in the later stages of the deformation [27,28]. The greater strength of the samples deformed in the [111] orientation was related with the activation of these mechanism in the earlier stage of plasticity. In addition to that TEM micrographs of [123] sample show the interaction of three different systems of nanotwinnings which validates the high ductility of this sample by postponing the plastic instability (Figure 7.3b and 7.4a). Nanotwinning formation and their interactions were observed in the austenitic steels earlier and they were concluded to be the major cause for the brittle fracture in these materials [29]. However in the current study although a high volume fraction of the twin-twin interactions was observed the fracture showed ductile behavior for all of the orientations. This can be stemming from the gliding of dislocations along the twin boundaries and interaction sites which would eventually lead to the relief of the high stress concentration of these sites [20,30].

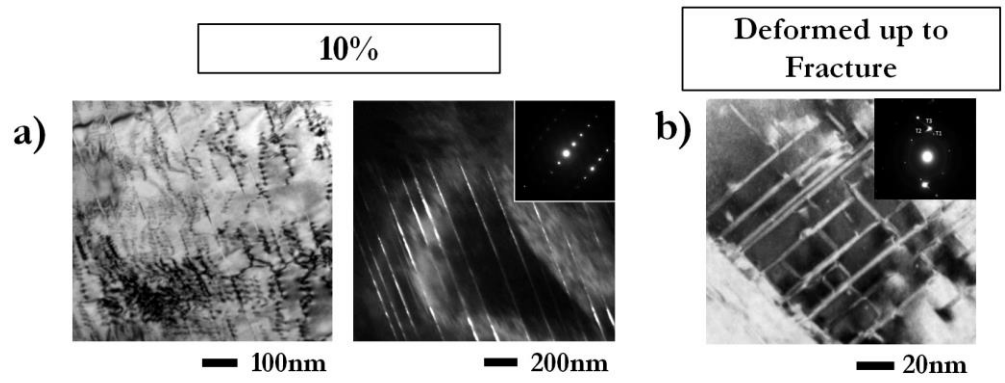

Figure 7.3. TEM micrographs and diffraction patterns of the samples in [123] orientation deformed up to **(a)** 10% and **(b)** fracture**.**

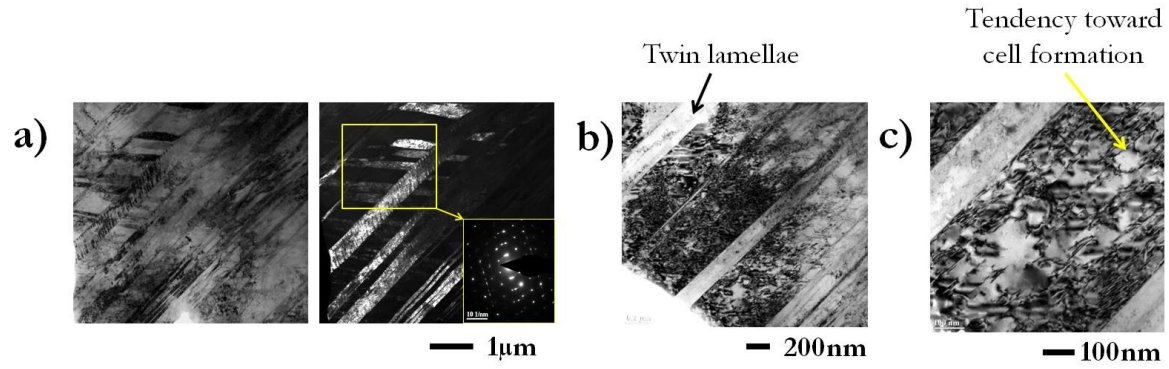

Figure 7.4. TEM bright field images of NiCoCr samples in [123] orientation deformed up to fracture.

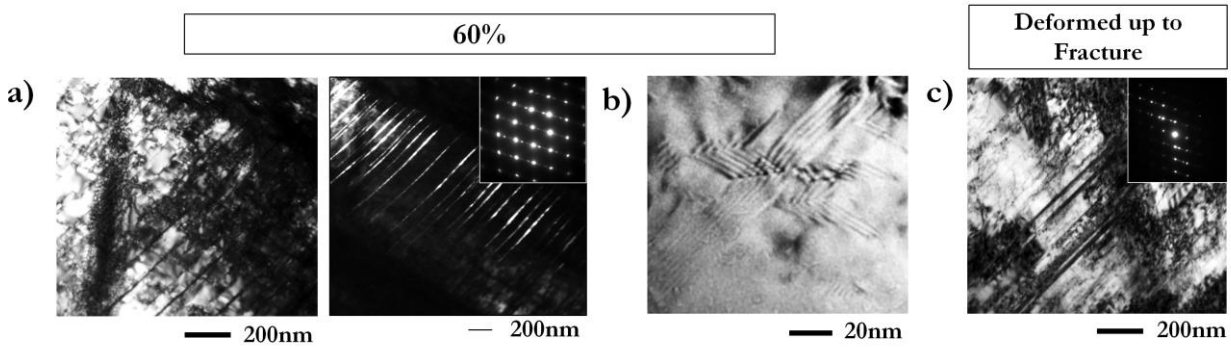

Figure 7.5. TEM micrographs and diffraction patterns of the samples in [110] orientation deformed up to **((a) and (b))** 60% and **(c)** fracture**.**

Overall these results show that unique combination of the elements in NiCoCr MEA provides this alloy to exhibit unprecedented mechanical and microstructural properties upon tensile loading. It presents a high work hardening capacity due to dissociation of perfect dislocation into Shockley partials in the early stages of plasticity and, activation and interaction of nanotwinnings in the later stages. The high stress concentration of the interaction sites of the nanotwinnings was relieved by allowing the dislocation glide along these boundaries which also leaded to a ductile fracture of this material. Considering the superior mechanical properties of the MPEAs in lower temperatures the further investigation of the NiCoCr at lower temperatures would result with much better strength and ductility combination.

7.4. References

[1] B.J. Yeh, S. Chen, S. Lin, J. Gan, T. Chin, T. Shun, C. Tsau, Nanostructured High-Entropy Alloys with Multiple Principal Elements : Novel Alloy Design Concepts and Outcomes, (2004) 299–303. doi:10.1002/adem.200300567.

[2] B. Cantor, I.T.H. Chang, P. Knight, A.J.B. Vincent, Microstructural development in equiatomic multicomponent alloys, Materials Science Engineering A. 375–377 (2004) 213–218. doi:10.1016/j.msea.2003.10.257.

[3] I. Kireeva, Y. Chumlyakov, Z. Pobedennaya, Mechanisms of Plastic Deformation in [111] Oriented Single Crystals of FeNiMnCrCo High Entropy Alloy, 20090 (2016) 1–5. doi:10.1063/1.4966383.

[4] B. Gludovatz, A. Hohenwarter, K.V.S. Thurston, H. Bei, Z. Wu, E.P. George, R.O. Ritchie, entropy alloy CrCoNi at cryogenic temperatures, Nature Communications. 7 (2016) 1–8. doi:10.1038/ncomms10602.

[5] B. Gludovatz, A. Hohenwarter, D. Catoor, E.H. Chang, E.P. George, R.O. Ritchie, A fracture-resistant high-entropy alloy for cryogenic applications, 345 (2014).

[6] M. Tsai, J. Yeh, M. Tsai, J. Yeh, High-Entropy Alloys : A Critical Review High-Entropy Alloys : A Critical Review, 3831 (2017). doi:10.1080/21663831.2014.912690.

[7] D.B. Miracle, D.B. Miracle, Critical Assessment 14 : High entropy alloys and their development as structural materials Critical Assessment 14 : High entropy alloys and their development as structural materials, 836 (2016). doi:10.1179/1743284714Y.0000000749.

[8] Z. Wu, H. Bei, F. Otto, G.M. Pharr, E.P. George, Intermetallics Recovery , recrystallization , grain growth and phase stability of a family of FCC-structured multi-component equiatomic solid solution alloys, 46 (2014) 131–140.

doi:10.1016/j.intermet.2013.10.024.

[9] F. Otto, A. Dlouhy, C. Somsen, H. Bei, G. Eggeler, E.P. George, The influences of temperature and microstructure on the tensile properties of a CoCrFeMnNi high-entropy alloy, 61 (2013) 5743–5755. doi:10.1016/j.actamat.2013.06.018.

[10] A. Gali, E.P. George, Intermetallics Tensile properties of high- and medium-entropy alloys, Intermetallics. 39 (2013) 74–78. doi:10.1016/j.intermet.2013.03.018.

[11] D.B. Miracle, O.N. Senkov, Acta Materialia A critical review of high entropy alloys and related concepts, Acta Materialia. 122 (2017) 448–511. doi:10.1016/j.actamat.2016.08.081.

[12] F. Otto, Y. Yang, H. Bei, E.P. George, Relative effects of enthalpy and entropy on the phase stability of equiatomic high-entropy alloys, Acta Materialia. 61 (2013) 2628–2638. doi:10.1016/j.actamat.2013.01.042.

[13] L.R. Owen, E.J. Pickering, H.Y. Playford, H.J. Stone, M.G. Tucker, N.G. Jones, An assessment of the lattice strain in the CrMnFeCoNi high-entropy alloy, Acta Materialia. 122 (2017) 11–18. doi:10.1016/j.actamat.2016.09.032.

[14] Z. Zhang, M.M. Mao, J. Wang, B. Gludovatz, Z. Zhang, S.X. Mao, E.P. George, Q. Yu, R.O. Ritchie, Nanoscale origins of the damage tolerance of the high-entropy alloy CrMnFeCoNi., Nature Communications. 6 (2015) 10143. doi:10.1038/ncomms10143.

[15] G. Laplanche, A. Kostka, C. Reinhart, J. Hunfeld, G. Eggeler, E.P. George, Acta Materialia Reasons for the superior mechanical properties of medium-entropy CrCoNi compared to high-entropy CrMnFeCoNi, Acta Materialia. 128 (2017) 292–303. doi:10.1016/j.actamat.2017.02.036.

[16] K. Jin, Y.F. Gao, H. Bei, Intrinsic properties and strengthening mechanism of monocrystalline Ni-containing ternary concentrated solid solutions, Materials Science and Engineering: A. 695 (2017) 74–79. doi:10.1016/j.msea.2017.04.003.

[17] G. Laplanche, A. Kostka, C. Reinhart, J. Hunfeld, G. Eggeler, E.P. George, Acta Materialia Reasons for the superior mechanical properties of medium-entropy CrCoNi compared to high-entropy CrMnFeCoNi, Acta Materialia. 128 (2017) 292–303. doi:10.1016/j.actamat.2017.02.036.

[18] Z. Wu, H. Bei, G.M. Pharr, E.P. George, ScienceDirect Temperature dependence of the mechanical properties of equiatomic solid solution alloys with face-centered cubic crystal structures, 81 (2014) 428–441. doi:10.1016/j.actamat.2014.08.026.

[19] F. Otto, A. Dlouhý, C. Somsen, H. Bei, G. Eggeler, E.P. George, The influences of temperature and microstructure on the tensile properties of a CoCrFeMnNi high-entropy alloy, Acta Materialia. 61 (2013) 5743–5755. doi:10.1016/j.actamat.2013.06.018.

[20] Z. Zhang, H. Sheng, Z. Wang, B. Gludovatz, Z. Zhang, E.P. George, Q. Yu, S.X. Mao, R.O. Ritchie, Dislocation mechanisms and 3D twin architectures generate exceptional strength-ductility-toughness combination in CrCoNi medium-entropy alloy, Nature Communications. 8 (2017) 14390. doi:10.1038/ncomms14390.

[21] D. Canadinc, H. Sehitoglu, H.J. Maier, D. Niklasch, Y.I. Chumlyakov, Orientation evolution in Hadfield steel single crystals under combined slip and twinning, International Journal of Solids and Structures. 44 (2007) 34–50. doi:10.1016/j.ijsolstr.2006.04.011.

[22] I. V Kireeva, Y.I. Chumlyakov, Effect of Nitrogen and Stacking-Fault Energy on Twinning in [111] Single Crystals of Austenitic Stainless Steels, 108 (2009) 313–324. doi:10.1134/S0031918X09090117.

[23] P.O.K. T.K. Lepistö, Comparison of the Cyclic Stress-Strain Behaviour of Single-and <111> Multiple-slip-oriented Copper Single Crystals, Materials Science and Engineering. 83 (1986) 1–15.

[24] I. Karaman, H. Sehitoglu, K. Gall, Y.I. Chumlyakov, H.J. Maier, Deformation of single

crystal hadfield steel by twinning and slip, Acta Materialia. 48 (2000) 1345–1359. doi:10.1016/S1359-6454(99)00383-3.

[25] W. Wu, M. Song, S. Ni, J. Wang, Y. Liu, B. Liu, X. Liao, Dual mechanisms of grain refinement in a FeCoCrNi high- entropy alloy processed by high- pressure torsion, Scientific Reports. (2017) 1–13. doi:10.1038/srep46720.

[26] I. Karaman, The Competing Effects Of Slip And Twinning On The Deformation Of Hadfield Manganese Steel Single And Polycrystals, Acta Mater. 49 (2001) 3919-3933.

[27] I. Karaman, H. Sehitoglu, K. Gall, Y. Chumlyakov, H. Maier, Deformation of single crystal Hadfield steel by twinning and slip, Acta Metallurgica. 48 (2000) 1345–1359. doi:10.1016/S1359-6454(99)00383-3.

[28] W.S. Choi, S. Sandlöbes, N. V. Malyar, C. Kirchlechner, S. Korte-Kerzel, G. Dehm, B.C. De Cooman, D. Raabe, Dislocation interaction and twinning-induced plasticity in face-centered cubic Fe-Mn-C micro-pillars, Acta Materialia. (2017) doi:10.1016/j.actamat.2017.04.043.

[29] M.O.S. P. Müllner, C. Solenthaler, P. J. Uggowitzer, Brittle Fracture in Austenitic Steel, Acta Metallurgica et Materialia. 42 (1994) 2211–2217.

[30] L. Rémy, The interaction between slip and twinning systems and the influence of twinning on the mechanical behavior of fcc metals and alloys, Metallurgical Transactions A. 12 (1981) 387–408. doi:10.1007/BF02648536

8. CONCLUSION & FURTHER ELOBORATIONS

Metallic materials have been utilized in various applications throughout the centuries. Technological improvements and development of new materials with superior properties has further expanded their use in aerospace, automotive, biomedical and civil engineering. In this thesis the relationship between the microstructure and the mechanical properties of novel metallic material has been investigated. Mechanical tests were carried out on the materials which are utilized as structural or biomaterial. The tests were expanded to construct the relation between the biocompatibility and, the microstructural and mechanical properties of the material.

For this purpose initial experiments were carried out on the stainless steel implant materials which have been subjected to tensile test up to different levels of strain. The activated plastic deformation mechanisms were observed via different microscopy techniques and their relation with the cell adhesion response was analyzed. The findings of this study showed the enhanced brain tumor cell response on the sample with the greatest amount of plastic deformation which catalyzed the formation of focal contacts on the implant surface due to the greater energy provided by the activated mechanisms. In addition to that this study showed that the surface topography was also modulated with the micro deformation mechanisms, such that the surface roughness increased with the enhanced plastic strain. In order to understand whether a different type of cell would respond in a similar way or not the fibroblasts cells were also seeded on these deformed steel implants. On the contrary to the enhanced response by the tumor cells the adhesion behavior of fibroblasts did not direct relation with the plastic strain. These findings point out the significant effect of the microstructure of the material on the biocompatibility of the material.

In order to thoroughly comprehend the parameters affecting the biocompatibility of the metallic materials further experiments were carried out. The biocompatibility of the Nickel Titanium (NiTi) orthodontic archwires were evaluated with immersion tests through the

incorporation of the realistic mechanical conditions into *ex situ* experiments. This study showed the significant effect of this critical approach, such that the toxic Ni ion release increased significantly due to stress corrosion cracking (SCC). The stress accumulated in the bracket archwire contact sites in concomitant with the corrosive environment of the artificial saliva (AS) created cracks on the archwires. Overall the findings of this study demonstrated the need for incorporating both realistic chemical and mechanical conditions into the *ex situ* biocompatibility experiments in order to manufacture orthodontic archwires with enhanced biocompatibility.

This study was followed by the investigation of the dissolution-reformation cycle of the protective oxide layer which plays critical role for preventing the Ni ion release. The characterization of the NiTi archwires immersed in AS with different pH values and immersion periods showed enhanced Ni ion release in the most corrosive solution and the oxide layer dissolution-reformation cycle within the 14 days of immersion period. The dissolution of the oxide layer enhanced ion release whereas during reformation the net contribution of Ni ion release decreased significantly. Furthermore the oxide layer formation was catalyzed on the regions with larger surface energy such as grooves and thus surface roughness was in direct relation with this cycle. These findings showed that in order to achieve the highest degree of biocompatibility and an efficient treatment the thorough analysis of the oxide layer dissolution-reformation cycle by the incorporating of the surface roughness and ion release behavior constitute utmost importance.

Having understood the critical parameters that strongly affect the biocompatibility of the metallic materials the relation of the microstructural and mechanical properties of the metals have been further investigated. In order to observe the activation of slip and twinning mechanisms, and capture their interaction metals with complex microstructures were subjected to mechanical testings. Initially polycrystal Hadfield steel with low stacking fault energy was subjected to ultra fast deformation which has promoted the activation of nanotwinnings, dislocations and

dislocation-twin interaction. In addition to that the formation of nanotwins within the primary twins was observed in the regions affected the most from the explosion. This study shows that activation of twin-twin interaction promotes the strengthening of the material and thus the material can endure the great amount of plastic deformation.

With the aim to better understand the activation of plastic deformation mechanisms single crystal NiCoCr samples were subjected to mechanical tests where the complications that may stem from the grain boundary effect and the interactions between the neighboring grains were eliminated. The studies carried out on polycrystalline NiCoCr alloy have presented the superior properties of this alloy compared with its quinary or quaternary counterparts. In the current thesis three crystallographic orientations were utilized ([110], [111] and [123]) and the desired plastic deformation mechanisms were preferentially activated. The results showed the strong orientation dependence of the stress-strain response of the crystals. The greater ductility of the sample with [123] was related with the enhanced twin-twin interaction which delayed the onset of necking. On the other hand analyses carried out on the [111] sample showed the interaction of nanotwinnings and dislocations where the dislocation motion was impeded by the twins. This has promoted the strain hardening and the increased the strength of this sample. Overall this study shows the significant influence of orientation on the mechanical response and microstructural evolutions. In order to evaluate the mechanical behavior of polycrystalline NiCoCr the findings of the single crystal need to be incorporated.

In this dissertation the author has analyzed the novel metallic materials from interdisciplinary applications. The findings show that the mechanical property of a metal is strongly influenced by its microstructure. Through these testings superior metallic materials to be utilized for aerospace applications at cryogenic temperatures can be developed and space exploration can be promoted further. In addition to that for the metals to be utilized in biomedical applications these two properties need to be incorporated into the biocompatibility

investigations in order to obtain metallic implants which can promote the highest cell attachment, shorten the recovery period and eliminate the post-surgical complications.

The findings of this dissertation evidenced enhanced cell viability and attachment behavior through the manipulation of the implant microstructure. However these results were confined with the SEM and Confocal Microscopy observations which were limited in the larger scale. As a future work author aims to investigate the cellular attachment in the small scale facilitating the TEM analysis. In this way the interaction of the cells with the micro deformation mechanisms would be observed in more detail and the most critical regions (i.e. twin-slip interaction sites, grain boundary, twin boundary…) influencing the cell response can be pointed out.

VITA

Benay Uzer graduated from the Department of Mechanical Engineering at Koç University in June 2013 with the highest rank in her department. She started doing PhD in the same department at Koç University in September 2013 under the supervision of Dr. Demircan Canadinç. She has been a visiting scholar at Leibniz University Hannover and Texas A&M University.

LIST of PUBLICATIONS

1) **Uzer B,** Toker SM, Cingoz A, Bagci-Onder T, Gerstein G, Maier H, Canadinc D, 2016. An Exploration of Plastic Deformation Dependence of Cell Viability and Adhesion in Metallic Implant Materials. Journal of Mechanical Behavior of Biomedical Materials 60, 177–186. doi:10.1016/j.jmbbm.2016.01.001

2) **Uzer B,** Gumus B, Toker SM, Sahbazoglu D, Saher D, Yildirim C, Polat-Altintas S, Candinc D, 2016. A Critical Approach to the Biocompatibility Testing of NiTi Orthodontic Archwires. International Journal of Metallurgy and Metal Physics. 1, 1–7.

3) **Uzer B,** Canadinc D, 2016. The Effect Of Plastic Deformation On The Cell Viability And Adhesion in Metallic Implant Materials. Ceramic Transactions (Accepted)

4) **Uzer B,** Birer O, Canadinc D, Investigation of the Dissolution – Reformation Cycle of the Passive Oxide Layer on NiTi Orthodontic Archwires. 2017. Journal of Shape Memory and Superelasticity. doi: 10.1007/s40830-017-0114-3

5) Canadinc D, **Uzer B,** Elmadagli M, Guner F, Nanotwin Formation in High-Manganese Austenitic Steels under Explosive Shock Loading, 2017. Materials Science and Engineering A (Submitted)

6) **Uzer B,** Liu J, Ozcan H, Jozaghi T, Canadinc D, Karaman I, Chumlyakov Yu I. Orientation Dependence of the Mechanical Response and Microstructural Evolution of Single Crystal Medium Entropy Alloys, 2017. To be submitted to Scripta Materialia (In Preparation)